Title

Communicating Change Across Scales: Turbulence causes small things to make big impacts

ISBN

9798180196590

Author

Bellerjeau, Charlotte

Publication Date

2026-07-24

Peer reviewed|Thesis/dissertation

UNIVERSITY OF CALIFORNIA SAN DIEGO

Communicating Change Across Scales: Turbulence causes small things to make big impacts

A Dissertation submitted in partial satisfaction of the requirements
for the degree Doctor of Philosophy

in

Oceanography

by

Charlotte Bellerjeau

Committee in charge:

Matthew Alford, Chair
Arnaud Le Boyer
Jennifer MacKinnon
Sarah Purkey
Sutanu Sarkar
BT Werner

2026

The Dissertation of Charlotte Bellerjeau is approved, and it is acceptable in quality and form for publication on microfilm and electronically.

University of California San Diego

2026

TABLE OF CONTENTS

LIST OF FIGURES

ACKNOWLEDGEMENTS

I would like to thank my advisor Matthew Alford for his unwavering support and trust over the past five years. His guidance allowed me the flexibility to follow my curiosity wherever it led, while keeping me on track to produce rigorous and thoughtful work. I also extend gratitude to my committee members Arnaud Le Boyer, Jennifer MacKinnon, Sarah Purkey, Sutanu Sarkar, and bt werner for their support and encouragement on my academic journey. I would like to especially acknowledge Arnaud for always sharing what excited him in science, from teaching me to plot my first spectrum to helping me finish testing my sensors this month. A special thank you to bt for helping me see myself in science, creating spaces that felt welcoming, and setting an excellent example of teaching and mentorship.

I've had the privilege to become part of an incredible scientific community outside of SIO as well. Thank you to my co-authors Alberto Naveira-Garabato and Giovanni Dematteis, and collaborator Kurt Polzin, all of whom helped me frame and develop Chapter 1. It was a joy working with all of you. I will never forget when Alberto responded to one of my questions by saying, "We are standing on the edge of the unknown together". What a beautiful way to say I don't know, but let's find out together! Thank you all for showing me how to be a part of a scientific community.

Thank you to the whole MOD Lab without whom none of this research would be possible. It has been a pleasure working with such a talented and vibrant group of engineers and scientists during my time in graduate school. Thank you for teaching me how important teamwork is in research.

My fellow students have been a constant source of inspiration, joy, and strength throughout this experience. Thank you to my cohort and friends for being by my side through all the ups and downs. It was an honor to be among friends for many hours doing homework, in the lab and office, on fieldwork, and on the picket line. Amazing, creative, talented, brave students are what makes SIO excellent.

Finally and always, thank you to my family. Mason, you are my best friend and the most amazing partner. I am so grateful for your constant love and support throughout the past five years. Thank you to the whole Kingsbury family for always making me feel cherished and supported, especially Tadia and Mark for giving me a home away from home. Karl, thank you for reminding me why I love this planet so much and your continued effort and support as my brother. To my chosen sister, thank you Erica for your constant stoke, love, and for being a part of my life. You all have been my anchor and my north star, and I appreciate you so much.

Chapter 1, in full, is a reprint of the material as it appears in Pathways to Turbulent Dissipation in a Submarine Canyon. Bellerjeau, Charlotte; Matthew H. Alford; Arnaud Le Boyer; Giovanni Dematteis; Alberto Naveira Garabato; Gunnar Voet; Nicole Couto; and Bethan L. Wynne-Cattanach, Geophysical Research Letters, 2025. The dissertation author was the primary investigator and author of this paper.

Chapter 2, in part is currently being prepared for submission for publication of the material. Bellerjeau, Charlotte; Alford, Matthew H.; Voet, Gunnar; Couto, Nicole; Le Boyer, Arnaud. “Near-Inertial Wave Drag one the Gulf Stream”. The dissertation author was the primary investigator and author of this material.

Chapter 3, in part is currently being prepared for submission for publication of the material. Bellerjeau, Charlotte; Le Boyer, Arnaud; Alford, Matthew H.; Lastuka, Sean; McConnell Becca. “Polymer Shear Probes for Durable Ocean Turbulence Sensing”. The dissertation author was the primary investigator and author of this material.

Chapter 4, in part is currently being prepared for submission for publication of the material. Bellerjeau, Charlotte. “Basic or Applied: Complicity and Tuning the Proximity of Research to its Impacts”. The dissertation author was the primary investigator and author of this material.

VITA

2020 Bachelor of Science in Aerospace Engineering Sciences, University of Colorado Boulder

2023 Master of Science in Oceanography, University of California San Diego

2026 Doctor of Philosophy in Oceanography, University of California San Diego

PUBLICATIONS

Alford, M. H., Le Boyer, A., Ren, A. S., Voet, G., **Bellerjeau, C**., Whalen, C. B., Hall, B., & Couto, N. (2025). Observations of Turbulence Generated by a Near-Inertial Wave Propagating Downward in an Anticyclonic Eddy. *Geophysical Research Letters*, *52*(6), e2024GL114070. https://doi.org/10.1029/2024GL114070

Masunaga, E., Alford, M. H., & **Bellerjeau, C.** (2025). *Mechanisms of Internal Tide–Induced Turbulent Mixing Observed from Mooring Data in a Shallow Steep Submarine Canyon*. https://doi.org/10.1175/JPO-D-24-0132.1

Kauzya, J.-B., Hayes, B., Hayes, A. C., Thompson, J. F., **Bellerjeau, C**., Evans, K., Osio-Norgaard, J., Gavai, G., Dikshit, K., Bruns, C., MacCurdy, R., Street, R. A., & Whiting, G. L. (2024). Direct ink writing of viscous inks in variable gravity regimes using parabolic flights. *Acta Astronautica*, *219*, 569–579. https://doi.org/10.1016/j.actaastro.2024.03.037

Atreya, M., Marinick, G., Baumbauer, C., Dikshit, K. V., Liu, S., **Bellerjeau, C**., Nielson, J., Khorchidian, S., Palmgren, A., Sui, Y., Bardgett, R., Baumbauer, D., Bruns, C. J., Neff, J. C., Arias, A. C., & Whiting, G. L. (2022). Wax Blends as Tunable Encapsulants for Soil-Degradable Electronics. *ACS Applied Electronic Materials*, *4*(10), 4912–4920. https://doi.org/10.1021/acsaelm.2c00833

Barthold, J. E., McCreery, K. P., Martinez, J., **Bellerjeau, C**., Ding, Y., Bryant, S. J., Whiting, G. L., & Neu, C. P. (2022). Particulate ECM biomaterial ink is 3D printed and naturally crosslinked to form structurally-layered and lubricated cartilage tissue mimics. *Biofabrication*, *14*(2), 025021. https://doi.org/10.1088/1758-5090/ac584c

Thompson, J. F., **Bellerjeau, C**., Marinick, G., Osio-Norgaard, J., Evans, A., Carry, P., Street, R. A., Petit, C., & Whiting, G. L. (2019). Intrinsic Thermal Desorption in a 3D Printed Multifunctional Composite CO2 Sorbent with Embedded Heating Capability. *ACS Applied Materials & Interfaces*, *11*(46), 43337–43343. https://doi.org/10.1021/acsami.9b14111

ABSTRACT OF THE DISSERTATION

Communicating Change Across Scales: Turbulence causes small things to make big impacts

by

Charlotte Bellerjeau

Doctor of Philosophy in Oceanography

University of California San Diego, 2026

Matthew Alford, Chair

Winds and tides force oceanic motion at many different scales from basin scale overturning to centimeter scale turbulence. The physical mechanisms that transfer kinetic energy and momentum between these scales allow the global climate to be influenced by processes that are too small to be resolved by models. Understanding the physics behind these transfers of energy and momentum holds the key to parameterizing their impact in models. Observations allow us to understand the physics on a deeper level, and continue to see the ocean from new

perspectives as technology evolves. This thesis uses observations to illuminate the physical mechanisms by which internal wave breaking transfers energy and momentum between scales, and the human mechanisms that allow those observations to exist.

In Chapter 1 we use observations to show the pathway of kinetic energy cascade from internal tides to turbulence in frequency-space. Chapter 2 presents observations and ray tracing of near-inertial wave propagation and breaking, contributing a momentum drag to the Gulf Stream. In Chapter 3 we present a novel design for the turbulence sensing shear probe which will make ocean turbulence sensing more durable and a better candidate for large-scale observational programs. Finally, in Chapter 4 we analyze 10 years of grant abstracts to unpack the language that researchers in this field use to describe their work to funding agencies, and how that rhetoric shapes the field itself.

Introduction

Kinetic energy is put into the ocean by winds and tides, and the ocean responds by moving at a variety of spatial scales and frequencies. This thesis focuses on the mechanisms by which kinetic energy and momentum are transferred between different scales of motion. Physical mechanisms of energy and momentum transfer allow the smallest scales of motion to meaningfully influence the fate of the largest scale ocean currents, playing an important role in regulating the global climate (Ferrari et al. 2009; Melet 2022).

Kinetic energy cascades in both directions, from smaller to larger scales (inverse) and from larger to smaller scales (forward). It inhabits many different classes of motion that behave and interact in a variety of ways, such as geostrophic currents, eddies, submesoscale fronts, internal waves and turbulence. Small scales of motion including turbulence and most internal waves cannot yet be resolved by regional and global ocean models. However, these small scales play an important role in balancing ocean kinetic energy and momentum budgets (Naveira Garabato et al. 2013; Polzin et al.1997). Since they cannot be resolved in models, the next best option is to understand the physics of their interactions with larger scales so that the effects can be estimated in the form of parameterizations (Achatz 2024; Polzin 1995).

Internal waves are one class of oceanic motion that draws kinetic energy from both winds and tides. Wind forcing drives internal waves at their minimum frequency and spatial scales of 10s of kms, generating near-inertial internal waves (Alford et al. 2016). When the barotropic tides encounter topography, they generate internal tides that can freely propagate as internal waves at the semidiurnal or diurnal frequency depending on their latitude (Wunsch 1975). Once forcing mechanisms have generated these low-frequency large-scale internal waves their energy enters a forward cascade, transferring to smaller and smaller frequencies until it is dissipated and converted to heat and potential energy (Olbers 1976; Müller et al. 1986; Polzin 1995; Dematteis et al. 2021). The momentum carried by internal waves can be transferred to larger scale currents once turbulence has been initiated by instability (Andrews and McIntyre 1976). Internal wave breaking thus transfers kinetic energy to smaller scales and momentum to larger scales.

Turbulence generated by internal wave breaking contributes to the irreversible mixing of dense water with the lighter water above it. This mixing is thought to contribute to upwelling along ocean boundaries, supplying the available potential energy that fuels the global overturning circulation (Munk 1966; Ferrari 2016). In my first chapter, I will present observations of kinetic energy cascade above the steep sloping boundary within a submarine canyon. Using a coarse graining method that is relatively new to oceanography (Aluie et al. 2018), I present the first ever direct observations of kinetic energy cascade at internal wave frequencies. Our observations show that the strongly nonlinear internal wave breaking in the canyon transfers kinetic energy to turbulence faster than it would be transferred by open ocean dynamics. Correctly parameterizing the influence of topographic interactions in down-scale kinetic energy cascade could unlock more realistic upwelling representations in ocean models.

The generation of turbulence during internal wave breaking allows momentum to be transferred from the wave to the background flow (Eliassen and Palm 1961; Andrews and McIntyre 1976). In my second chapter, I present observations of near-inertial wave breaking in the Gulf Stream. Due to the combined effect of Doppler shifting and geostrophic vorticity only against-stream waves will ever break, leading to a net drag (Kunze 1985; Olbers 1981). I compute an upper bound on the resulting momentum transfer which would cause a local flow deceleration of 3cm/s. Using ray tracing, I expand the parameter space to account for the range of near-inertial waves that could be produced from a variety of wind forcing. The upper bound on near-inertial wave drag indicates an equal significance to previously identified momentum sources and sinks for boundary currents such as the Gulf Stream (de Marez et al. 2020; Gula et al. 2015). This previously unidentified mechanism represents a sink of momentum for large scale ocean currents that is currently unaccounted for in models. Near-inertial wave drag parameterizations could contribute to a more accurate representation of the Gulf Stream in models in the future.

Observations allow us to augment and verify our understanding of complex ocean physics, which would otherwise be based entirely on theoretical studies and modelling. Turbulence occurs sporadically and on scales ranging from meters to centimeters, making it challenging to observe (MacKinnon et al. 2017). In my third chapter I present a novel design for the turbulence sensing shear probe, which has remained unaltered for over 50 years (Lueck 2002). The newly ocean-tested design replaces the fragile crystalline sensing element with a polymer that is much more durable. The increased durability will make shear probes a better candidate for large-scale observation programs that rely on non-expert deployment, like ARGO and GO-SHIP (Roemmich et al. 2019). Inclusion in large-scale open access observation campaigns would make turbulence data accessible to wider variety of users, outside of the handful of labs which are able to operate their own microstructure platforms (Le Boyer et al. 2023).

Engineering challenges are not the only hurdle for scientists to overcome to make ocean observations. The ever-evolving landscape of federal funding is another maze that must be navigated on the pathway to scientific progress. In my fourth and final chapter, I examine the historical and contemporary language used by oceanographers to describe their research when advocating for military funding. With a specific focus on the origin and uses of the categories basic and applied, I unravel some of the functional roles of language in SIO grant abstracts from the time period 2015-2025. This work examines how language can be used to obfuscate our positionality as scientists, how the stories we choose to tell about our fields can define the way students interact with them, and how rhetoric is used to construct a relationship between science and impact.

Taken together, all four chapters tell a story of how change is communicated across scales; how dynamics at the smallest scale can alter the fate of large systems.

Chapter 1 : Pathways to Turbulent Dissipation in a Submarine Canyon

1.1: Introduction

Turbulent mixing on small scales drives the abyssal part of the global ocean circulation by upwelling deep water (Munk, 1966; Wunsch & Ferrari, 2004). Kinetic energy (KE) imparted to internal waves by wind and tides is thought to cascade to smaller scales and higher frequencies until turbulent motions dissipate it as heat or convert it to available potential energy (Gregg, 1989; Henyey et al., 1986; Olbers, 1976). Understanding the transfer of energy between scales is thus fundamental to closing the global overturning circulation, and to predicting how it may evolve in a changing climate and ocean (Dematteis et al., 2024; Lumpkin & Speer, 2007).

The pathways that KE takes to dissipation in wavenumber-frequency space depend on the mechanisms that are responsible for that energy transfer. In the open ocean internal wave KE is thought to cascade downscale via weakly nonlinear wave-wave interactions. Eventually it reaches scales at which shear instability causes internal waves to break and transfer energy to dissipation. Alternatively, in more energetic environments, instabilities can occur at larger scales and energy may be transferred to dissipation without the need for wave-wave interactions to move it downscale first (Kunze et al., 2012; Moum et al., 2003; Nash et al., 2007).

Progress has been made toward characterizing the forward cascade of energy based on weakly nonlinear wave-wave interaction theory (Müller et al., 1986; Olbers, 1976). Finescale parameterizations (Gregg, 1989; Henyey et al., 1986; Polzin et al., 1995) estimate the dissipation rate by relating turbulence to shear and/or strain, assuming that conditions are similar to the GM spectrum (Garrett & Munk, 1972). Departures from this spectral shape have been accounted for in a phenomenological way (Ijichi & Hibiya, 2015; Polzin et al., 2014), but were recently successfully incorporated in the theoretical wave-wave framework (Dematteis et al., 2024; Eden et al., 2019). Dematteis et al. (2024) developed a method that determines KE transfers in wavenumber-frequency space based on wave triad interactions, hereafter referred to as the W-W method.

In parallel to progress on weakly nonlinear KE cascade theory, observations and models have identified regions with rough topography as significant sites of mixing, dissipation, and upwelling (de Lavergne et al., 2016; Ferrari et al., 2016; Polzin et al., 1997). Many of these areas are highly energetic, featuring strongly nonlinear dynamics that render finescale parameterizations invalid (Alford, 2010; Klymak et al., 2008; Kunze et al., 2002; Waterman et al., 2014). This disconnect between theoretical tools and observations leaves a gap in our understanding of the KE cascade in topographic regions where mixing is strongest, which are of leading-order importance to the upwelling branch of the meridional overturning circulation.

This study maps the transfer of KE to dissipation within a canyon as the semidiurnal internal tide (D2, encompassing multiple undistinguished tidal constituents) breaks convectively above its sloped floor. Analysis of the combined data set revealed 200 m tall overturns (Alford et al., 2024; Wynne-Cattanach et al., 2024b). We apply a coarse graining method (Aluie et al., 2018) to velocity data from a closely spaced mooring array, mapping the KE cascade in frequency space. The method uses selective low-pass filtering to determine cross frequency KE flux. Coarse grained flux is compared to dissipation from shear microstructure observations, finescale parameterizations, and the W-W method. When the internal tide is breaking, KE likely is not contained in a neatly organized internal wave continuum, but rather in some strongly nonlinear assemblage of convective billows that advect past the moorings. Unlike finescale parameterizations and the W-W method, coarse graining does not make assumptions about flow dynamics or weak nonlinearity. We find that KE is transferred directly to dissipation from lower frequencies when strong nonlinearity is allowed.

1.2: Data and Methods

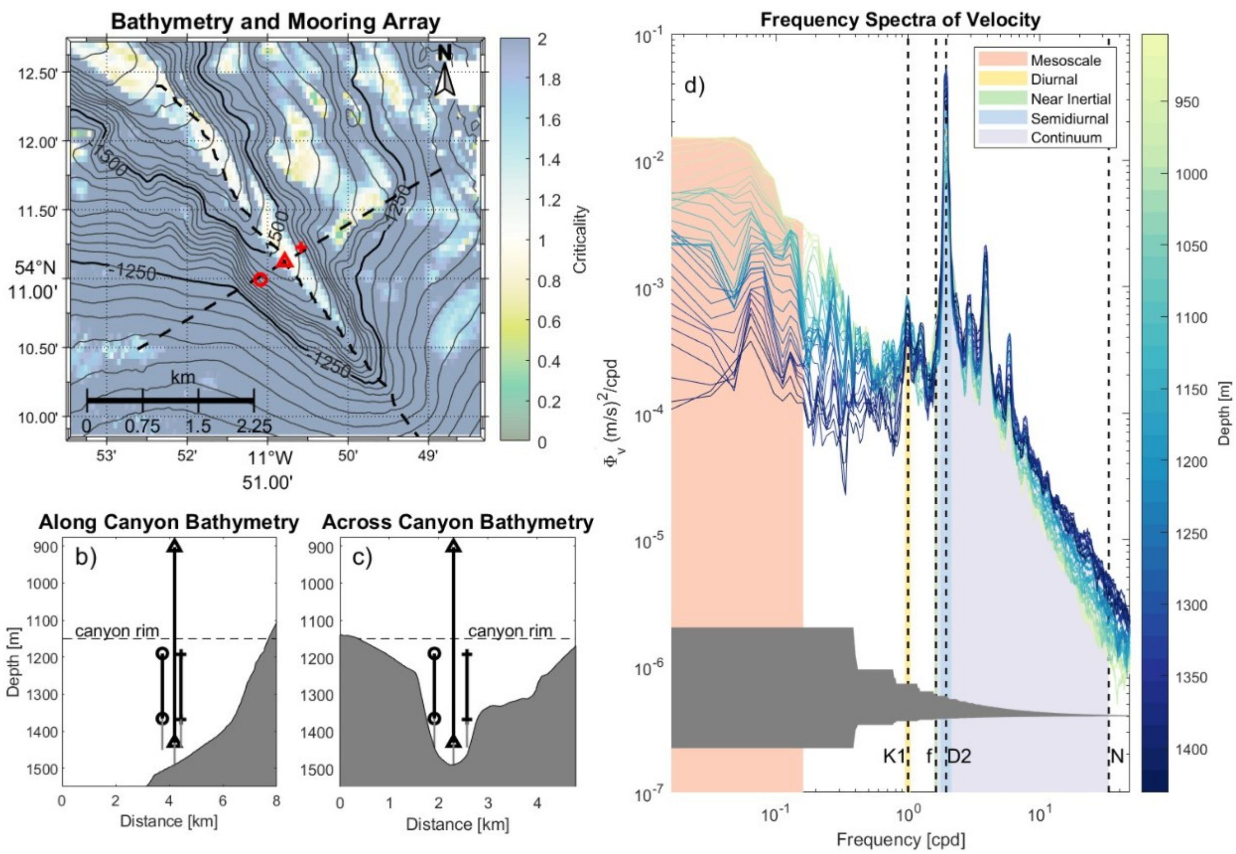

Figure 1.1: [a] Canyon bathymetry from shipboard multibeam observations. Criticality (Eq 1) with respect to D2 (color). Dashed black lines show bathymetry sections in (b) and (c). Mooring locations in red, MP3 (triangle), MAVS3 (circle), and MAVS4 (plus sign). [b] Along-canyon bathymetry with mooring ADCP ranges (thick black) [c] Across-canyon bathymetry [d] Frequency spectra of velocity at each ADCP depth bin from MP3. Depth indicated by color. Frequency bands shaded in color. Diurnal (K1), semidiurnal (D2), inertial (f), and buoyancy (N) frequencies marked with dashed lines. Grey bar indicates spectral uncertainty. Spectra WKB-scaled above f.

1.2.1: Boundary Layer Observations in a Canyon

From July 2021 through August 2022, turbulent processes were observed in a Rockall Trough canyon during the Boundary Layer Turbulence (BLT) project (Alford et al., 2024;

Wynne-Cattanach et al., 2024b). Three moorings, referred to as MAVS3 (circle markers), MP3 (triangle markers), and MAVS4 (plus markers), were deployed in a critically sloped section for 10 months (Figure 1). Each was equipped with a downward looking Acoustic Doppler Current Profiler (ADCP). MP3 included a McLane Moored Profiler (Doherty et al., 1999) set to transit the 530 m cable every 3 hr, providing co-located CTD and ADCP velocity data for 3 weeks in July 2021, after which it stopped profiling due to mechanical failure. Ship-based shear microstructure profiles were obtained using the epsilometer (Le Boyer et al., 2021) over 130 collective hours of sampling during July 2021 and 213 hr during August 2022. Observations from within 2 km of MP3 are used to create a mean profile of the turbulent dissipation rate of KE, ϵ.

Criticality, s, shown in (Figure 1a), impacting the nature of internal wave breaking on topographic slopes, is defined by the ratio of the slope, α, to the characteristic slope of the tide.

$$s = \frac{\alpha}{\sqrt{\frac{\omega_{D2}^2 - f^2}{N^2 - \omega_{D2}^2}}} \tag{1.1}$$

where ω_{D2} is the semidiurnal (D2) tidal frequency, f is the local inertial frequency, and N is the mean buoyancy frequency. A critical slope, resulting in parallel reflection and breaking (Eriksen, 1982; Wunsch, 1969), is defined as s = 1.

1.2.2 Spectral Analysis

1.2.2.1 WKB Scaling

As internal waves propagate, their amplitude and vertical wavelength change in response to changes in stratification. To compensate for this refraction, allowing comparison of internal wave velocities across the water column, the velocity data are WKB-scaled as below following Leaman and Sanford (1975):

$$U_{WKB}(z,t) = U(z,t)\left[\frac{\langle N\rangle}{N(z)}\right]^{1/2} \quad 1.2$$

where U = [u, v, w] is velocity from the ADCP, N(z) is the mean buoyancy frequency at each depth, and ⟨N⟩ is depth-mean buoyancy frequency. Ship-based repeat CTD casts from September 2021 are used to compute the mean N profile.

1.2.2.2 Time Mean Spectra and Kinetic Energy

Frequency spectra of complex velocity (Gonella, 1972) are computed with velocity data from MP3 using Welch's method with 50% overlapped Hanning windows, each containing 60 days of data. After subtracting the instrument noise floor of 7×10^{-6} $(m/s)^2$/cpd estimated from observed spectral whitening at the highest frequencies, KE is computed by integrating the unsmoothed spectrum, $\phi(\omega)$, over a discrete band, where A and B denote band limit frequencies:

$$KE_{AB} = \int_{B}^{A} \varphi(\omega)\partial\omega \quad 1.3$$

Following Le Boyer and Alford (2021), continuum KE is estimated by integrating over a best fit of the GM spectrum (Garrett & Munk, 1972) to the high frequency continuum ($\omega > 8$ cpd), rather than the observed spectrum, to minimize contamination by tidal harmonics.

1.2.2.3 Wavelet Analysis

Continuous wavelet transforms are used to produce a time-frequency record of wavelet energy density from ADCP data. Wavelet transforms reveal the frequency content of a signal in time by convolving the data with a wavelet that is compact in frequency and time (Kumar & Foufoula-Georgiou, 1997; Torrence &Compo, 1998).

1.2.3 Finescale Parameterization

Finescale parameterizations estimate dissipation from velocity shear and/or vertical strain, assuming energy is transferred downscale by internal waves interacting in a GM-like field (Gregg, 1989; Gregg et al., 2003; Henyey et al., 1986; Polzin et al., 1995). We use the version of the finescale parameterization presented by Gregg et al. (2003), which uses both shear and strain spectra, hereafter referred to as GHP. Wavenumber spectra of shear and strain are computed using data from the ADCP and CTD mounted on the McLane Moored Profiler. Strain, $\xi_z = N^2(t, z) / \langle N^2(z) \rangle$, is computed from time variations in N, the buoyancy frequency. Shear, $S = \partial(u, v) / \partial z$, is computed over10 m bins centered around each 2 m McLane depth bin due to the 10 m resolution of McLane velocity data (Alford, 2010). Wavenumber spectra of shear and strain are computed over 150 m bins using Welch's method with no windowing.

1.2.4 Coarse Graining

Aluie et al. (2018) applied a coarse graining method to oceanography which, unlike GHP, makes no assumptions of stationarity, statistical homogeneity, scale invariance, or degree of nonlinearity. WKB-scaled velocity data is low-passed at a spatial scale of interest, l, and applied to the rotating Boussinesq equations of motion. A KE budget for scales >l is derived which includes a term, Π_l, for the transfer of energy to scales <l. The full equations of motion can describe the low-passed field in detail, but we compute only one term of the KE budget, Π_l, describing coupling to smaller scales. Cross-scale interactions between velocity and pressure terms are neglected by this method. Like some other studies (Barkan et al., 2021; Naveira Garabato et al., 2022) we coarse grain infrequency space. Rather than at spatial scale, l, we low-pass at frequency scale, ω. Cross-frequency kinetic energy flux, Π_ω, is defined as:

$$\Pi_{\omega}(\mathrm{x,y,z,t}) = -\frac{1}{2}(\nabla\overline{\boldsymbol{u}}_{\omega} + \nabla\overline{\boldsymbol{u}}_{\omega}^{T}) : (\overline{\boldsymbol{u}\boldsymbol{u}}_{\omega} - \overline{\boldsymbol{u}}_{\omega}\overline{\boldsymbol{u}}_{\omega}) \qquad 1.4$$

where **u**(x, y, z, t) = (u, v, w) is the velocity at time t and location (x, y, z). ∇ is a 3D gradient, superscript T is a transpose operator, : is a tensor inner product, and over-line with subscript ω signifies low-passing. Π_{ω} gives the scalar magnitude and direction (± to higher/lower frequency) of KE flux, in W/kg, across frequency boundary ω. Equation 4 is computed at each sample in space and time (every 16 m in depth, 425 m horizontally, and 15 min intime). Gradient terms are computed by interpolating onto shared depths and times, calculating the velocity gradients between mooring pairs, and then averaging between pairs. Vertical velocity, w, signals are often too small to be measured by moored ADCPs. Because of the strong tide and the topographic slope our w data has a10:1 signal to noise ratio, sufficient for our analysis.

We choose to work in frequency space due to the high time resolution and low spatial resolution of our data. Mathematically, this method can be applied in the same way to temporal or spatial scales (Barkan et al., 2017). Similarly to Naveira Garabato et al. (2022), the decision to do so relies on the shape of the 2D velocity spectrum. Ocean frequency and wavenumber velocity spectra are typically red, meaning that as the wavenumber of fluid motions increases, their frequency tends to increase as well. A few notable exceptions include near-inertial waves and internal tides, which occur at one frequency but can be observed at many wavenumbers (Alford, 2010; Leaman & Sanford, 1975). To maintain the validity of relating KE flux in frequency space to spatial scales, we exclude the semidiurnal tide and its first harmonic by choosing frequency boundaries ω > 4.5 cpd.

ADCP noise cannot be removed from coarse grained estimates, because they are computed at each point in space and time, rather than from a spectrum. White noise in the velocity data adds noise to the estimated flux, especially at higher frequencies, but does not contribute to an erroneous trend or bias in the results.

1.2.5 Wave-Wave Interaction Numerical Method

We compare cross-spectral fluxes from coarse graining to the Dematteis et al. (2024) method applied to the three-wave kinetic equation (Lvov et al., 2004; Olbers, 1976). As with coarse graining, it makes no assumptions of stationarity, scale invariance, or the locality in wavenumber-frequency space. Unlike coarse graining, the W-W method excludes all energy transfer mechanisms other than wave-wave interactions, under the assumption of weak nonlinearity. The W-W method takes a given wavenumber and frequency spectrum of velocity and computes the KE flux that would result from wave-wave interactions between arbitrary finite boxes in wavenumber-frequency space. Coupling between KE and available potential energy is accounted for by the W-W method because it is based on a spectral space budget for the total energy of the internal wave field. The W-W method has the potential to improve finescale parameterizations by estimating dissipation using a first principles approach, and taking into account changes in spectral slope which reflect a diverse range of energy sources (Dematteis et al., 2024; Le Boyer & Alford, 2021; Pollmann, 2020; Polzin & Lvov, 2011).

Due to computational expense, we restrict bins in frequency space to three boundaries, at 2.7, 8, and 20 cpd. The W-W method excludes tidal harmonics spectrally, so the lowest boundary can be lower than for coarse graining. Coarse graining can only remove tidal and harmonic contamination by the choice of frequency boundary because it is not a spectral method.

1.3 Results

1.3.1 Depth Dependence of Time-Mean Kinetic Energy

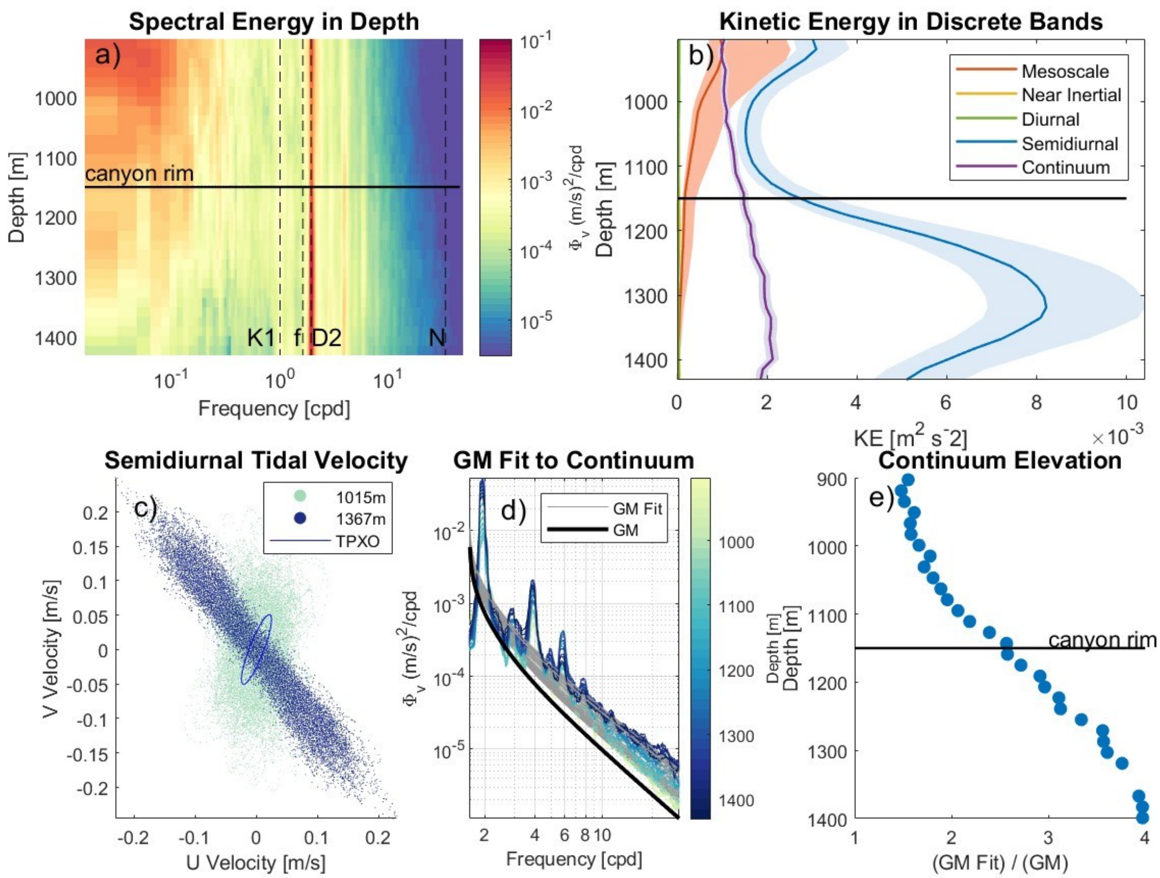

Figure 1.2: Data from MP3. [a] Frequency spectrum of velocity at each ADCP depth bin. [b] KE in select frequency bands. Near inertial (yellow) and diurnal (green) KE are negligible, falling on the zero axis at this scale. [c] Semidiurnal band-passed velocity components at one depth above the canyon (1015 m) and one within (1367 m). TPXO barotropic tidal ellipse overlaid. [d] Frequency spectrum of velocity at each depth bin at continuum frequencies. GM spectrum (thick black) and best fits to each spectrum above 8 cpd (thin grey). [e] Elevation of continuum as ratio of GM fits over GM.

D2 is the dominant KE source below the canyon rim (Figure 2a). By integrating across sub/mesoscale, diurnal, near-inertial, semidiurnal, and continuum bands, we can see how KE changes with depth (Figure 2b). Sub/mesoscale (62–6 day periods) KE signals are strongest above the canyon, but decrease rapidly below the rim. Neither the diurnal nor the near-inertial band contributes a significant KE signal.

Tidally band-passed (1.2 - 3.0 cpd) velocity is plotted at one example depth above the canyon (1,015 m) and one within (1,367 m) (Figure 2c). Semidiurnal velocities exceed barotropic predictions from TPXO tide models (Egbert & Erofeeva, 2002) at all depths, and are greatest within the canyon, indicating an internal tide. The D2peak contains the most KE at all depths, and is maximum within the canyon at a depth of 1,300 m. We believe this is due to the criticality of the canyon floor with respect to D2 (Figure 1a).

Some D2 KE cascades to higher frequencies and is dissipated, so unless it transfers directly from the tide to dissipation it must be observable in continuum frequencies. Fitting the GM spectral shape to the observed velocity spectrum above 8 cpd shows that continuum KE is elevated above the predicted GM spectrum (Figure 2d). The elevation of continuum KE increases with depth to 4 times GM (Figure 2e). This increase suggests that more KE is passing through continuum frequencies at depth, where we expect internal tide breaking to play a more important role in energy transfer.

1.3.2 Timescales of Kinetic Energy Transfer

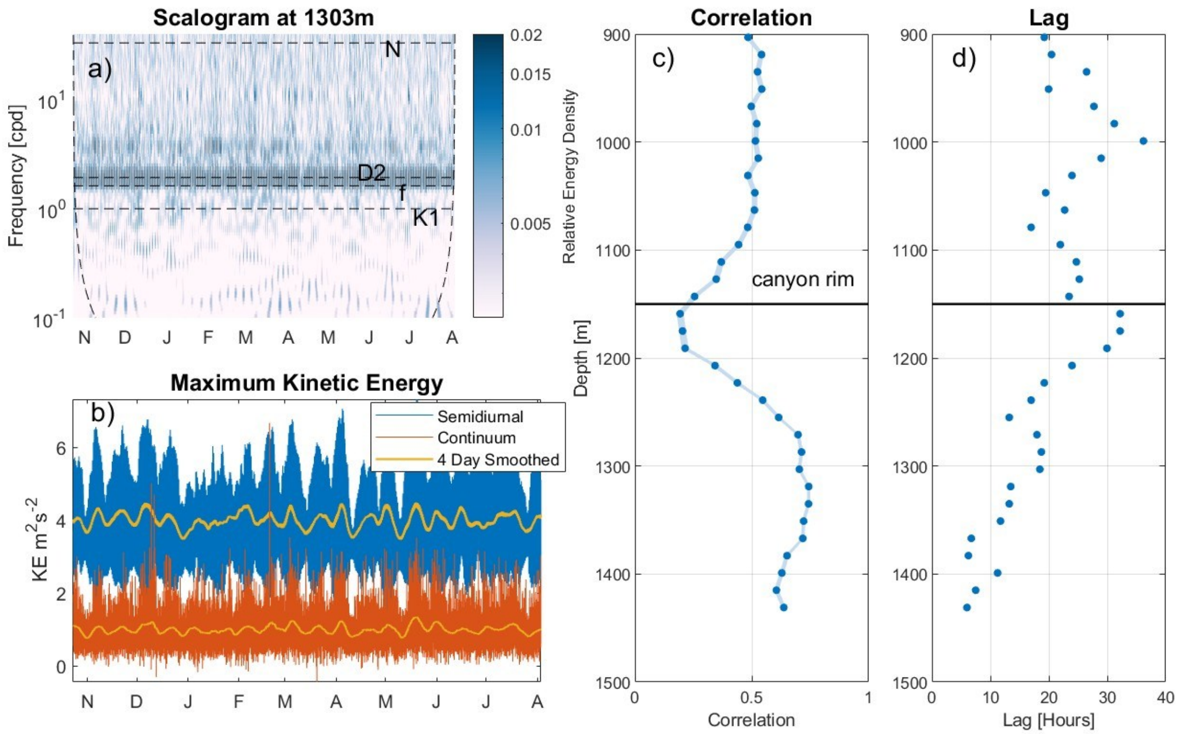

Figure 1.3: [a] Sample scalogram at 1303m depth [b] Peak KE in D2 and continuum bands normalized by the time-mean and shifted 2 m2s−2 for visibility [c] Correlation between D2 and continuum, with shaded 99% confidence interval (so narrow that it appears to be a line connecting the markers) [d] Lag at maximum correlation between D2 and continuum

We expand our analysis to frequency, depth, and time using a continuous wavelet transform at each depth, such as the example from 1,303 m (Figure 3a). The energy density in the scalogram is relative because continuous wavelet transforms do not conserve energy. Scaling to the mean KE level from spectral analysis and integrating, we produce a time record of continuum and D2 KE. A spring-neap cycle can be observed in both bands (Figure 3b). The records are smoothed over a 4-day window to isolate the spring-neap cycle and lagged cross correlation is computed, similar to Le Boyer and Alford (2021). Correlation between D2 and continuum KE is greatest within the canyon (Figure 3c).

The lag at maximum correlation decreases with depth to 6 hr (Figure 3d). D2 is the only significant KE source in the canyon, so the lag can be interpreted as the mean timescale over which KE must dissipate to maintain the observed approximate stationary state. KE is transferred to dissipation most rapidly near the floor of the canyon. Early numerical methods based on wave-wave interactions in the GM spectrum estimate timescales for KE transfer on the order of 10 - 100 days in the open-ocean (Olbers, 1976). More recent studies have identified open-ocean processes that transfer energy on a timescale of hours (Dematteis et al., 2024; MacKinnon & Winters, 2005). This study finds a timescale of KE cascade on the faster end of observed and modeled dissipation mechanisms, consistent with the vigorous observed internal tide breaking (Wynne-Cattanach et al., 2024b).

1.3.4 Pathways to Dissipation

KE cascade pathways are mapped by computing flux through discrete bins in frequency space, showing whether KE passes through continuum frequencies or transfers directly from D2 to dissipation. Before quantifying the KE pathways, we build physical intuition by placing upper and lower bounds on the amount of energy that could flux through continuum frequencies (Figure 4a, red dots). The upper bound represents dissipation of 100% of continuum KE, from Figure 2d, over the lag-based timescale from Figure 3d. The lower bound must be non-zero if we assume only forward cascade, because continuum KE oscillates in time (Figure 3b). The lower bound represents a case in which only enough KE fluxes to account for the spring-neap continuum oscillation. The next dominant frequency in the continuum is semidiurnal: much of the dissipated KE is likely transferred on this timescale. The spring-neap cycle was chosen for a conservative lower bound because it contains more continuum KE variance than any other frequency component, and has the largest correlation to D2 in time. These time-mean upper and lower estimates bound most dissipation samples (pale blue dots), building confidence.

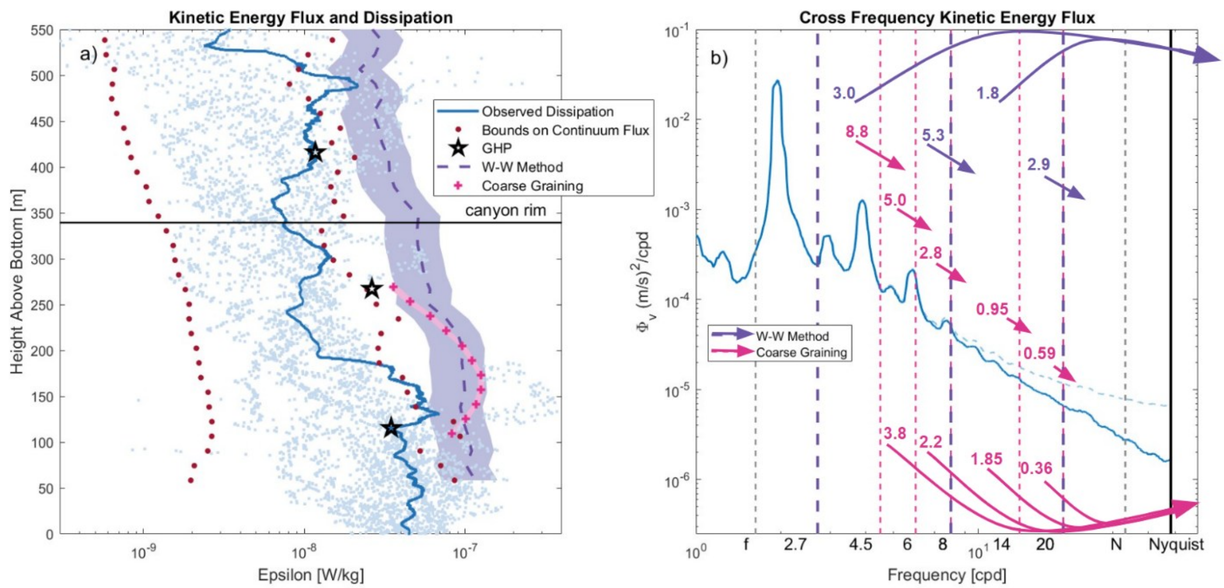

Figure 1.4: [a] Turbulent kinetic energy dissipation rate, ϵ, from microstructure observations (light blue individual estimates, dark blue mean), and GHP (black stars). KE flux through continuum frequencies from physical bounds (dotted red), W-W method flux from above 2.7 cpd (dashed purple), and coarse graining flux from above 4.5 cpd (pink plus signs). [b] KE pathways in frequency space. Short arrows show flux across (vertical dashed) frequency boundaries, longer curved arrows show flux directly to dissipation. Units are 10−8 W/kg. Depth averaged velocity spectrum without (solid blue) and with (pale dashed blue) ADCP noise.

GHP (black stars) agrees with mean observed dissipation (solid blue) and the physical upper bound (rightmost red dots), suggesting that all dissipated KE is observable in continuum frequencies (Figure 4a). The W-W method (dashed purple) and coarse graining (pink plus markers) both estimate fluxes within 3x greater than GHP, over-predicting flux through continuum frequencies and exceeding the physical bounds of the system (Figure 4a).Coarse graining cannot account for KE conversion to available potential energy, which may explain why it exceeds observed dissipation and physical bounds (Figure 4a). Coarse graining is only available at depths where velocity data from all three moorings overlaps, so it covers a narrower depth range.

Using multiple frequency boundaries, we map the KE cascade through discrete frequency bins (Figure 4b). The long arrows in Figure 4b represent flux to frequencies higher than we observed, which we assume transfers directly to dissipation. For coarse graining, direct dissipation is computed from the convergence of flux. Unlike coarse graining, the W-W method is 2-dimensional, so for the W-W method direct dissipation is estimated from flux to high wavenumber. While the W-W method assumes that dissipation of KE is caused by direct breaking of internal waves due to shear instability, coarse graining makes no dynamical assumptions, describing only the amount of KE above and below a chosen boundary and the coupling across that boundary. It is likely, given the presence of 200 m convective overturns, that we observed the advection of strongly nonlinear features rather than internal waves, invalidating the assumptions of the W-W method and making coarse graining a more appropriate method.

The influence of strong nonlinearity in the cascade is seen by comparing coarse graining with the W-W method. Both methods estimate a similar magnitude of flux through the continuum, in agreement with time-mean observed dissipation and GHP within a factor of 3, but they show KE taking different pathways. Coarse graining shows a transfer of KE that is weighted toward lower frequencies, while the W-W method shows a more evenly distributed flux of KE from all frequency bins. Coarse graining predicts 68% of KE fluxing to dissipation from below 8 cpd, while the W-W method predicts only 34% (Figure 4b). These results suggest a cascade which relies on fewer intermediate processes before wave-breaking than open-ocean wave-wave interactions, and may transfer energy more efficiently.

1.4 Discussions and Conclusions

Coarse graining agrees with the W-W method on the magnitude of flux through the continuum, but reveals a less local pathway. The physical difference that could result in these distinct pathways is the scale at which we assume wave-breaking to occur. The W-W method does not allow strong nonlinearity, assuming that weakly nonlinear interactions must transfer energy to the scales at which shear instability will ultimately result in dissipation. By allowing for convective wave-breaking at any scale, coarse graining shows KE flux to dissipation from frequencies closer to D2. In this study, weakly nonlinear methods estimate a magnitude of dissipation similar to observations despite the invalidation of their underlying assumptions. That is not always the case in other observational studies (Alford, 2010; Klymak et al., 2008; Kunze et al., 2002; Waterman et al., 2014). Coarse graining allows us to gain a deeper understanding of the mixing processes in this strongly nonlinear environment, and may be useful in other cases where open-ocean methods are not applicable and high resolution data is available.

Regions with sloping seafloors have been identified as leading-order contributors to the upwelling branch of the MOC. Canyons play an important role in upwelling deep water across continental shelves through tidal and wind driven mixing, and are ubiquitous features in global coastlines (Alberty et al., 2017; Alford & MacCready, 2014;Hickey, 1995; Waterhouse et al., 2017). Turbulent mixing in subcritical and super-critically sloped canyons has been well studied, but quantifying the KE cascade has long been outside the reach of theory and modeling due to the complexity of the processes involved. It is likely that other critically sloped topography where internal tides are breaking may experience a similarly rapid energy cascade. The methods used here have the potential to improve the accuracy of and bound the applicability of mixing parameterizations in global climate models.

Acknowledgements

This work would not have been possible without the efforts of the Multiscale Ocean Dynamics team, and the captain and crew of the RRS Discovery. This project was funded by the National Science Foundation (grants OCE-1756264, OCE-1756324 and OCE-1756251) and the Natural Environment Research Council (grant NE/S001433/1). We would also like to thank Kurt Polzin, Eiji Masunaga, Noel Gutierrez Brizuela, Joe Skitka, and Zhiyuan Gao for their wisdom and support.

Chapter 1, in full, is a reprint of the material as it appears in Pathways to Turbulent Dissipation in a Submarine Canyon. Bellerjeau, Charlotte; Matthew H. Alford; Arnaud Le Boyer; Giovanni Dematteis; Alberto Naveira Garabato; Gunnar Voet; Nicole Couto; and Bethan L. Wynne-Cattanach, Geophysical Research Letters, 2025. The dissertation author was the primary investigator and author of this paper.

Chapter 2 : Near-Inertial Wave Drag on the Gulf Stream

2.1 Introduction

Near-inertial internal gravity waves, generated primarily by wind forcing on the surface of the ocean (Alford et al. 2016), account for approximately half of the energy in the internal wave field (Ferrari and Wunsch 2009). Most ocean mixing results from breaking internal waves. The importance of mixing for fueling deep circulation and for setting horizontal and vertical density gradients has led to an intense focus on internal waves' energetic contribution to the ocean. Several recent studies have also focused on the momentum carried by internal waves that is deposited when they break, accelerating the mean flow in the direction the wave was propagating (Muench and Kunze 1999; Pinkel et al. 2012; Shakespeare and Hogg 2019).

Near-inertial wave interactions with larger scales of motion have often been studied in the context of their energetic contributions to mixing and exchanges of kinetic energy with the mesoscale and submesoscale (Kunze 1985; Young and Jelloul 1997; Polzin 2010). Kunze et al. (1995) and Alford et al. (2025) both observe a balance between kinetic energy dissipation and flux divergence at the base of mesoscale eddies, suggestive of near-inertial wave trapping in critical layers. Barkan et al. (2021) show that the presence of near-inertial waves in realistically forced regional ocean simulations leads to depleted mesoscale energy. Using a multiscale array of moorings, Savage et al. (2025) observe energy transfers both into and out of the near-inertial wave band from lower frequency motions. Several studies have observed higher levels of shear associated with near-inertial waves on the lower vorticity side of fronts and jets (Duda and Cox 1987; Rainville and Pinkel 2004; Alford et al. 2013).

The strain and shear generated by mesoscale motions impact near-inertial wave propagation by modifying the minimum frequency at which they can freely propagate and the intrinsic frequencies of the waves themselves. Kunze (1985) explored the impacts of both of these factors on near-inertial wave propagation and breaking in a geostrophic jet using ray tracing. Essink et al. (2022) used ray tracing and observations to investigate the impact of minimum and intrinsic frequency shifting on near-inertial kinetic energy and associated turbulence within and anticyclonic eddy. Whitt and Thomas (2013) similarly used a ray tracing approach to look into the behavior of near-inertial waves in strongly baroclinic currents, like the Gulf Stream. The impact of the mesoscale eddy field on near-inertial wave propagation was observed recently in the NISKINe experiment and global drifter datasets (Thomas et al. 2024a; Conn and Callies 2026). When near-inertial waves break due to interactions with mesoscale currents, there is often minimal exchange of kinetic energy with the current itself. Kunze et al. (1995) found a 7% exchange of kinetic energy due to near-inertial wave breaking within an anticyclonic eddy. The wave-mean interaction is more significant when viewed through the lens of momentum exchange.

The generalized Eliassen-Palm flux theorem states that internal wave momentum flux, also referred to as pseudomomentum flux (Mcintyre 1981), is conserved in the absence of dissipation and nonlinearity (Andrews and McIntyre 1976). Polzin (2010) points out that this theorem only holds when the background velocity field contains at least one axis of horizontal symmetry, so we will assume that the Gulf Stream is symmetric in the along-stream coordinate, similar to Kunze (1985) and Whitt and Thomas (2013). Upon dissipation internal waves deposit their momentum in the mean flow, conserving the momentum of the combined wave-mean system and accelerating the mean flow in the direction the wave was traveling. Internal gravity waves have long been known as a source of momentum for atmospheric circulation (Eliassen and Palm 1961; Lindzen 1973; Bühler and McIntyre 1999). Atmospheric scientists have incorporated wave-mean interactions into climate modeling and weather predictions in the form of a parameterized wave-drag, (Achatz et al. 2024; Kim et al. 2003). Physical oceanographers have also identified mechanisms by which internal wave pseudomomentum flux impacts the mean flow, but have yet to develop model parameterizations based on these mechanisms. Some examples of known oceanographic wave-mean momentum interactions include internal tides forcing upper ocean circulation (Pinkel et al. 2012; Shakespeare and Hogg 2019), internal waves fueling equatorial deep jets (Muench and Kunze 1999, 2000), and topographic lee waves exerting a drag when they break locally (Bell 1975; Naveira Garabato et al. 2019; Voet et al. 2023). In this work, we explore a mechanism by which wind-driven near-inertial waves exert a drag on the Gulf Stream.

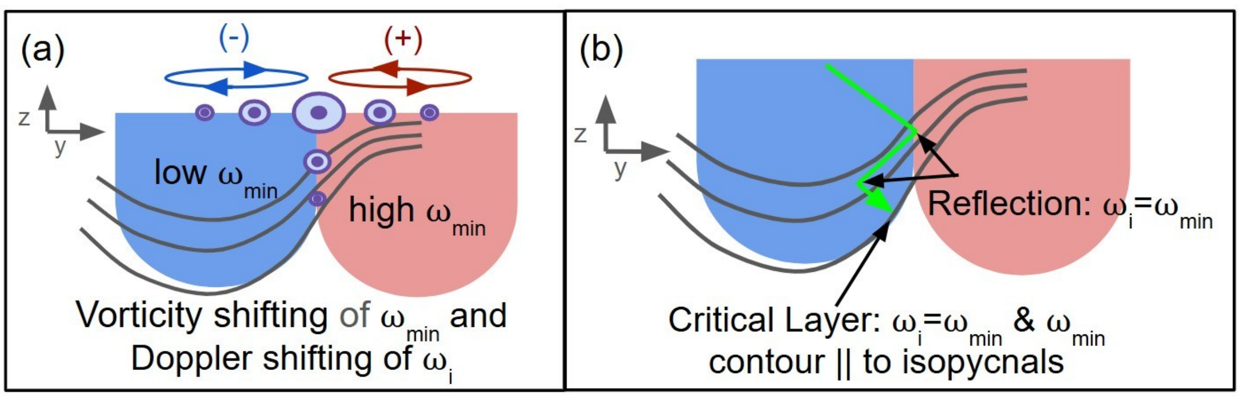

Figure 2.1: A cartoon depiction of the modifications to near-inertial wave propagation due to a strongly baroclinic jet. Isopycnals are depicted by thick gray lines sloping down to the left. The blue (red) bowl shape represents an area of negative (positive) vorticity. [a] Negative (positive) vorticity generates a regions of low (high) ω_{min}. The jet structure of the flow is indicated by the purple target symbols. Sheared velocity Doppler shifts ω_i . [b] The combined alterations of ω_{min} and ω_i determine the locations of critical layers.

Internal wave breaking occurs at critical layers, when the wave reaches the minimum intrinsic frequency at which it can propagate, $\omega_{\min}$, and is unable to reflect away, (Figure 2.1). In the absence of mesoscale influence, ω_{min} is the inertial frequency, f , which is also the frequency of waves generated locally by storms. ω_{min} can be altered by vorticity and baroclinicity that tilts the isopycnals and alters the dispersion relation of the wave (Kunze 1985; Whitt and Thomas 2013). We adopt the definition of ω_{min} derived by Whitt and Thomas (2013), which takes both vorticity and baroclinicity into account. The jet structure of the Gulf Stream introduces a complex vorticity field and strongly tilting isopycnals which both influence ω_{min}, although the vorticity effect is more significant in our case. The negative vorticity on the south side of the Gulf Stream lowers ω_{min}, and the positive vorticity on the north side raises it. The locations of near-inertial wave reflections and critical layers are determined in part by this spatially complex field of ω_{min}. Our observations show a wave propagating in from the south and reflecting off the positive vorticity of the Gulf Stream north wall. We will focus on the case study of waves generated within and to the south of the Gulf Stream, because the vorticity structure makes it less likely that a wave would be able to enter the Gulf Stream core from the north. Rainville and Pinkel (2004) observed near-inertial wave blocking on the shoreward side of the Kuroshio due to this same mechanism.

The other factor that influences the location of reflections and critical layers is the wave's intrinsic frequency, ω_i, which is Doppler shifted as the wave propagates through sheared flow. In the case of downward propagating internal waves and positively sheared mean flow, any wave with a component of propagation against-stream will have ω_i shifted down. A decrease in ω_i makes it more likely that the wave will reach ω_{min}. If $\omega_i = \omega_{min}$ in a location where the ω_{min} contour is parallel to isopycnals, like the bottom of an eddy for example, trapping will occur in a critical layer, (Figure 2.1). The group velocity of a trapped near-inertial wave will go to zero and its vertical wavenumber will increase. The shortening of vertical wavelength will eventually trigger shear instability and the wave will be dissipated, depositing its momentum in the mean flow.

Taking both the modifications of ω_{min} and ω_i into account, this study finds that only waves propagating against-stream encounter critical layers in jet-like velocity fields like the Gulf Stream. The exclusive trapping of against-stream rays was also found by the theoretical studies of Kunze (1985) and Olbers (1981). We here show an observational case study of this mechanism from a 200 km transect of the Gulf Stream and then use ray tracing to model a range of different near-inertial waves with varied starting locations, $\omega_i = 0.8\,f$ to $1.2\,f$, and initial amplitudes, $\hat{u} = 0.05$ m/s to 0.3 m/s. The preferential breaking of against-stream internal waves suggests that near-inertial waves contribute a negative acceleration to the Gulf Stream, or a near-inertial wave drag.

2.2 Observations

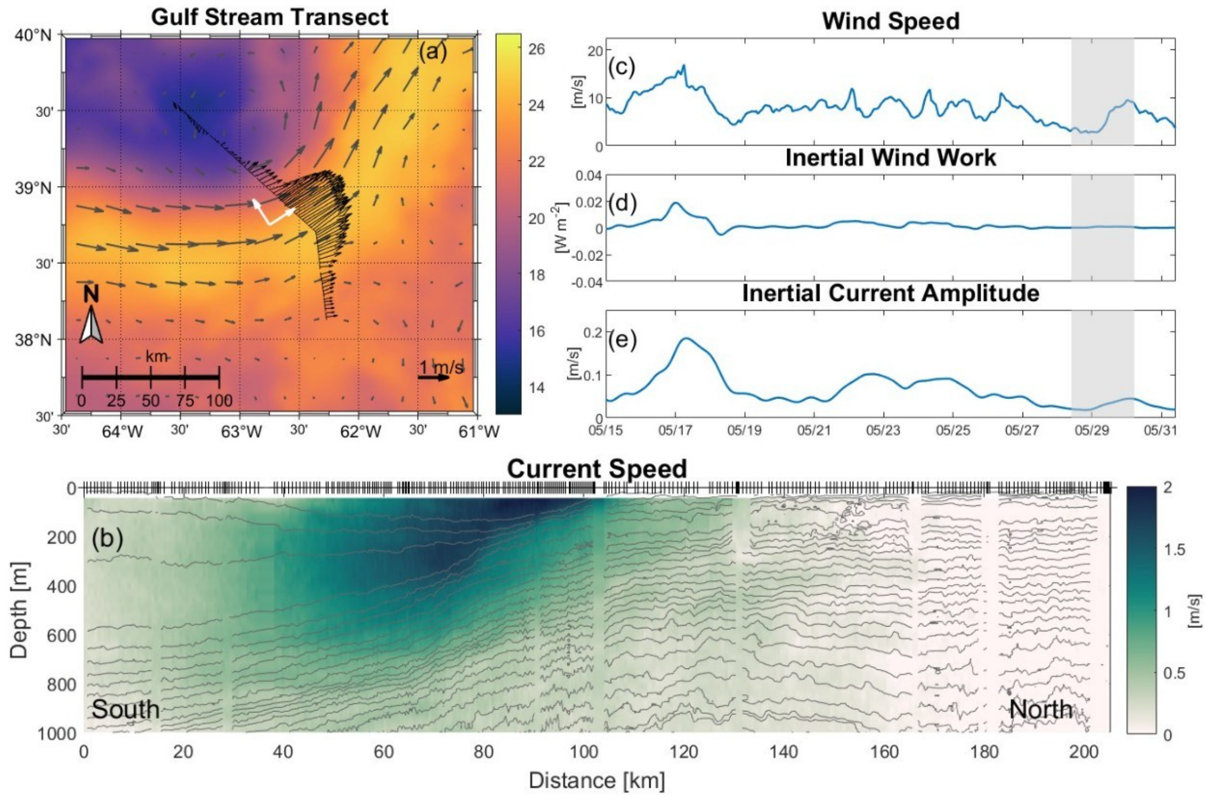

Figure 2.2: [a] Shiptrack of Gulf Stream transect with average currents from 50-70 m depth, gray arrows are geostrophic currents from CMEMS Global Total velocity, colors are temperature from the NASA Multi-scale Ultra High Resolution SST satellite product. [b] current speed from Acoustic Doppler Current Profiler (ADCP) transect with isopycnals from Fast CTD (FCTD) in gray. Tick marks at surface show profile locations. Mean [c] wind speed, [d] inertial wind work, and [e] inertial current amplitude from a slab model forced by ERA5 reanalysis wind data from -63° to -64.5° longitude and 38.5° to 39.5° latitude. Our observational period is shown in (c-f) in gray.

A 200km transect was conducted across the Gulf Stream from 10pm on May 28th to 6pm on May 30th 2023, (Figure 2a). The shiptrack is plotted with current speed from the top shipboard 38 kHz ADCP bin centered around 60m depth, as well as May 28th sea surface temperature from the NASA Multi-scale Ultra High Resolution (MUR) SST gridded satellite reanalysis product (NASA/JPL 2019) and geostrophic currents from the CMEMS Global Total velocity product (Rio et al. 2014). The Fast CTD (FCTD) profiler (Alford and Pinkel 2000) was used to collect temperature, salinity, depth, and microconductivity data at 0.5 m depth resolution from the surface to 1200 m at an average horizontal spacing of 630 m starting in the south and moving north. Velocity data were simultaneously recorded by a shipboard 38 kHz ADCP at 24 m depth resolution down to a depth of 1800 m. Current speeds reached a maximum of 2 ms^{-1} in the core of the Gulf Stream, (Figure 2.2b). We define our coordinate system with the positive y-axis facing across-stream to the north, indicated by the white arrows in Figure 2a.

Passage of a storm on May 16th generated strong wind forcing leading up to the observational period, which is indicated by the gray box in Figures 2c-e. The maximum average wind speed for the domain 63 to 64.5° W, 38.5 to 39.5° N was 17 ms−1, observed 12 days before the observational period. We use 12 days as the transit time of the near-inertial wave from the surface to the depth at which we observe it, and this timing is corroborated by ray tracing in Section 2.4.2. A slab model (Pollard and Millard 1970) forced by ERA5 reanalysis wind data shows a peak in inertial wind work and inertial current amplitudes averaged over one inertial period during the strongest wind event. The average near-inertial wave amplitude from the period modeled is $\hat{u}$ = 0.0639 ms^{-1}, similar to the observed wave amplitude of $\hat{u}$ = 0.055 ms^{-1} shown in Section 2.4.1.2.

2.3 Methods

2.3.1 Minimum Frequency

Whitt and Thomas (2013) describe the behavior of a near-inertial wave propagating perpendicular to a strongly baroclinic jet. They derive equations of motion for a time-dependent simple harmonic wave propagating through a sheared flow that take the form of the Eliassen Sawyer equation below (Sawyer 1956; Eliassen and Palm 1961):

$$(F^2 - \omega^2)\frac{\partial^2\Psi}{\partial z^2} + 2S^2\frac{\partial^2\Psi}{\partial z\partial y} + N_g^2\frac{\partial^2\Psi}{\partial y^2} = 0 \qquad 2.1$$

with geostrophic flow parameters $F^2 = f(f - \frac{\partial u_g}{\partial y})$, $S^2 = f\left(\frac{\partial u_g}{\partial z}\right) = -\frac{\partial b_g}{\partial y}$, and $N_g^2 = \frac{\partial b_g}{\partial z} = -(\frac{g}{\rho})(\frac{\partial \rho}{\partial z})$, where ρ is density, f is the local inertial frequency, and g is the acceleration due to gravity. The coordinate system (x, y, z) is oriented so that the x-axis is along-stream, the y-axis is across-stream, and the z-axis is up, as indicated by the white arrows in Figure 2a. Geostrophic along-stream velocity u_g and buoyancy b_g are computed by low-pass filtering observed ADCP velocity and FCTD buoyancy at 25 km horizontal scales and 150 m vertical scales to remove ageostrophic signals. These scales represent the horizontal and vertical wavelength of the near-inertial wave computed in Section 2.4.1.2. The time oscillating part of the equation of motion is represented by $\psi(x, y, z) = \Re(\Psi(y, z))e^{-i\omega t}$), where ω is the Eulerian frequency of the wave and t is time.

The dispersion relation derived from Equation 1 takes into account both the vortical and baroclinic effects of the mean flow's shear and strain. See Whitt and Thomas (2013) for a complete derivation and an insightful physical description of near-inertial wave behavior in critical layers without Doppler shifting; in their formulation, the Doppler shift vanishes because the waves propagate normal to the mean current. We here leverage an adapted version of their ray tracing software (Whitt and Thomas 2013; Whitt et al. 2018) to characterize near-inertial wave behavior with Doppler shifting.

The minimum frequency for a near-inertial wave in the presence of vortical and baroclinic effects is defined as:

$$\omega_{min} = f\sqrt{1 + Ro_g - Ri_g^{-1}} \qquad 2.2$$

where $Ro_g = \zeta_g / f$ is the Rossby number with geostrophic vorticity $\zeta_g = \frac{\partial v_g}{\partial \mathrm{x}} - \frac{\partial u_g}{\partial \mathrm{y}}$

, and $Ri^{-1}{}_g = \frac{f^2 N_g^2}{S^4}$ is the inverse geostrophic Richardson number. We use Equation 2 to compute ω_{min} at every point in our transect. For waves propagating along isopycnals and in the case of no baroclinicity, the minimum frequency would reduce to $\omega_{min} = \mathrm{f} + \frac{\zeta_g}{2}$ (Kunze 1985; Young and Jelloul 1997). The dominant effect on ω_{min} in the case we observed is vorticity, which creates a region of lowered ω_{min} south of the Gulf Stream core.

2.3.2 Intrinsic Frequency

The intrinsic frequency of the wave, ω_i, is the frequency measured when following the flow. We compute ω_i for our observed wave using γ, the angle between each coherent shear layer and isopycnals from FCTD/ADCP observations. Near-inertial waves at ω_{min} force particle oscillations and shear layers parallel to isopycnals. We can tell how far a wave's ω_i is above ω_{min} based on how far its angle of oscillation is from the isopycnal angle. This method is an adaptation of Equation 31 from Whitt and Thomas (2013). To our knowledge it is the first time this method is being used to interpret observational data. We define ω_i according to:

$$\omega_i^2 = N^2\gamma^2 + \omega_{min}^2 \qquad 2.3$$

where $N^2 = -(\frac{\mathrm{g}}{\rho_0})(\frac{\partial \rho}{\partial \mathrm{z}})$ is the local squared buoyancy frequency, with average density ρ_0. While Eulerian frequency is conserved for internal waves propagating through a varying medium, intrinsic frequency is Doppler shifted by the horizontal and vertical shear, as defined by:

$$\frac{\partial}{\partial r}\omega_i = -\frac{\partial}{\partial r}(\boldsymbol{k} \cdot \boldsymbol{u}) \qquad 2.4$$

with wavenumber **k** = (k, l, m), non-wave velocity **u** = (u_{al} , v_{cr} , w), and direction of wave travel r. The cross-stream and vertical components of velocity are negligible for the geostrophic flow, and we assume any gradients in the along-stream direction are negligible, similar to (Whitt and Thomas 2013; Kunze 1985). Patibandla et al. (2025) highlighted the importance of accounting for curvature of fronts in near-inertial wave propagation, but that effect is outside the scope of this study. The dispersion relationship developed by Kunze (1985) showed that the strain and shear of an axially symmetric flow only impact the wavenumber in the non-homogeneous directions of the flow, so k is constant. The Doppler shift along a ray is then:

$$\frac{\partial}{\partial r}\omega_i = -k(\nabla u_{al} \cdot \boldsymbol{r}) \qquad 2.5$$

where **r** is the unit vector in the along-ray direction.

For our observed near-inertial wave, we only have a vertical profile of ω_i computed using Equation 3. Because of this, we can only account for Doppler shifting by vertical shear. Assuming that the horizontal wavenumber and direction of the flow remain constant, the change in ω_i due to vertical shear only can be written as: $\frac{\partial}{\partial \mathrm{z}}(\omega\mathrm{i}) = -\mathrm{k}\cos(\varphi)\frac{\partial}{\partial \mathrm{z}}(u_{al})$, where φ is the angle between the near-inertial wave propagation and the flow. This version of the Doppler shifting equation is used in Section 2.4.1.2.

2.3.3 Ray Tracing

The position and wavevector of the near-inertial wave are governed by the equations, (Lighthill 1978):

$$\frac{\partial \boldsymbol{r}}{\partial t} = \boldsymbol{c}_g + u \qquad 2.6$$

$$\frac{\partial \boldsymbol{k}}{\partial t} = -\nabla\omega_i \qquad 2.7$$

where $\boldsymbol{c}_g = (c_{gx}, c_{gy}, c_{gz})$ is the group velocity of the wave. We adopt the ray tracing approach and software used by Whitt and Thomas (2013), with the addition of modifying ω_i at each time-step according to Equation 2.5.

This ray tracing method was developed using the WKB assumption that the scales of the wave are much smaller than scales on which the background flow field varies. This assumption is on tenuous footing in the case of a near-inertial wave in the Gulf Stream, especially in regards to its horizontal scale of 40 km computed in Section 2.4.1.2. The scale separation problem was also noted by Whitt and Thomas (2013) and Kunze (1985). Both of these authors used a ray tracing approach in similar conditions, and both compared their results to numerical solutions and found them to be in close agreement. Young and Jelloul (1997) predicted an ω_{min} shift due to mesoscale strain identical to that of Kunze (1985) without using WKB assumptions for spatial scale, instead relying on time scale separation. These authors did not take the effect of baroclinicity on ω_{min} into account. The dominance of the vortical effect on our ω_{min} spatial variation may salvage the validity of our ray tracing even in the case of narrow scale-separation. Regardless, many studies have demonstrated the usefulness of WKB theory beyond its formal validity bounds (Thomas et al. 2024b; Qu et al. 2021), and so we proceed cautiously.

2.3.4 Kinetic Energy Dissipation Rate

The microconductivity probes on our FCTD cannot directly measure the rate of kinetic energy dissipation, ϵ. They are designed to measure small scale vertical variations in conductivity, which are then used to derive the rate of dissipation of temperature variance, χ. ϵ and χ are expected to be related for mechanically driven turbulence when stratification is dominated by temperature (Osborn and Cox 1972; Osborn 1980). We can leverage that relationship to compute ϵ from χ if we assume we are measuring isotropic steady-state turbulence with constant mixing efficiency, and that within the turbulence there is a balance between shear production, buoyancy production and dissipation. Alford and Pinkel (2000) and Moum and Nash (2009) describe a method to compute ϵ from χ under these assumptions and taking into account the limited vertical resolution provided by a rapidly profiling instrument. They define ϵ in terms of χ as:

$$\epsilon_\chi = (2\Gamma c)^{\frac{-1}{p+1}} \left[\frac{g}{\rho_0} \frac{\hat{\chi}}{N^2} (1 + \frac{1}{R_\rho}) \right]^{\frac{1}{p+1}} \qquad 2.8$$

where $p = -0.4$ and $c = 5\times10^{-5}$ are power law constants determined by the ratio of the theoretical Batchelor spectrum that is resolved for different values of ϵ. χ is the temperature variance dissipation rate estimated from the part of the Batchelor spectrum that can be resolved by the available observations. Γ is the mixing efficiency, which we assume to be 0.2. $R_\rho = \alpha(\frac{\partial \mathrm{T}}{\partial \mathrm{z}}) \,/\, \beta(\frac{\partial \mathrm{S}}{\partial \mathrm{z}})$ is the density ratio with temperature T, salinity S, $\alpha = -1\, \rho_0\, (\frac{\partial \rho}{\partial \mathrm{T}})$ and $\beta = \frac{1}{\rho} (\frac{\partial \rho}{\partial \mathrm{S}})$, describing the tendency for the density gradient to be set by either temperature or salinity. Our FCTD transect has a mean R_ρ of 6.7±0.012. The density gradient is controlled by temperature in 80% of the observed transect. The appendix of Alford and Pinkel (2000) does an excellent job of deriving Equation 8 if the reader is craving more detail. A similar method is used by Moum and Nash (2009) to compute ϵ_χ from moored fast thermistor probes.

2.3.5 Eliasen-Palm Flux

Internal wave pseudomomentum flux, also called Eliassen-Palm flux, is the combination of momentum and buoyancy flux (Eliassen and Palm 1961). It is conserved in systems with at least one degree of spatial symmetry in the background velocity field, (Polzin 2010).

Pseudomomentum flux is often used to diagnose wave-mean interaction in combination with the non-acceleration theorem, which states that the divergence of pseudomomentum flux is zero only in the absence of dissipation and nonlinearity (Andrews and McIntyre 1976). The acceleration of the zonal mean flow is equal to the divergence of the first column of the Eliassen-Palm flux tensor (Bühler 2014):

$$F_{EP} = \begin{bmatrix} 0 \\ \hat{v}\hat{u} \\ \hat{u}\hat{w} - \dfrac{f}{N^2}\hat{b}\hat{v} \end{bmatrix} \qquad 2.9$$

where hat quantities denote wave properties. F_{EP} can be computed at every point along ray paths. The three components of F_{EP} represent the flux of along-stream pseudomomentum in the x (along-stream), y (across-stream), and z (down) directions. The other 2 columns would give the fluxes of across-stream and vertical pseudomomentum, but those components do not address our question of momentum contributions to the along-stream velocity, so they are not included in this analysis.

The acceleration of the zonal mean flow is then given by the divergence of (9):

$$\nabla \cdot F_{EP} = \frac{\partial}{\partial y}\hat{v}\hat{u} + \frac{\partial}{\partial z}\left(\hat{u}\hat{w} - \frac{f}{N^2}\hat{b}\hat{v}\right) \qquad 2.9$$

When the required wave properties are not available from observations, they are computed from the polarization relations for linear internal waves: $\hat{w} = \frac{k}{m}\hat{u}$, $\hat{v} = \frac{\omega_{min}}{\omega_i}\frac{m}{k}\hat{w}$, $\hat{b} = N^2/\omega_i\hat{w}$.

In this analysis we will compute upper bounds on mean flow acceleration by assuming that the internal wave is completely dissipated, corresponding to a complete divergence of F_{EP}. This divergence is assumed to be distributed evenly over the time, depth, and horizontal distance occupied by the ray between its second to last and last reflection points, as a proxy for the location of the critical layer. Dissipation is most likely to be concentrated in the critical layer, where shear instability occurs. The mean value of F_{EP} over the estimated critical layer domain is used to make acceleration estimates from ray tracing.

2.4 Results

2.4.1 Observed Near-Inertial Wave

2.4.1.1 Wave Behavior

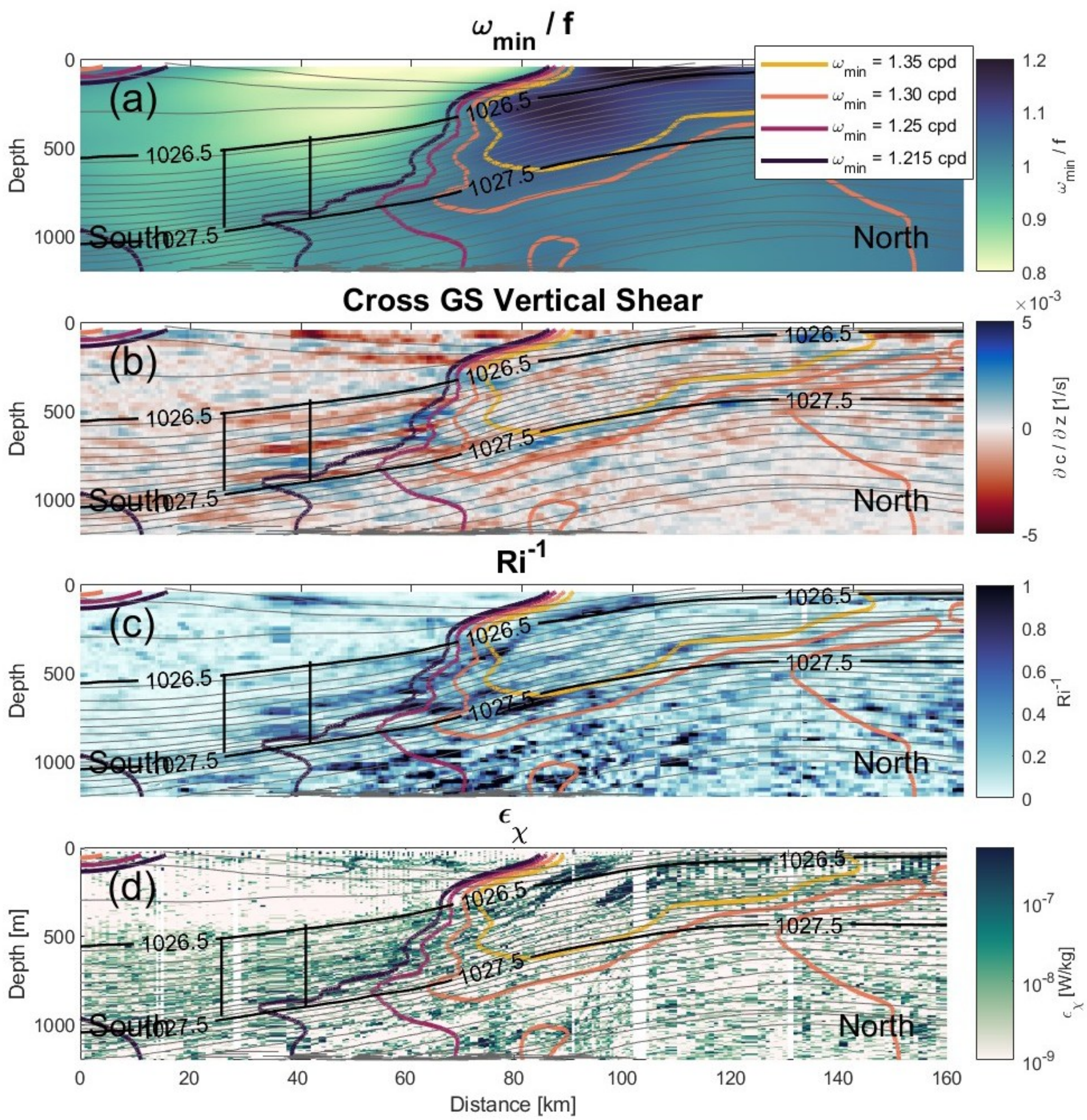

Figure 2.3: Various contours of ω_{min} over [a] ω_{min}/f , [b] cross-stream vertical shear, du_{cr}/dz [c] Inverse Richardson Number, Ri^{-1}, and [d] kinetic energy dissipation rate, ϵ_χ. 25 km smoothed isopycnals in gray with 1026.5 and 1027.5 kg/m^3 highlighted in black. The boxed domain between 30 km and 45 km is used for critical layer analysis in Section 2.4.1.2.

Examining the ratio ω_{min}/f , we can predict the behavior of downward propagating near-inertial waves, (Figure 2.3a). An internal wave is only able to propagate where $\omega i \geq \omega min$. Where $\omega_{min}/f < 1$, which only happens in the presence of vortical and baroclinic effects, waves can be generated at frequencies lower than f . A region of low ω_{min}/f is observed on the south side of the Gulf Stream, corresponding to the wall of negative vorticity associated with the jet. A near-inertial wave cannot propagate into a region where $\omega_i < \omega_{min}$, so when it hits a boundary of $\omega_i = \omega_{min}$ it tries to reflect. If the ω_{min} contour is parallel to isopycnals then it cannot reflect, and becomes trapped. These conditions are indicative of a critical layer, (Kunze 1985). When a near-inertial wave encounters a critical layer its group velocity goes to zero and its vertical wavenumber increases without bound. Narrowing of the vertical wavelength increases the probability for shear instability, triggering turbulent dissipation.

The alternating layers of shear in Figure 3b are interpreted as a near-inertial wave. The wave's shear is seen to be excluded from regions of high ω_{min} / f . Clear and coherent shear layers extend from 30 km up until the boundaries drawn by the contours of ω_{min}, and no further to the right. Upon closer inspection, the horizontal extent of the shear layers seems to be defined by contours of decreasing ω_{min} with depth, indicating that ω_i is decreasing with depth. This behavior is suggestive of Doppler shifting, the impact of which will be quantified in Section 2.4.1.2. Contours of ω_{min} are parallel to isopycnals at several locations. If $\omega_i = \omega_{min}$ at any of the locations, the conditions for a critical layer will be met, and shear instability and dissipation will be more likely.

Shear instability occurs when shear overcomes stratification, leading to overturning and unstable density gradients. High values of inverse Richardson number, $Ri^{-1} = \frac{\left(\frac{\partial u_{al}}{\partial z}\right)^2 + \left(\frac{\partial u_{cr}}{\partial z}\right)^2}{N^2}$, predict favorable conditions for shear instability (Miles and Howard 1964). $Ri^{-1} = 4$ is commonly used as a diagnostic threshold allowing shear instability in numerical modeling studies. However, due to the 24-m depth resolution of our shipboard ADCP we don't resolve enough of the shear variance at small scales to see $Ri^{-1} = 4$. Nevertheless, the ratio is still a good indicator of regions where shear instability is more likely. In Figure 2.3c, high Ri^{-1} corresponds in several locations to ω_{min} contours parallel to isopycnals. High Ri^{-1} values also correspond to regions of low stratification below the core of the Gulf Stream, which may not be indicative of internal wave dynamics. Elevated Ri^{-1} in the regions of strongest stratification and co-located with potential critical layer locations do suggest shear instability driven by the near-inertial wave. Critical layer locations also correspond to elevated ϵ_{χ}, suggesting that shear instability may be fueling dissipation, (Figure 2.3d). Regions of elevated ϵ_{χ} also appear to be co-located with decreasing contours of ω_{min} with depth.

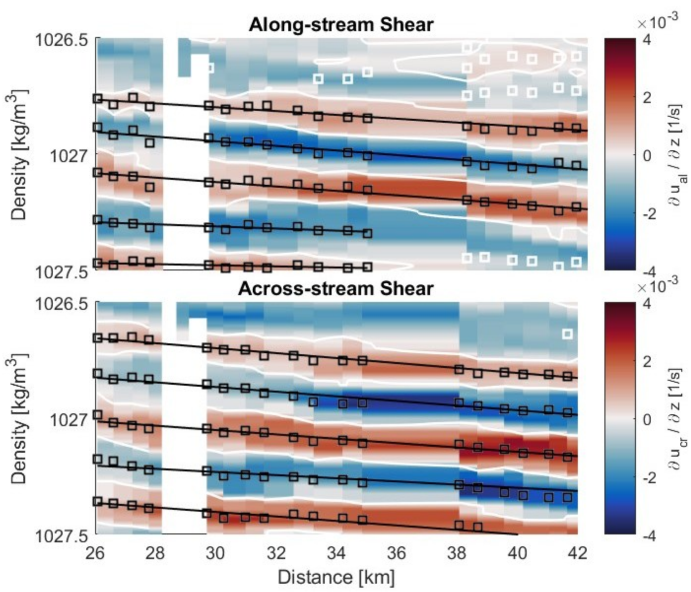

Figure 2.4: [a] $\partial u_{al} / \partial z$ and [b] $\partial u_{cr} / \partial z$ within critical layer domain in isopycnal coordinates. Contours of zero shear (white) and linear best fits to shear layers (black). Midpoints between zero contours for each profile are black squares.

2.4.1.2 Wave Properties

Now that we have observed the wave behavior that is visible in the FCTD/ADCP transect, we can use the internal wave dispersion relation to quantify some other wave properties. In order to focus on the highly coherent shear layers, we use the boxed domain in Figure 2.3 to estimate ω_i for the observed near-inertial wave according to Equation 2.3. Converting observed shear to isopycnal space, we use a linear fit to the midpoints between zero contours to compute ω_i from each coherent shear layer in a finite domain, (Figure 2.4). The centers of each shear layer, identified by black squares, are defined by the midpoints between zero contours for each profile.

The average height of shear layers defined by these contours yields a domain average vertical wavenumber m = 0.0419 1/m, corresponding to 150m vertical scales. A horizontal wavenumber of $k = 1.25\times10^{-4}$ 1/m, corresponding to a scale of 40 km, is computed by using domain-average values of ω_{min}, ω_i, m, and N^2 in the dispersion relationship for linear internal waves, $\omega_i^2 = \omega_{min}^2 + \frac{N^2k^2}{m^2}$.

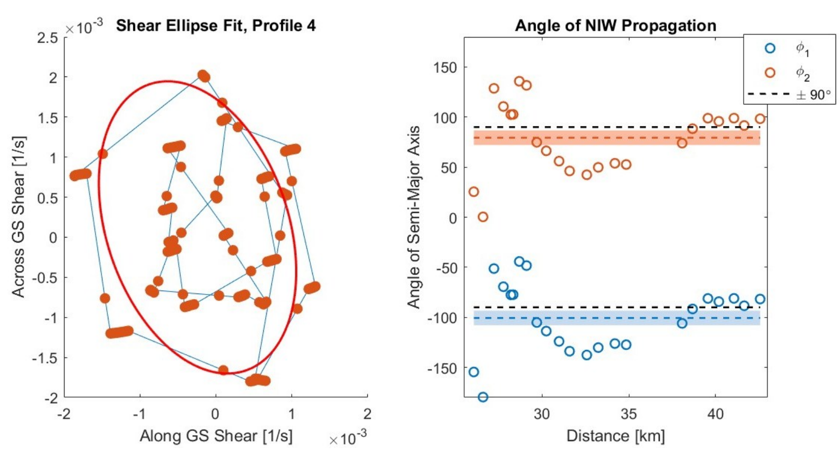

Figure 2.5: [a] Example best fit shear ellipse, and [b] angles of semi-major axes for all best fit shear ellipses. Both options for the direction of propagation, ϕ_1 and ϕ_2 are shown. Dashed black contours are ±90°from along-stream, so angles within the dashed black lines are along-stream propagating while angles outside the dashed black lines have against-stream components.

Next, we estimate the horizontal direction of propagation using the angle of the semi-major axis of the shear ellipses. An ellipse is fitted to the shear components of each profile in the boxed domain in Figure 2.3b, as shown in the sample ellipse from a single profile in Figure 2.5a. For each fitted ellipse there are two possible directions the wave could be traveling, 180° apart. We group the possible directions for each shear profile into the two options that maximize coherence between ellipses and their neighbors, (Figure 2.5b). The dashed lines show the average direction of travel, with 0° being the along-stream direction. The horizontal angle of propagation varies significantly across the 20 km of transect in our domain of focus, reflective of straining of the near-inertial wave by the strong horizontal and vertical shear of the mean flow. The shear/strain method of determining the near-inertial wave's direction of travel used by Winkel (1998) and Alford and Gregg (2001) fully determines the direction of travel, but the strain signal was too noisy in our data to use that method. We can remove the 180° ambiguity by noting that ω_i decreases with depth according Equation 2.3: Geostrophic velocity decreases with depth over this domain, so Doppler shifting would decrease ωi for a wave traveling against-stream. With this in mind, we choose $\phi_1 = -100 \pm 7.3°$ as the direction of propagation that matches the observed Doppler shift.

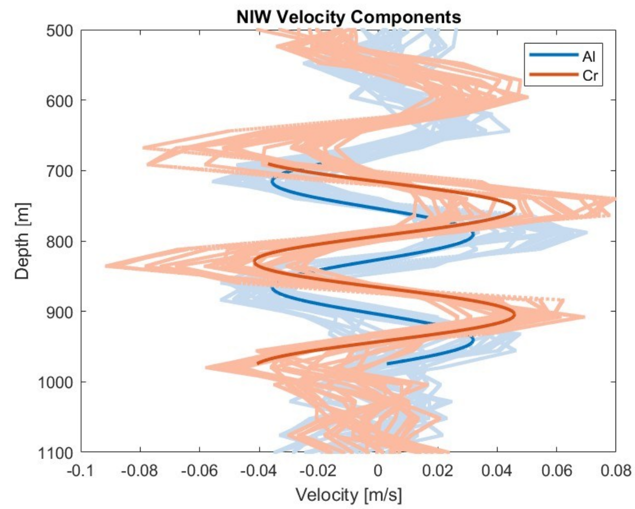

Figure 2.6: Profiles of along-stream (blue) and across-stream (red) velocity lowpassed at 600m vertical scales from within the domain in Figure 4. Best fit sine waves are plotted between 700 m and 1000 m.

The amplitude of the wave can be estimated using the ADCP data, highpassed at 600m vertical scales to remove the geostrophic velocity signal, (Figure 2.6). Best fit sine waves to all ageostrophic velocity profiles within our domain are used to estimate the amplitude of the wave, $\hat{u} = 0.055 \pm 2.1 \times 10{-}4$ m/s.

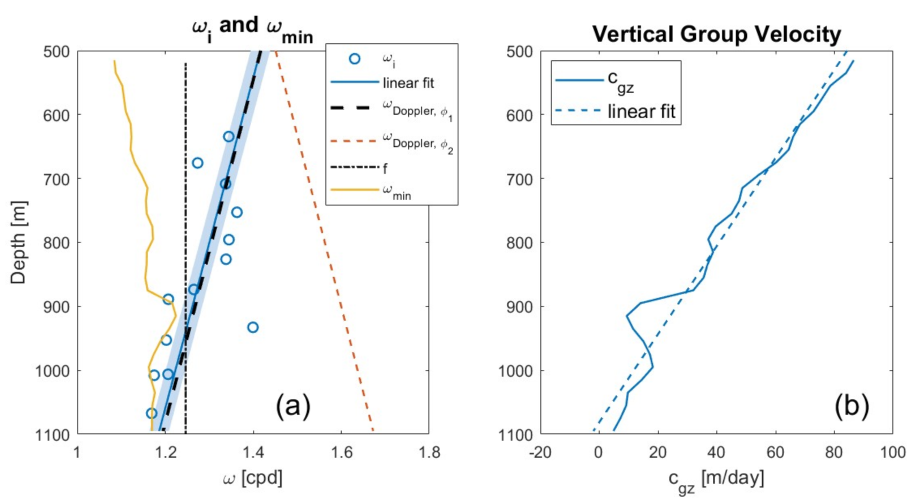

Figure 2.7: [a] ω_i from shear layer angles (blue circles) with linear best fit (solid blue, with shaded error bar), ω_i that would be expected from Doppler shifting with angles ϕ_1 (thick black dashed) and ϕ_2 (red dashed), f (black dash-dotted), and ω_{min} (yellow), [b] vertical group speed, c_{gz} (solid blue) and linear best fit (dashed blue)

The decrease in ω_i observed using Equation 2.3 is consistent with what would be expected from Doppler shifting using a mean direction of propagation $\phi_1 = -100 \pm 7.3°$, clockwise from along-stream (Figure 2.7). ω_{min} increases with depth in our domain while ω_i decreases. The combined effects of Doppler shifting and the decrease in negative vorticity with depth in the baroclinic current lead to $\omega_i = \omega_{min}$ at the bottom of our domain, (Figure 2.7a). This condition results in either a reflection or a critical layer, depending on the angle between the ω_{min} contour and the isopycnals. Referring to Figure 2.3, we can see that the contour ω_{min} = 1.215 cpd is parallel to isopycnals at 1000 m depth. The conditions for a critical layer are met at the bottom of the domain of interest. The vertical group velocity of the wave,

$$c_{gz} = \frac{\omega_i^2 - \omega_{min}^2}{\omega_i m} \qquad 2.11$$

goes to zero at the bottom of the domain, supporting the existence of a critical layer. We compute horizontal group velocity using the aspect ratio of the wave:

$$c_{gy} = -c_{gz}\left(\frac{m}{k}\right) \qquad 2.12$$

Using both components of group velocity and assuming constant kinetic energy, $KE = \hat{u}^2 + \hat{v}^2$, computed from our best fit velocity components, we compute the kinetic energy flux as $F_{\mathrm{KE}} = \mathrm{c_{gy}\,K\,E} + \mathrm{c_{gz}\,K\,E}$. APE is negleted here, with the justification that KE $\geq$ 0.9APE everywhere in our domain as $\omega_i < 1.2\omega_{min}$, (Kunze et al. 1995).

Kunze et al. (1995) noted that in the critical layer at the bottom of an eddy there was a balance between the divergence of kinetic energy flux and kinetic energy dissipation. Most of the energy delivered into the critical layer by the wave was consumed by dissipation, rather than being radiated away at other internal wave frequencies or being contributed to the mean flow. Alford et al. (2025) and Essink et al. (2022) observed a similar balance. We can compare the divergence of kinetic energy flux over our domain to ϵ_χ to assess the completeness of wave dissipation. The divergence of kinetic energy flux across our critical layer domain is computed as:

$$\frac{\partial F_{KE}}{\partial r} = \frac{\partial}{\partial y}\left(-c_{gz}\left(\frac{m}{k}\right)KE\right) + \frac{\partial}{\partial z}\left(c_{gz}KE\right) \qquad 2.13$$

Averaging over our critical layer domain, we find $\frac{\partial \mathrm{F_{KE}}}{\partial \mathrm{r}}$ $/\rho 0 = 1.9 \times 10^{-8} \pm 2.3 \times 10^{-11}$ W/kg and $\epsilon_\chi = 5.3 \times 10^{-8} \pm 4.4 \times 10^{-9}$ W/kg. The close agreement between kinetic energy flux divergence and dissipation suggests that we could be observing a complete dissipation of the wave within the critical layer. It is possible that there are other sources of kinetic energy contributing to the observed dissipation, but the available kinetic energy dissipation does not rule out complete wave divergence.

2.4.1.3 Wave Momentum Flux

Using our observations, and leveraging the internal wave dispersion relationship, we have identified the wave properties: $m = 2\pi/150 \pm 2$ 1/m, $k = 2\pi/40{,}000 \pm 11{,}800$ 1/m, $\omega_i = 9.33 \times 10^{-5} \pm 1.6 \times 10^{-6}$ rad/s, and $\hat{u}$ $= 0.055 \pm 2.1 \times 10{-}4$ m/s within our domain. Domain-averaged environmental conditions are: $f = 9.06 \times 10^{-5} \pm 4.89 \times 10^{-10}$ rad/s, $N^2 = 1.95 \times 10^{-5} \pm 6.24 \times 10^{-8}$ rad^2/s^2, and $\omega_{min} = 8.45 \times 10^{-5} \pm 4.75 \times 10^{-7}$ rad/s. As described in Section 2.3.5, we can use the polarization relations for linear internal waves to estimate the remaining variables needed to compute the Eliassen-Palm fluxes, F_{EP}, using Equation 9. We find $\hat{w} = \frac{k}{m}\hat{u} = 2.06 \times 10^{-4}$ m/s; $\hat{v} = \frac{\omega_{min}}{\omega_i}\frac{m}{k}\hat{w} = 0.0491$ m/s; and $\hat{b} = \frac{N^2}{\omega_i}\hat{w} = 4.31 \times 10^{-5}$ m/s. The observed wave properties and environmental parameters result in $F_{EP} = [0, 0.0027, 1.5089 \times 10^{-6}]$ m^2/s^2. If this flux diverged completely in the 500 m vertical scale of its critical layer and 44 km over which its shear energy is observed during half of its 12 day transit time, chosen because the critical layer domain covers half of the total vertical transit, it would result in a local mean flow reduction of 0.0334 m/s. This constitutes a 13% reduction of the 0.5 m/s flow speed at 1000 m depth. Because it corresponds to a complete flux divergence and assumes the wave is traveling entirely against-stream, this represents the upper bound of the theoretical flow deceleration by a wave with the observed parameters. In the next section we will use ray tracing to generalize this result by modeling near-inertial waves that could be generated by the range of 10 m height wind speeds for 2023 in ERA5 reanalysis data, (Hersbach et al. 2020).

2.4.2 Ray Tracing

Ray tracing is used to explore the parameter space of near-inertial waves with varied ω_i and $\hat{u}$ traveling either along or against the Gulf Stream. Theoretical waves are tested with ω_i ranging from 0.8 f to 1.2 f (1 cpd to 1.5 cpd), starting positions varying along the south side of the observed Gulf Stream transect, and initial $\hat{u}$ from 0.05 m/s to 0.30 m/s. Near-inertial waves generated at the local inertial frequency must travel south in the absence of vorticity (Garrett 2001; Alford et al. 2016). Rays are able to travel northbound here because they are above the minimum frequency and have not hit their turning latitude. The chosen parameter space for ω_i is based on possible frequencies at generation and the influence of the mesoscale on the likely range of propagation after generation, discussed further in Section 2.5.1. The range of initial $\hat{u}$ corresponds to the range of inertial current amplitudes predicted by a slab model forced by ERA5 reanalysis 10 m wind data for 2023. The distribution of wind speeds and $\hat{u}$ are shown in Figures 2.10a and 2.10b.

For each initial ω_i, starting position, and initial $\hat{u}$, one wave is tested with Doppler shifting assuming it is traveling entirely along-stream and one entirely against-stream. These are meant to be upper and lower limits on what Doppler shifting can do to the ray path and F_{EP}. As the ray is also moving in the cross-stream direction through the observed transect, it could never actually be propagating entirely along or against the flow.

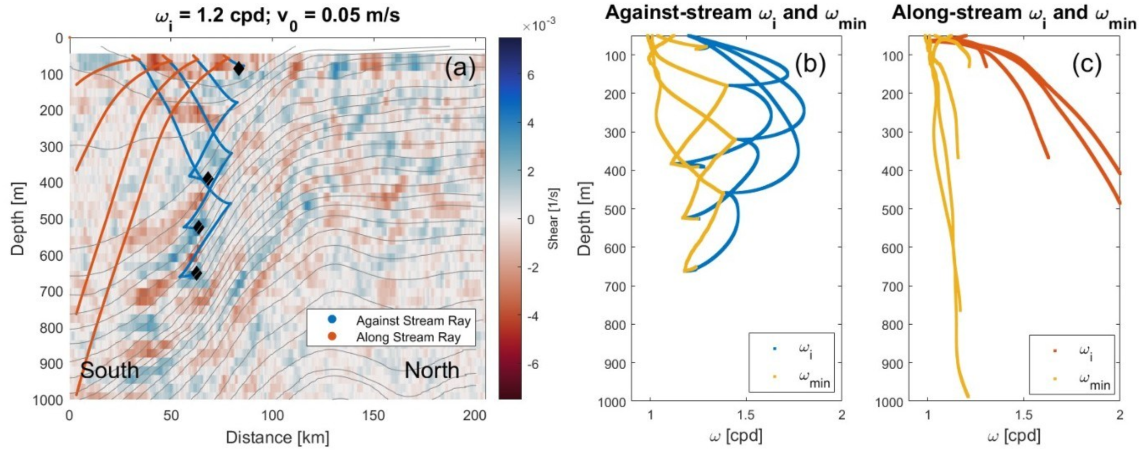

Figure 2.8: [a] Sample rays at ω_i = 1.2 cpd, with Doppler shifting assuming fully against-stream (blue) or along-stream (red) propagation. Critical layers indicated by black diamonds. [b] and [c] show ω_{min} and ω_i vs depth for against-stream and along-stream rays respectively, computed at each position along the ray paths.

Example rays with initial ω_i = 1.2 cpd and $\hat{u}$ = 0.05 m/s can help us understand the behavior expected from each theoretical wave, Figure 8. The first two ray locations from the left cannot start because their initial frequency, ω_i = 1.2 cpd, is below the local ω_{min}. These rays would have started from 1 km and 16 km. The behavior of the rest of the waves can be understood by combining the effects of Doppler shifting on ω_i and vorticity on ω_{min}, (Figure 2.8b and 2.8c).

In a current with positive shear, a wave traveling along-stream will have its frequency shifted higher, while a wave traveling against-stream will have its frequency shifted lower. The Gulf Stream has a sub-surface maximum in geostrophic velocity south of its core at around 200-m depth, meaning the shear is negative at the top of the water column. This geometry is seen in our observations, as well as other studies with more transects taken in all seasons (Andres et al.

2020). Within this negative vertical shear, the along-stream waves have their frequencies shifted down. They quickly hit the condition $\omega_i = \omega_{min}$, and their group speeds drop to zero. At this point the waves try to reflect. If the ω_{min} contour were parallel to isopycnals then the group speed would be zero on both characteristics and the wave would be unable to reflect away, signaling a critical layer. Because this is not the case, the along-stream waves reflect away soon after starting and propagate off the page, ω_i shifting up all the way. The against-stream rays initially have ωi shifted up, and do not hit the condition $\omega_i = \omega_{min}$ until they are well into the Gulf Stream core. Most of them reflect at least twice before hitting critical layers indicated by black diamonds, (Figure 2.8a).

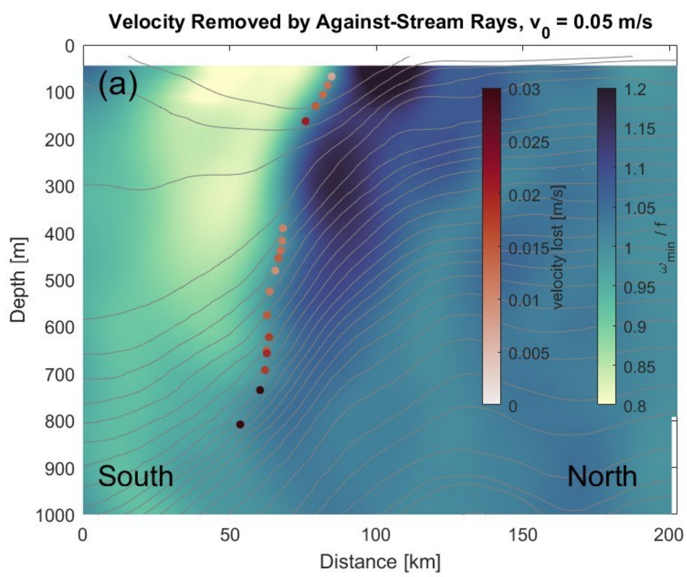

Figure 2.9: [a] $\omega_{min}/\ f$ with isopycnals in gray. Red dots show locations of critical layers with their color representing the velocity removed from the mean flow by each ray during its transit.

Considering the complete parameter space of modeled rays, we find that only against-stream rays result in critical layers. All of the critical layers fall along the sharp transition between positive and negative vorticity beneath the core of the Gulf Stream, where ω_{min} goes from greater than f to less than f . Although they are not shown, rays initially propagating south from the same locations, i.e. starting on the other characteristic, showed similar results. The spatial pattern of critical layers is consistent with many of the locations where ω_{min} contours are parallel to isopycnals in Figure 2.3, which represent a small subset of ω_{min} contours. The critical layer locations for rays with initial $\hat{u}$, = 0.05 m/s and all frequencies are plotted in Figure 9, with colors corresponding to the mean-flow velocity that would be lost due to near-inertial wave drag.

$F_{E\,P}$ is computed for each ray from Equation 2.9, and is assumed to diverge completely across the time and vertical distance between the last and second to last reflection, representative of the ray's critical layer height. The region of the dissipation is assumed to be the entire horizontal extent of the ray path, similar to the horizontal wavenumber in our observations. Waves with initial $\hat{u}$ = 0.05 m/s cause decreases in mean flow velocity up to 0.033 m/s, consistent with the estimate from the observed wave. Critical layer locations follow a similar spatial distribution for waves of other initial $\hat{u}$.

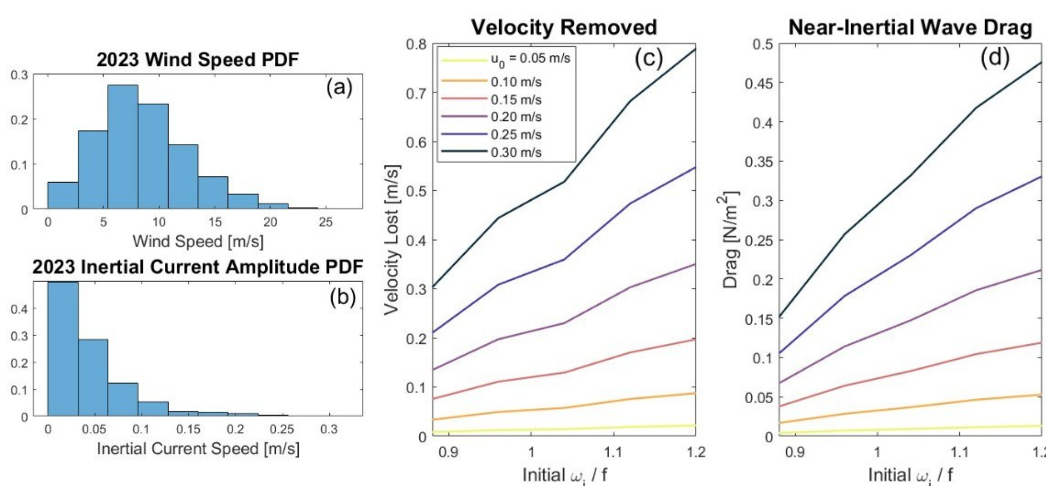

Figure 2.10: Probability density functions of [a] wind speed and [b] inertial currents predicted by a slab model forced with 2023 ERA 5 reanalysis 10-m height wind data at 64°W and 39°N. [c] Velocity removed from the mean flow according to ray tracing estimates of [d] near-inertial wave drag.

The local Gulf Stream velocity loss and corresponding near-inertial wave drag across the entire ray tracing parameter space is considered next, averaging across ray starting locations for each initial $\hat{u}$, and ω_i. The distribution of wind data and slab model inertial current amplitudes come from 2023 10 m height ERA5 reanalysis data at 64°W and 39°N, (Figure 2.10a and 2.10b). Wind speeds were most often between 5 and 10 m/s during 2023, but several storm events saw wind speeds above 20 m/s. The wind event 12 days before our observations was one of these occasions, with a maximum wind speed of 22 m/s. Despite this strong forcing, we see a wave amplitude of only 0.05m/s at the time of our observations, indicating that some KE may have been lost over the wave's 12 day transit. Near-inertial wave drag is larger for waves of increasing initial ωi and $\hat{u}$, (Figures 2.10c and 2.10d). Extreme events that force wave amplitudes of $\hat{u}$, = 0.30 m/s could cause local velocity loss of 0.8 m/s if the wave diverged completely, was oriented entirely against-stream, and had a very super-inertial frequency of 1.2 f. This combination of factors is very unlikely, as discussed further in Section 2.5.1. An initial wave amplitude of $\hat{u}$, = 0.30 m/s represents the most extreme forcing event that we see in the record for 2023. The most likely near-inertial wave events are found in the lower left corner of Figure 2.10, representing waves with initial $\hat{u}$= 0.05 m/s and $\omega_i \leq f$, which could have been locally generated on a day with average wind speeds in 2023. The upper bound of near-inertial wave drag on these days is 0.01 N/m^2, corresponding to velocity loss of 3.3 cm/s. We compare the magnitude of near-inertial wave drag to other sources of drag on the Gulf Stream in Section 2.5.3.

2.5 Discussion

2.5.1 Intrinsic Frequency Parameter Space

The parameter space of initial $\hat{u}$ used for our ray tracing study was determined by the distribution of wind forcing seen in 2023, (Figure 2.10a and 2.10b). A range of possible initial ω_i is a little bit harder to constrain. No rays are capable of starting with ω_i < 1 cpd based on the range of ω_{min}, so that sets our lower bound. The geometry and statistical path of the Gulf Stream can shed some light on how likely it is for a near-inertial wave of any initial ω_i > 1 cpd to propagate into the core. In the absence of advection or modification by geostrophic currents, near-inertial waves propagate equatorward, toward the direction of lowering ω_{min}. As they propagate down the gradient of ω_{min} they become more super-inertial relative to the local inertial frequency. To be able to propagate through the wall of positive vorticity from the north, a near-inertial wave would have to be at 1.2 f or higher. Barring any vorticity effects, it would have to come from above latitude 48.38° N, almost 10° and over 1000 km north of the average latitude of our transect. The North Atlantic only extends up to 44° N at this longitude before running into Nova Scotia, so the wave would also have had to propagate westward. We tested waves of initial ω_i from 0.8 f to 1.2 f . The Gulf Stream has an average meander amplitude of 90 km at the longitude of our transect, which is only enough to advect a near-inertial wave south by 0.81°, (Lee and Cornillon 1996). Given that the average path of the Gulf Stream moves northward about 13 km for every 100 km along its path in this region, it is more likely for waves to be advected northward than southward. These factors combine to indicate that near-inertial waves trapped in the Gulf Stream core are more likely to have initial $\omega_i < f$.

However, the geometric considerations above do not take vorticity effects into account. If anear-inertial wave is generated locally within a region of $\omega_{min} > f$ it can have $\omega_i > f$. Considering the complex field of eddies surrounding the Gulf Stream, of both positive and negative vorticity, a wide envelope of initial ω_i is possible. This field of eddies also complicates the path of any near-inertial wave that might propagate into the Gulf Stream from a remote location. Due to the synoptic nature of the wind event 12 days before our observations, it seems most likely that the wave was generated locally. A locally generated wave would have $\omega_i < 1.2 f$ at its generation, so it would be excluded from the north side of the Gulf Stream as is observed in the ADCP transect, (Figure 2.3). All of the complications discussed here lead to a high level of uncertainty in the initial ω_i of the wave we observed, and of the parameter space for waves that are likely to interact with the Gulf Stream in general. If we are ever to parameterize near-inertial wave drag in coupled ocean-climate models, this parameter space should be investigated further.

2.5.2 Implications for the Internal Wave Field

Kunze (1985) observed in their ray tracing study that near-inertial waves that propagate through the Gulf Stream are focused into beam-like paths, leading to a highly anisotropic internal wave field surrounding the Gulf Stream, and similar fronts. Other studies have similarly focused on the distortion of the internal wave field around fronts and mesoscale features, (Lee and Eriksen 1997; Duda and Cox 1987; Polzin 2008; Nagai et al. 2015; Rainville and Pinkel 2004; Alford et al. 2013). Many parameterizations of internal waves rely on assumptions of isotropy that are complicated by interactions with strong mean flows. Doppler shifting and ω_{min} alteration by mesoscale shear and strain play an important role in the distribution of internal wave energy in the North Atlantic. Whalen et al. (2012) found an excess of internal-wave-driven mixing at mid-latitudes, underlying winter storm tracks and co-located with complex mesoscale structures.

The Gulf Stream and eddies are both associated with strong positive vertical shear below their velocity maxima, which suggests that Doppler shifting should play an important role in setting the distribution of internal wave energy originating from the surface. Along-stream rays shown in Figure 2.8 do not reach critical layers but instead propagate off the page into the ocean interior. These rays quickly have their ω_i shifted higher as they propagate down through the positive shear, filling the internal wave continuum in the ocean interior with energy above the forcing frequency. The implications of Doppler shifting by the mesoscale should be appreciated not only for the immediate impact of momentum deposition in local critical layers, but for the up-frequency cascade of kinetic energy. Many studies have focused on the impact of wave-mesoscale interactions on the kinetic energy cascade, (Savage et al. 2025; Tedesco et al. 2023; Barkan et al. 2021). Mechanisms considered here could play an important role in that cascade, alongside the often implicated nonlinear wave-wave interactions.

2.5.3 Implications for the Zonal Momentum Budget

The wave-mean interaction mechanism studied here has long been known by atmospheric scientists as an important contributor to atmospheric zonal momentum budgets, (Andrews and McIntyre 1976; Bühler and McIntyre 1999). Internal wave momentum deposition at inertial levels is incorporated into weather predictions and climate models in the form of a parameterized wave-drag (Achatz et al. 2024; Kim et al. 2003; McFarlane 1987; Bühler 2014). The same is not yet true for ocean models. Recent ocean studies have modeled the wave-mean momentum flux driven by topographically generated internal tides, but this is the first study we are aware of to highlight the contribution of wind-driven near-inertial waves to mesoscale momentum budgets.

The magnitude of the wave-drag we compute is similar to the pseudomomentum divergences forced by internal tides. Shakespeare and Hogg (2019) computed the divergence of vertical flux of zonal pseudomomentum to be ±0.02 N/m^2, similar to the 0.0344 N/m^2 contribution to our wave-drag from the vertical flux of zonal momentum for initial ω_i = 1.2. Pinkel et al. (2012) estimated an Eliassen-Palm flux divergence of 0.1025 N/m2 from an internal tide with $\hat{u}$ = 0.50 m/s amplitude, similar to the possible F_{EP} divergence we report for sub-inertial waves of amplitude $\hat{u}$ = 0.20 to 0.25 m/s. The magnitude of the upper bound of near-inertial wave drag is comparable to other contributors to Gulf Stream momentum and drag. Gula et al. (2015) report a form drag generated as the Gulf Stream runs over the Charleston Bump with a magnitude of 0.3 N/m^2. Surface wind stress and turbulent bottom stress in the same area have magnitudes of approximately 0.05 N/m^2. de Marez et al. (2020) investigate the impact of lee waves generated by the same topographic feature and find that the waves exert a drag of 0.2 N/m^2 on the current, decreasing the local velocity by 20 cm/s. Similar to topographic features, near-inertial waves are spatially sporadic. Unlike topography they are also temporally sporadic, which further complicates the task of parameterizing their impact on the Gulf Stream momentum budget. Renault et al. (2023) emphasize the importance of including a parameterized drag at the ocean surface to prevent modeled Gulf Streams from becoming too sensitive to bottom drag, especially when considering energy pathways in eddy-rich simulations. The near-inertial wave drag introduced here acts below the surface, distributed across the upper 1000 m, so representing it may play an important role in accurately modeling Gulf Stream dynamics.

The importance of eddy-momentum fluxes for the Gulf Stream is well studied, and even diagnosed using a form of the Eliassen-Palm flux we use in this study (Uchida et al. 2022). Zonally averaged, the eddy-momentum flux magnitude of approximately 0.1 N/m^2 is found to be similar to that of the wind stress (Greatbatch et al. 2010). A zonal average of the near-inertial wave drag would depend on the spatial and temporal distribution of the wind forcing. This distribution may change as the mid-latitude storm track becomes more energetic under climate change, introducing the potential for a complex feedback mechanism. Given the increasingly recognized importance of the Gulf Stream and Kuroshio recirculation currents in climate modeling, quantification of near-inertial wave drag warrants further investigation, towards model parameterizations.

2.6 Conclusions

We have shown using an observational case study, and demonstrated with ray tracing, that against-stream propagating near-inertial waves are Doppler shifted to critical layers when they interact with the shear and strain structure of the Gulf Stream. Using an FCTD/ADCP transect of a near-inertial wave in the Gulf Stream, we showed ω_i decreasing at a rate consistent with Doppler shifting by vertical shear until it reaches locations where $\omega_i = \omega_{min}$ and ω_{min} contours are parallel to isopycnals. We show that c_{gz} goes to zero in these locations, consistent with critical layer behavior, and that they are co-located with elevated ϵ_χ and elevated Ri^{-1}. These combined factors point toward shear-driven dissipation in a critical layer. Total against-stream divergence of the observed near-inertial wave within its critical layer would lead to local velocity loss of 0.03 m/s.

Behavior of our observed near-inertial wave is consistent with that of simulated near-inertial rays. We use ray tracing to explore the mechanism of wave-drag associated with inertial critical layers in the Gulf Stream core. Similar to previous ray tracing studies, (Kunze 1985; Olbers 1981), we find that only near-inertial waves propagating against-stream encounter critical layers, leading to a preferential deposition of momentum against the current. Upper bounds on the magnitude of near-inertial wave drag lead to velocity reductions of up to 0.45 m/s for sub-inertial waves. It would be useful for future studies to better constrain the parameter space of ω_i, as we find near-inertial wave drag to be highly sensitive to this initial condition. Such future studies could work towards a parameterization of near-inertial wave drag on oceanic zonal jets similar to those implemented in the atmosphere for weather prediction and climate modeling. The impact of near-inertial wave drag on the transport of heat and other tracers by the Gulf Stream is potentially significant, and warrants further investigation.

Acknowledgements

The authors wish to thank the Captain and crew of the RV Neil Armstrong and the engineers of the Multiscale Dynamics Group (MOD) for their skill and hard work in obtaining these observations. The authors thank Dan Whitt, Leif Thomas, Colm Caulfield, Rick Salmon, Bill Young, Jennifer MacKinnon, Kerstin Bergentz, and Andrea Rodriguez-Marin Freudmann for useful discussions. This work was supported by the US Office of Naval Research under award N00014-25-1-2016.

Chapter 2, in part is currently being prepared for submission for publication of the material. Bellerjeau, Charlotte; Alford, Matthew H.; Voet, Gunnar; Couto, Nicole; Le Boyer, Arnaud. “Near-Inertial Wave Drag one the Gulf Stream”. The dissertation author was the primary investigator and author of this material.

Chapter 3 : Polymer Shear Probes for Durable Ocean Turbulence Sensing

3.1 Introduction

The dissipation of kinetic energy plays a key role in ocean mixing and kinetic energy budgets (Munk and Wunsch 1998; Waterhouse et al. 2014), which influence the overturning circulation and climate on regional and global scales (Melet 2022). Kinetic energy dissipation, ϵ, is driven by a variety of processes that transfer kinetic energy from internal waves, submesoscales, and other larger scale motions to the meter scales of 3D turbulence and eventually to the centimeter scales at which viscosity converts kinetic energy to heat and potential energy. This conversion of energy to smaller scales and eventual mixing and dissipation is sometimes referred to as the forward kinetic energy cascade. When we measure ϵ we are observing the last step in this process. Because it is driven by such a diverse array of processes, turbulence is spatially and temporally patchy (MacKinnon et al. 2017). Its patchiness and small scales make ocean turbulence difficult to observe, alongside all of the other difficulties of ocean observing such as high pressures and saltwater intrusion.

Despite the challenges, ocean turbulence observation is becoming increasingly important to the ocean science community. Le Boyer et al. (2023) suggest the introduction of turbulent diapycnal fluxes, which depend on ϵ, as an essential ocean variable. This distinction signals the importance of observing ϵ using standardized, robust, and accessible platforms. Thus far, ocean turbulence sensing has been available only to a handful of highly specialized labs who have the capacity to make their own microstructure instruments (Le Boyer et al. 2021; Moum and Nash

2009; Gregg 1999), or those that can afford to buy microstructure observing platforms off the shelf. In order to reach their full potential as an essential ocean variable, turbulent diapycnal fluxes should be observable from long term autonomous networks like ARGO or GO-SHIP (Roemmich et al. 2019). Integration in such programs requires that sensors be durable for handling and deployment by non-experts.

Historical and contemporary sensing of ϵ is achieved by shear probes using piezo-ceramic sensing elements which are exceedingly fragile, (Siddon 1971; Oakey 1977; Lueck et al. 2002). Here, we introduce a new design for a shear probe sensing element made of the flexible piezo-polymer polyvinylidene fluoride (PVDF). Piezo materials are distinguished by their ability to convert a mechanical deformation into an electrical response signal, and vice versa. They are commonly used as acoustic transponders and strain gauges, with shear probes being closer to the latter. Shear probes work by sensing the pressure perturbations generated by changes in the surrounding fluid velocity. Their design will be discussed in detail in Section 3.2. By replacing the ceramic, lead zirconate titanate (PZT), sensing element with a polymer we have made a shear probe that is more resilient to the shock loading which is sometimes encountered during handling and deployment at sea. Traditional probes can be broken by tapping gently against a surface or impacts with fish or inanimate objects during profiling. The sensitivity of the PVDF probes is lower than conventional PZT probes, but is high enough to sense turbulence above the noise floor of the instrument, as seen in an ocean test off the coast of La Jolla in San Diego. We believe that future investigation into the efficacy of piezo-polymer shear probes is warranted following this proof-of-concept demonstration. In Section 3.2 we will detail the design parameter space and manufacturing process; in Section 3.3 we will show the results of calibration, pool and ocean tests; and in Section 3.4 we will conclude with future recommendations and impacts.

3.2: Design and Manufacturing

3.2.1: Historical Shear Probe Design

Due to its random nature, turbulent flow is very difficult to describe in a useful way with the same equations of motion we use to describe more predictable fluid flows. Subsequently, the fields of physics and engineering have developed a statistical approach to the description of turbulent fluid flows (Kundu and Cohen 2010). One of the assumptions of this statistical description is that the amount of energy supplied to the scales of motion where 3D turbulence occurs is balanced by the amount of energy being removed by viscous dissipation. The power of this assumption is that by estimating the energy level of the velocity or shear spectrum of 3D motion we can estimate the rate of kinetic energy dissipation:

$$\epsilon = \frac{15}{2} \nu \frac{\overline{\partial u^2}}{\partial z} \qquad 3.1$$

where $\nu = 1 \times 10^{-6}$ m s^{-1} is the viscosity of water and $\partial u / \partial z$ is the change in horizontal velocity with depth, or vertical shear. Shear probes measure vertical shear and then we fit the spectrum to a universal curve referred to as the Nasmyth spectrum to estimate ϵ. An example of this curve fitting will be shown in Section 3.3.2.

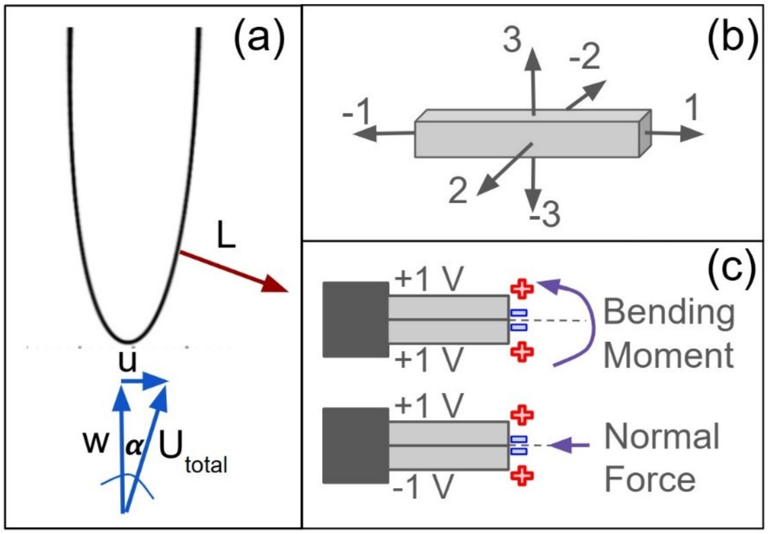

Figure 3.1: [a] Force diagram depicting low angle fluid flow over a falling shear probe. [b] Axes for polarization of a piezo-material. A 3-1 mode piezo-material would produce a voltage potential across the 3 axis when stretched in the 1 axis. [c] A cartoon bimorph design. It is sensitive to bending but insensitive to normal force.

Small-scale shear is directly observed by relating the electrical signal from the sensing element to the pressure exerted on the probe by the fluid flow. The first airfoil probe was used to measure turbulence in a wind tunnel rather than in the ocean (Siddon 1971). The core concepts remains the same for our shear probes today. They leverage the linear relationship between the lift force exerted on an airfoil and the angle of attack of the oncoming fluid, depicted in the force diagram in Figure 3.1a.

The lift force can be expressed as:

$$L = qA\frac{\partial C_L}{\partial \alpha}\frac{u}{U_{total}} \qquad 3.2$$

where A is the effective probe area, $dC_L/d\alpha$ is the lift slope, u is the magnitude of the horizontal component of velocity, and U_{total} is the magnitude of the total velocity. $q = 1/2\ \rho w^2$ is the dynamic pressure, with fluid density ρ and vertical velocity w. The vertical velocity is approximately equal to the fall rate of the vehicle. Assuming small angles of attack, ($\alpha \leq 5°$), and spatial scales of turbulence that are much greater than the foil diameter, ($d_{max} = \lambda_{min}/4$), Equation 2 can be simplified to $L = q(u/w)$. After calibration, the electrical signal ($E0$) received from the pressure sensor is linearly related to the angle of attack:

$$E_0 = S_v q \frac{u}{w} \tag{3.3}$$

where S_v is a sensitivity constant. Osborn (1974) modified the airfoil probe design to measure turbulence in the ocean. Many of the considerations remain the same across both designs. The sensor must 1) have a frequency response compatible with the dominant spectral content of the turbulence, 2) occupy a volume much smaller than the characteristic wavelength of the turbulence, 3) offer sufficient sensitivity for a good signal-to-noise ratio, and 4) be insensitive to noise from vibration and temperature fluctuation.

Gregg (1999) points out that the range of turbulence that can be measured by a shear probe is limited by the size of the probe and the noise floor of the instrument carrying it. As turbulence becomes more energetic it is characterized by smaller scales of motion, so the ability of the probe to resolve high values of ϵ is limited by its diameter. The ability to measure low values of ϵ depends on the instrument being able to register small velocity signals above its noise floor, which depends on S_v.

Expressing Equation 3.3 in terms of the time signal of velocity change, $\partial u/\partial t = w(\partial u/\partial z)$ and using Equation 3.1 we can write an expression for the voltage output in terms of ϵ.

$$E_0 = S_v \left(\frac{w^2}{2g}\right) \sqrt{\frac{2}{15\nu}\epsilon} \tag{3.4}$$

The voltage signal expected from any given shear probe can now be computed for a range of ϵ if its sensitivity is known. In Section 2.2 we will predict the sensitivity of a PVDF shear probe using a first principles model, and in Section 3.1 we will report the sensitivities we found in MOD's specially designed calibration tank.

The sensor within a shear probe is made from a piezo material. Piezo-materials produce an electric charge in response to mechanical deformation, and vice versa. The piezo-material is polarized to maximize response across a specific axis (Figure 3.1b). For example, the piezo sensors in our shear probes are 3-1 polarized, meaning a deformation in the 1 axis leads to a voltage potential across the 3 axis. Polarization amplifies the response across the desired axis to the desired force, but doesn't eliminate the response of other axes entirely. To cancel the signal from forces normal to the probe tip, or changes in the oncoming velocity, the sensors are constructed in a bimorph configuration (Figure 1c). The bimorph design makes the probe insensitive to the normal velocity component and doubles the signal of the horizontal velocity component normal to its active axis. Any change in the oncoming velocity will cause a negative voltage across one side of the probe and a positive charge across the opposing side, resulting in a net zero voltage. A change in the horizontal velocity, however, will result in the stretching of one half and the compression of the other, yielding a doubled net voltage.

The shear probe design has remained largely unchanged since Osborn (1974) adapted it for ocean turbulence. It has been reproduced in slightly different dimensions by a handful of labs and companies (Gregg 1999; Moum and Nash 2009; Le Boyer et al. 2021) and for a multitude of different vehicles (Lueck et al. 2002), but the airfoil design with a piezo-ceramic bimorph sensor has never changed. The reason we are proposing an alternative now is not due to any failure of the traditional shear probe to measure turbulence. Rather, we seek to expand its usefulness outside the hands of the highly specialized experts who currently manufacture and deploy it. A polymer, rather than a ceramic, sensing element will be more conducive to deployments by non-experts.

3.2.2: Modelled Design Parameter Space

Before detailing the design of our PVDF shear probe, we explore the design parameter space using a first-principles model. We start by predicting the lift force on the probe tip using potential flow modeling, then compute the internal stresses using a beam-bending analysis, and finally convert these internal stresses to a voltage potential using the sensitivity information available for PVDF (MeasurementSpecialtiesInc 1999).

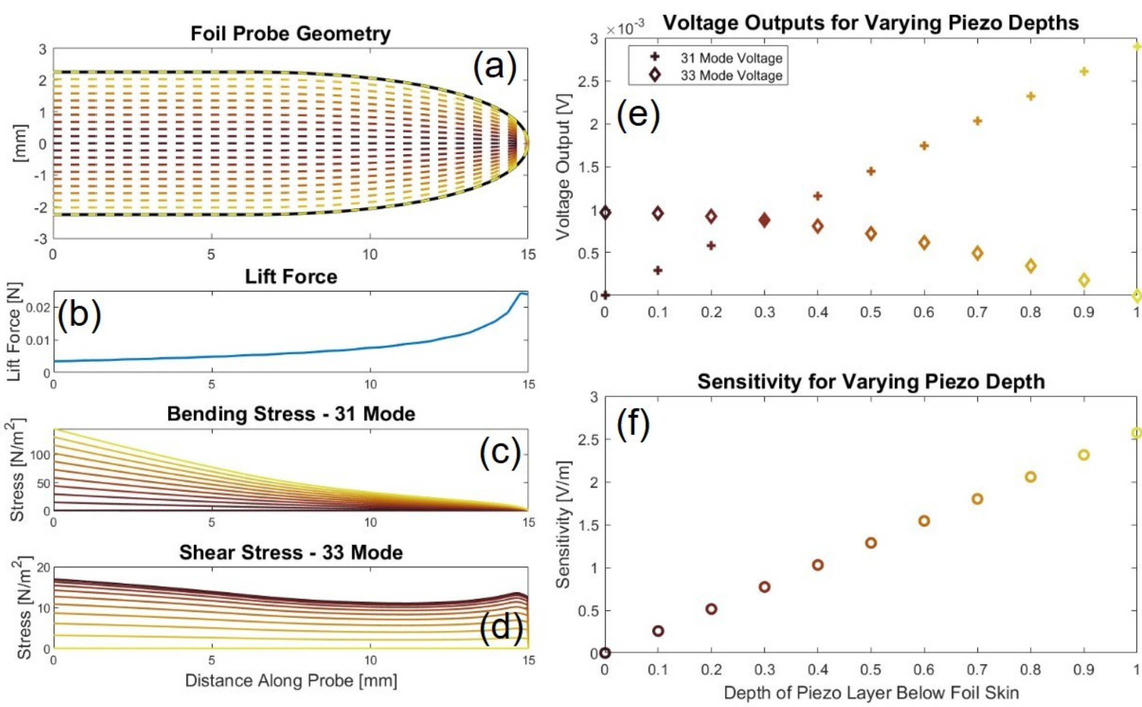

Figure 3.2: [a] Shear probe geometry with 10 potential depths at which to embed a PVDF film shown in color. [b] Lift force exerted on the outside of the probe by 0.65m/s oncoming flow at 5° angle of attack. [c] Bending stress and [d] Shear stress exerted at each potential PVDF film depth. [e] Voltage output for each potential film depth and polarization, [f] Sensitivity of probe for varying film depths, after selecting the 3-1 mode and running a simulated calibration.

First, we approximate the probe as a thin symmetric airfoil (NACA 0015), with a range of possible depths at which to place a thin film of PVDF, (Figure 2a). Next, we use a potential flow analysis to predict the force exerted on the probe tip by oncoming seawater at 0.65m/s, the average fall rate of the MOD lab's epsilometer (Le Boyer et al. 2021). Flow around a thin airfoil at low angle of attack can be modeled by a vortex sheet within a uniform flow (Anderson 2011). The pressure contours predicted by this simulation show high pressure on the side closest to the oncoming flow and low pressure on the opposite side, as expected. By integrating the predicted pressure distribution over the area of the probe tip, assuming axial symmetry, we estimate the force exerted on the probe, (Figure 3.2b).

The internal stresses are computed as a function of depth and lengthwise position, using the force distribution computed above and approximating the probe tip as a cantilevered beam. The internal stress in the cross-probe direction, shear stress, would be best captured in the 3-1 mode of a piezo-film, while stress in the along-probe direction, bending stress, would be captured by the 3-3 mode. The shear force and bending moment are used to compute the shear stress and bending stress for a range of piezo depth options, (Figure 3.2c and 3.2d).

The stresses experienced by the PVDF layer and the reported piezoelectric constant are used to compute the voltage potential across the simulated bimorph beam. The units of the piezoelectric constant are $\frac{\mathrm{V}}{\mathrm{m}} / \frac{N}{m}$, signifying voltage per meter of piezo thickness divided by pressure applied to relevant area. The relevant area depends upon which mode is being considered. For the 3-3 mode, the area is the larger flat face of the PVDF film. For the 3-1 mode, the area across which the stress is being distributed is the cross section of the PVDF film, (Figure 3.1b).

Predicted voltage output is shown to be greatest for a PVDF film closer to the skin of the probe, and activated by the 3-1 mode, (Figure 3.2e). Next we run a simulated calibration to assess the potential sensitivity of different geometries. Adopting the 3-1 mode, we run each simulated

geometry through a range of angles of attack to compute sensitivity in V/m (Figure 3.2f). This process is the modeled equivalent of the calibration tank used by the MOD lab for our home built shear probes, which will be described in Section 3.5. For reference, the typical sensitivity for one of MOD's shear probes is 35-45 V/m Le Boyer et al. (2021). The sensitivity predicted by our first principles model for a 2 layer PVDF probe is 2.5 V/m, 16x lower than the sensitivity for a traditional probe. It should be noted that this model was run assuming only one layer of PVDF on each side of the bimorph beam. Sensitivity in our final design is increased by adding layers of PVDF to each side, wired in parallel.

Before summarizing the takeaways of our design space model, we remind the reader of the assumptions involved. We used potential flow theory to compute the forcing, which assumes inviscid, incompressible, irrotational flow, and we assumed a small angle of attack and attached flow. The beam bending approximation assumes small angle deformation. With these assumptions in mind, some lessons can be taken away from the model. Internal stresses are maximized at the fixed end of the probe. The 3-1 mode experiences an order of magnitude greater activation stress in our configuration, so it makes sense to select a 3-1 polarized PVDF film. Sensitivity is maximized by positioning the PVDF layers as far as possible away from the center axis of the probe. These lessons were used to inform the design described in the following section.

3.2.3: Manufacturing Method

The design presented here features 8 layers of 28μm PVDF, with 4 layers of PVDF on each side of a 1 mm thick silicone divider forming a bimorph beam. The manufacturing process detailed in this section was designed for iterative prototyping.

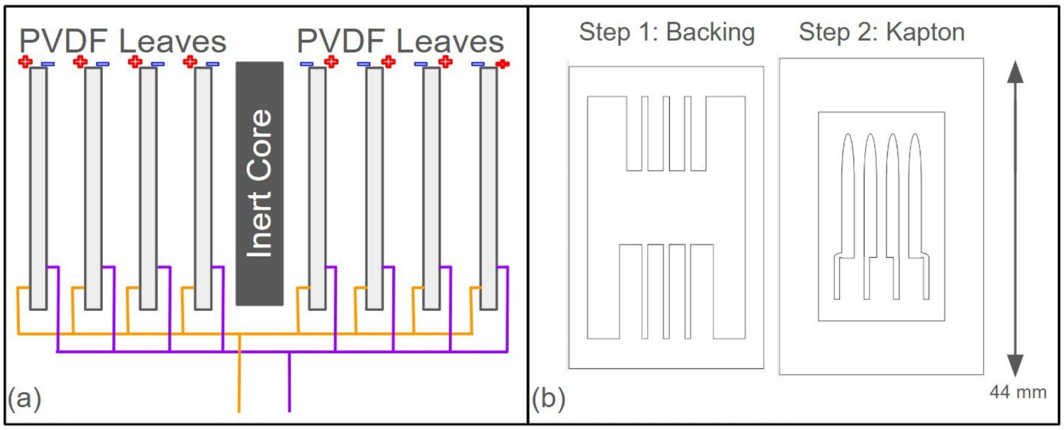

Figure 3.3: [a] A wiring diagram, showing the two sides of the bimorph beam wired in parallel to maximize capacitance [b] The two steps of the laser cutting process needed to make a kapton stencil.

We start with a 200 mm by 280 mm sheet of PVDF manufactured by PolyK, with silver electrodes screen printed on either side across the entire sheet. Cutting directly through the sheet would pinch the silver electrodes together causing a short, so the first step is to etch around the desired shape with acetone, removing the surrounding silver. To define the shape of the PVDF leaves we use a two step laser cutting process to make a kapton tape stencil, (Figure 3.3b). The first step cuts a platform into a tape backing material that will hold each kapton leaf in a fixed position while revealing the sticky side in the middle. Then 2 layers of 0.0015" kapton tape are applied, being careful not to move the backing strip in between laser cutting steps. The second step cuts the shape of the PVDF leaves without cutting the backing behind it. Very low power and precise focus are necessary for the laser cutter to fully cut through the tape, but not the backing. Narrow strips on the bottom of the set of four kapton leaves fan out so that they can all be accessed on a flat plane for soldering in parallel, maximizing capacitance (Figure 3.3a). The signal is measured through a charge-amp circuit, so higher capacitance yields the strongest possible signal.

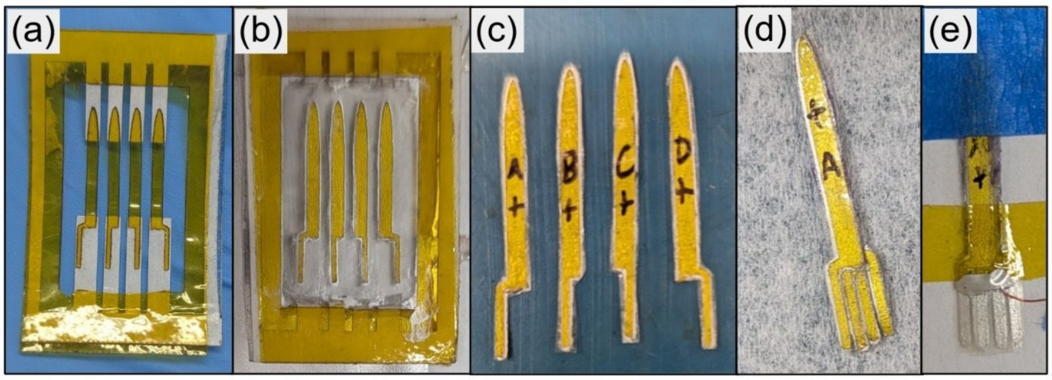

Figure 3.4: [a] A kapton stencil with the center sections peeled off the front and back, ready to be stuck down onto the PVDF sheet [b] The PVDF sheet with the stencil still attached after acetone etching [c] A set of 4 PVDF leaves after being cut out with scissors [d] A set of 4 PVDF leaves glued together [e] A set of 4 PVDF leaves after soldering the magnet wire to one side.

Once the stencil is cut the middle section of the kapton layer is peeled off to reveal the PVDF leaves, and the middle section of the backing is peeled to reveal the sticky side of the tape (Figure 3.4a). One stencil is adhered to either side of the pre-electroded PVDF sheet, making sure to match up the corners so they align precisely on either side. Then acetone is used to remove the unwanted silver surrounding the PVDF leaves with a Q-tip, being careful not to accidentally peel up the kapton tape (Figure 3.4). One layer of kapton tape is removed from each side after etching, leaving only a single 0.0015” kapton protector on each side. The PVDF leaves are labeled on their positive side. This labeling step is important to achieve the bimorph configuration, as all of the positive faces need to be oriented outward. After labeling, the leaves are cut out from the larger PVDF sheet with scissors (Figure 3.4c). The leaves are glued together with Loctite 422 adhesive after lightly sanding each side and priming with Loctite SF 770 primer

(Figure 3.4d). Once the glue dries the kapton tape on the soldering pad is carefully peeled up to reveal the silver on all four leaves and a 36 Ga magnet wire is soldered across them (Figure 3.4e). Silver epoxy is used to prevent damaging the PVDF with traditional hot solder. The opposing side is covered with a piece of kapton tape to prevent the silver epoxy from bleeding through and shorting the probe. The first side cures for at least two hours before flipping and soldering the other side.

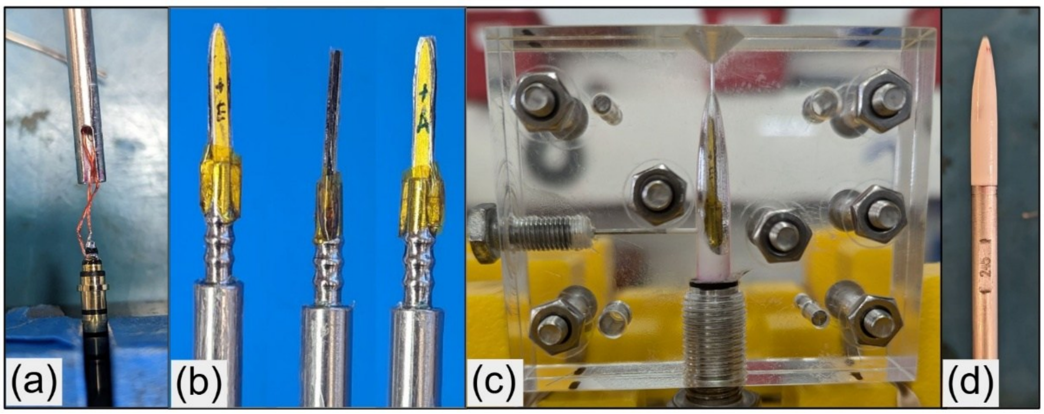

Figure 3.5: [a] Two pairs of 36 Ga magnet wires soldered to the TRRS jack before insertion into the sting [b] Three views of the sensing element in the sting just before injecting epoxy [c] Silicone being injected in the mold during the final step of manufacturing [d] A finished PVDF shear probe.

Two halves, each with a wire soldered to both sides are glued back to back with a 1 mm silicone spacer in between, using the same glue and primer as before. The negative wire of one side is twisted together with the positive wire from the other side, completing the wiring diagram from Figure 3.3a. The two twisted pairs are then threaded through a machined steel tube, the same sting used by the MOD lab for our traditional shear probes with the addition of a notch on one end to make room for the PVDF soldering pad. The wires are soldered to a TRRS connector (Figure 3.5a), and the 8 layer PVDF sandwich is temporarily secured in its notch with a thin strip of kapton tape (Figure 3.5b). Epoxy is injected into the steel tube using a specialized jig and cured under pressure for 24 hours. Silicone is then injected into the same mold used for our traditional probes (Figure 3.5c) and cured under pressure for at least 24 hours. Finally, we have a completed PVDF shear probe (Figure 3.5d).

As mentioned earlier, this manufacturing method was designed for iterative prototyping. The ability to quickly make a new stencil shape allowed us to try several different prototypes before landing on the 8 layer probe presented here. For a finalized design, we would recommend screen printing the electrode pattern directly onto the PVDF, which would greatly simplify the process.

3.3: Validation

3.3.1: Calibration

A batch of 5 8-layer PVDF probes are analyzed in this study, starting with determination of their sensitivity in MOD's specially designed calibration tank. The tank shoots a laminar jet of water, and the probe angle of attack is modulated through ±5° while measuring the voltage output (Figure 3.6a). The voltage response of 5 8-layer PVDF probes is plotted alongside that of a single traditional probe (Figure 3.6b). The mean peak-to-peak voltage of the PVDF probes is 0.2105 ± 0.0337 V, while the traditional probe had a peak-to-peak voltage of 1.219 V. The frequency response of all 5 probes can be seen in Figure 3.6c, which shows a similar primary peak frequency across all calibrations, representing the oscillation rate of the calibrator arm. The mean sensitivity of the PVDF probes was determined to be 6.79 ± 1.02 V/m, computed as describe in Section 3.2.1 (Figure 3.6d). This is in agreement with the prediction of 8 V/m for an 8 layer probe from the first-principles model. The sensitivity of the traditional probe was 38.35 V/m, within the standard range for MOD shear probes of 35-45 V/m (Le Boyer et al. 2021).

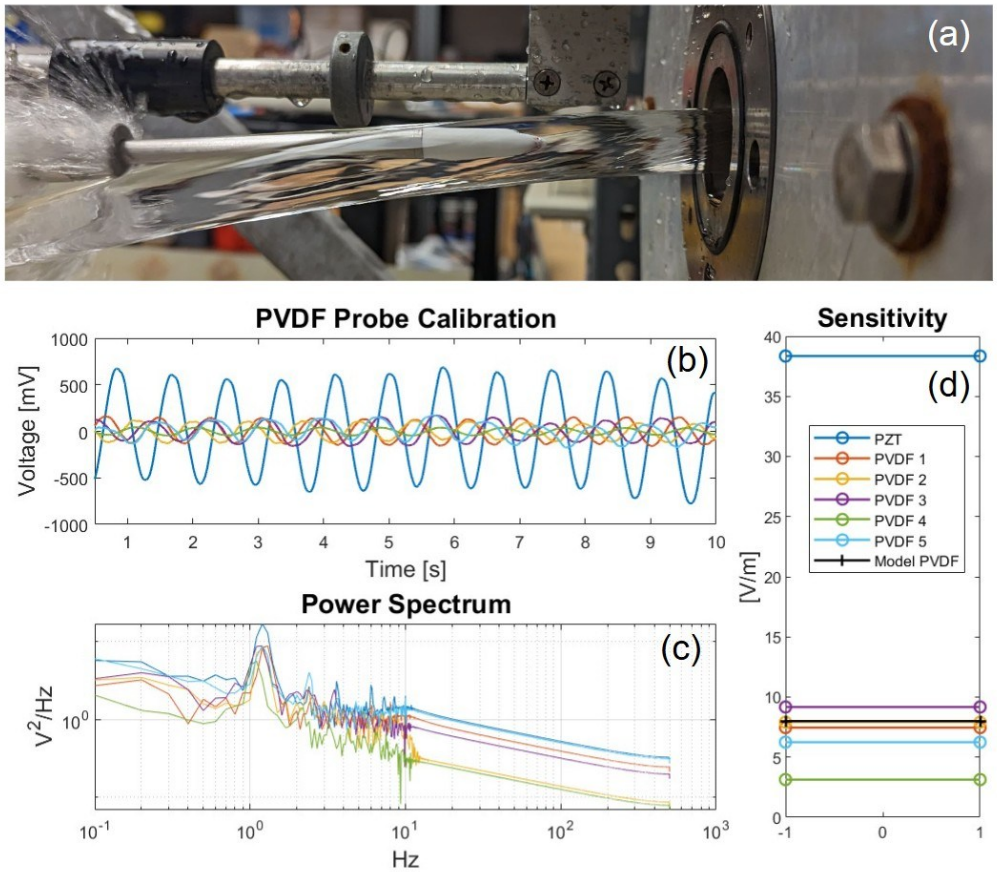

Figure 3.6: [a] Image of a probe positioned in the laminar flow coming out of the calibration tank [b] Voltage output during probe calibration [c] Power spectrum of probe output during calibration [d] Sensitivity of probes compared to model prediction.

Given the sensitivities of our batch of probes, we can estimate their voltage outputs for a range of ϵ from Equation 4. $\epsilon = 10^{-10}$ is the lowest level of turbulence that can be measured above the noise floor of the MOD lab's microstructure profiler Le Boyer et al. (2021). For $\epsilon = 10^{-10}$ the PVDF probe would produce a 0.54 mV signal, compared to a 2.8 mV signal from the traditional probe. Gregg (1999) reports that the highest value of ϵ that can be resolved using traditional sized shear probes is $\epsilon = 10^{-5}$. The PVDF probes would produce a signal of 0.17 V for this value of ϵ, compared to 0.87 V for a traditional probe.

3.3.2: Testing

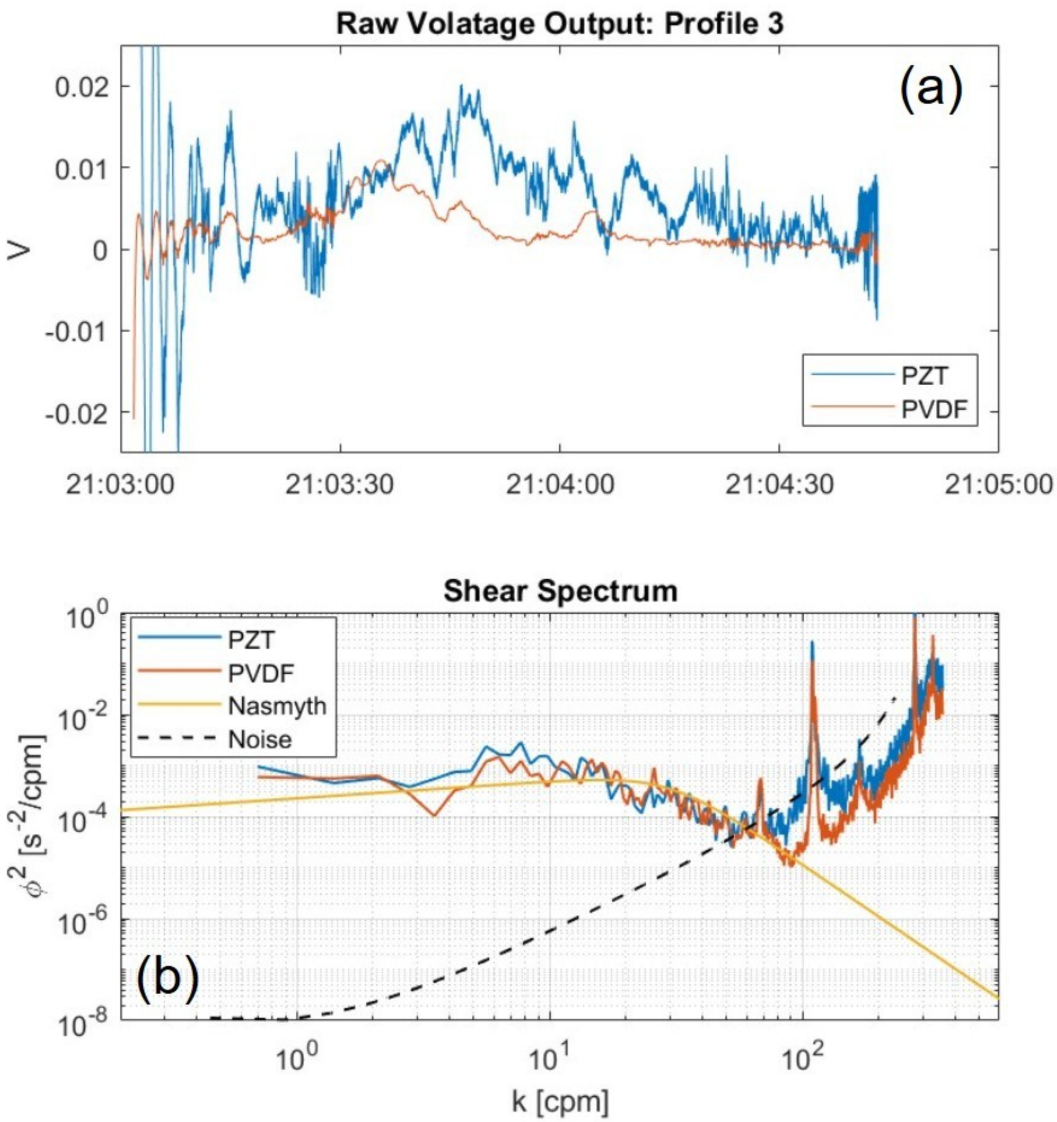

Figure 3.7: Wavenumber spectrum of shear measured offshore of the SIO pier by a traditional PZT probe (blue) alongside a PVDF probe (red). The theoretical Nasmyth spectrum (yellow) that best fits these spectra corresponds to $\epsilon = 1.5 \times 10^{-7}$ W/kg. The instrument noise floor (dashed black) dominates at high wavenumber.

PVDF probe number 5 was tested alongside a traditional PZT probe by profiling the MOD lab's epsilometer off of a small boat using a high speed fishing reel. 7 profiles were performed down to 45 m of depth. Raw voltage output from both probes is shown in Figure 3.7a. Upon visual inspection, the low frequency response of the probes seems to be very different.

However, ϵ is computed by making a wavenumber spectrum of shear from 2 second windows of data, so the low frequency response is not necessarily relevant. The shear spectra in Figure 3.7b is an average of 5 adjacent spectra, covering 8 m to 10 m depth in profile 3. The response of the probes at high wavenumber, which is the part of the signal used to compute ϵ is quite similar in this example. The theoretical Nasmyth spectrum that best fits these spectra corresponds to an observed $\epsilon = 1.5^{-7}$. Instrument noise begins to dominate the signal of both probes around 58 cpm.

Using a curve fitting procedure like the one that resulted in Figure 3.7b, ϵ is computed for all 7 profiles (Figure 3.8). Both probes observe comparable profiles of ϵ with the exception of the first profile, which shows the greatest difference between the two. The voltage signal is scaled by probe sensitivity before computing ϵ, so the slight negative offset of most of the observations from the PVDF probe may be due to an inaccurate calibration of one of the two probes.

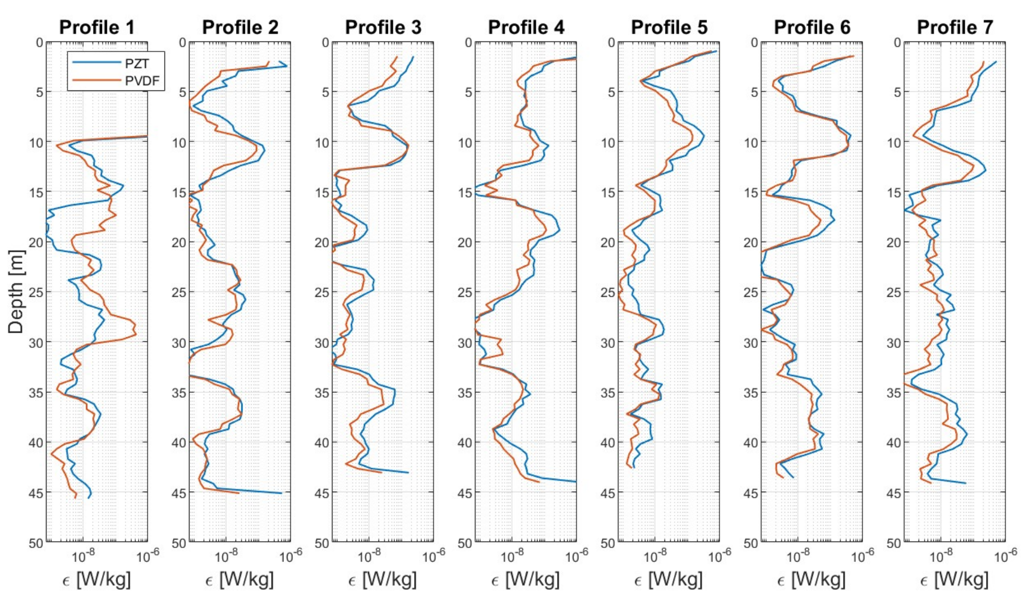

Figure 3.8: 7 Profiles of ϵ taken half a mile west of the SIO pier.

3.3.4: Durability

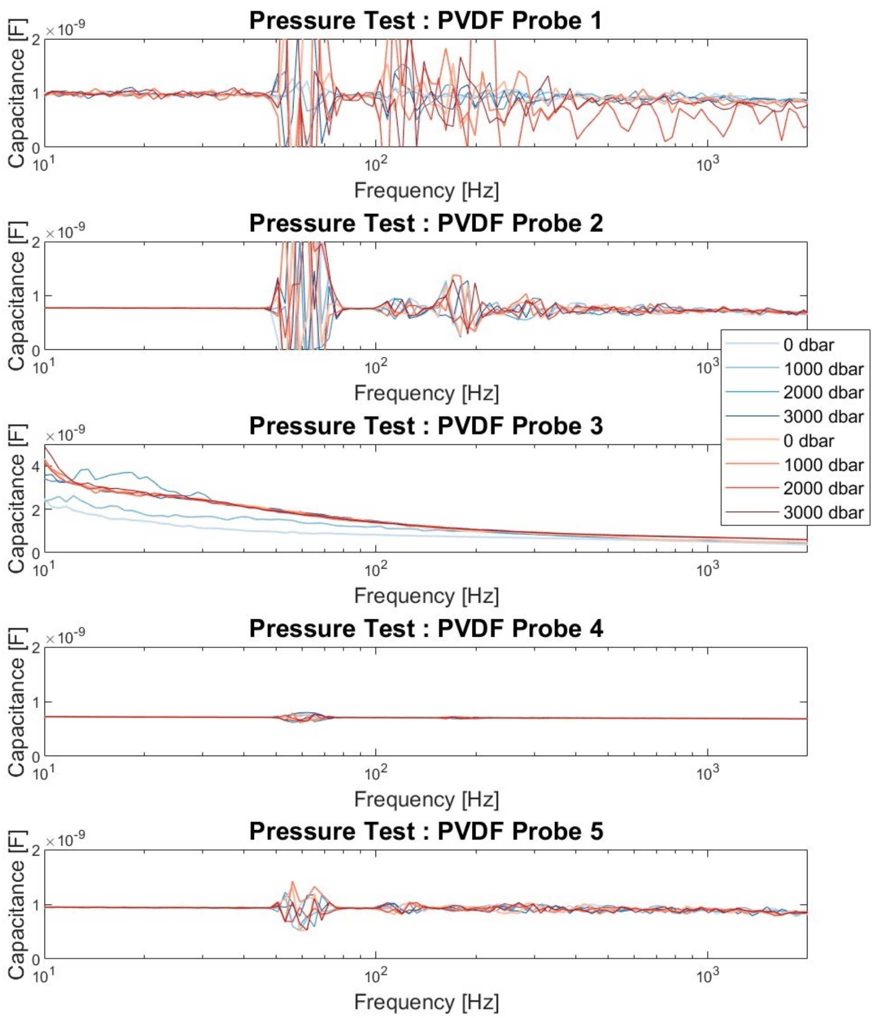

Figure 3.9: Capacitance of the 5 PVDF probes during two cycles from 0 to 3000 dbar, measured from 10 Hz to 20 kHz. The first cycle is plotted in progressively darker and thinner blue lines and the second cycle in red.

Probe capacitance was measured from 10 Hz to 20 kHz during exposure to 1000, 2000, and 3000 dbar of pressure in a bench top pressure pot (Figure 3.9). Each probe was cycled up to 3000 dbar twice, based on the erratic behavior of the PVDF probe on it’s first ocean profile compared to subsequent profiles. Probe behavior at frequencies less than 25 Hz are relevant to ϵ

observations, as they correspond to the maximum frequency at which a profiler falling at 0.5 m/s might encounter 50 cpm turbulence. After 50 cpm the noise of the instrument dominates. A flat capacitance between 750 and 1000 pF indicates a functioning probe, with higher capacitance indicating more sensitivity. All of the probes picked up on a noise signal at 60 Hz corresponding to the frequency of the fluorescent lights in our lab. Probe 1 had a noisy signal at low frequency after 2000 dbar on the first cycle, which would lead to an unstable calibration constant and an unreliable probe. Probe 2 experienced noise at high frequency, but was reliable at the frequencies we care about for observing ϵ. Probe 3 behaved unreliable at low frequency, with a capacitance that changed significantly during the first pressure cycle and decreased with increasing frequency across all tests. If this behavior was displayed before calibration the probe would not have been included in the final batch, so it must have been damaged after calibration. Probe 4 behaved well at all frequencies and pressures. The final probe, which was the one that had been used in the ocean tests prior to this pressure test, behaved well at the frequencies of interest.

We did a final durability test by dropping all 5 of the PVDF probes tip down from bench height (38 cm), measuring their capacitance before and after (Figure 3.10). This test was chosen as a worst case scenario for the kind of damage that could be sustained during fieldwork. More often, probes might be lightly tapped on a bench or brushed up against during installation, both of which would likely be survived by a probe that survived the drop test. It is known from experience, but not verified in this study due to manufacturing costs, that PZT probes would not survive being dropped from bench height. Probes 1 ad 5 survived the drop test with their capacitance unchanged. Probe 2 experienced a drop in capacitance and probe 4 experienced an increase in capacitance. Both of these would still give an estimate of ϵ following this damage, but their calibration constant would be changed causing an offset in the magnitude of ϵ. Probe 3 experienced a drop in capacitance and the addition of noise at low frequencies, which would cause ϵ estimates to be unreliable. The failure mode of the probes that changed following the drop tests is most likely a change in the contact of the solder joints, causing the measurement of the signal from one or more of the PVDF leaves to change. This failure mode could be addressed by designing a more robust receiving end of the sting into which the PVDF is potted with epoxy. The more stable the solder joint is within the potted epoxy the less likely it is to be damaged. Additionally, 3 of the probes sustained damage to the silicone and would not have been water tight after dropping. This result leads me to conclude that the PVDF sensor is more durable than the silicone in which it is potted, a significant improvement in durability over traditional probes.

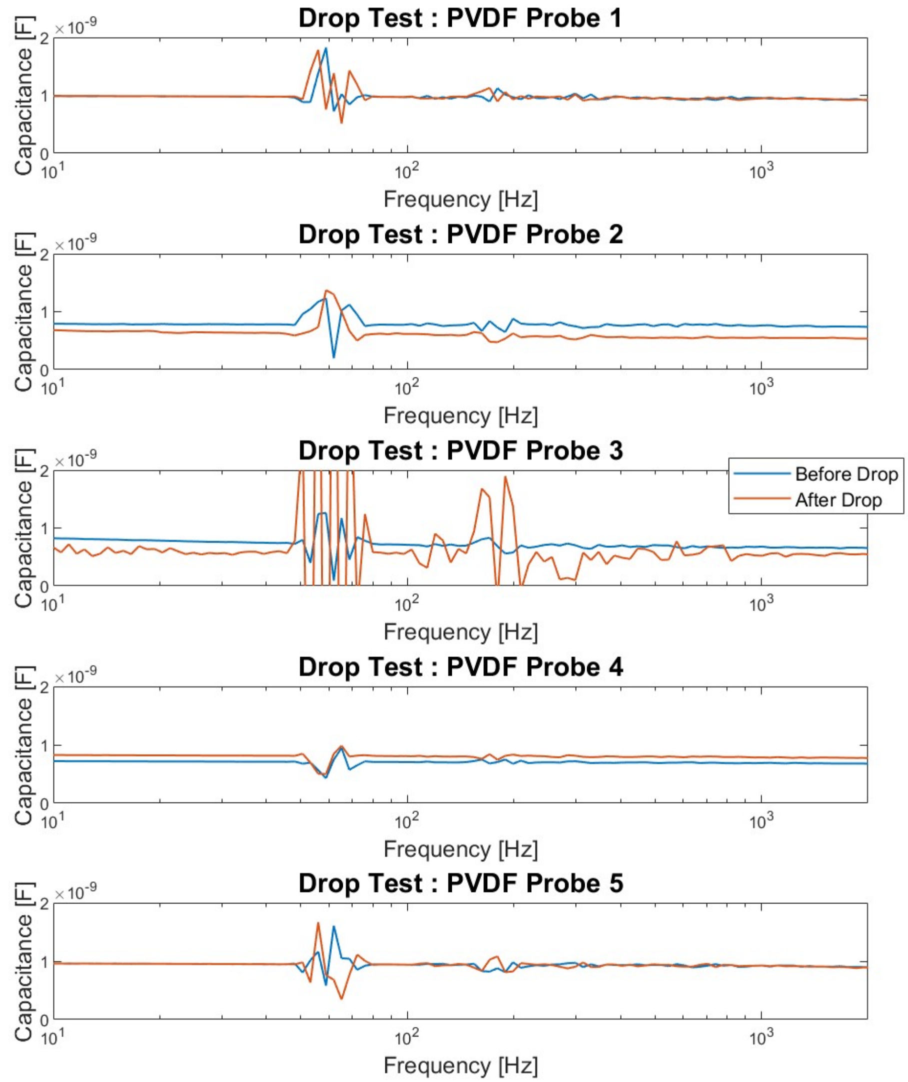

Figure 3.10: Capacitance of the 5 PVDF probes before (blue) and after (red) being dropped tip down from 38 cm, measured from 10 Hz to 20 kHz.

3.4: Discussion and Conclusions

This study has demonstrated the viability of piezo-polymers for ocean turbulence measurements. PVDF shear probes measured here were 16% as sensitive as a traditional shear probe, which was enough to reliably measure ϵ in the range encountered in a nearshore ocean test. Three out of 5 probes behaved well in water under up to 3000 dbar of pressure. Two out of 5 survived a 38cm tip down fall with no observable damage to the sensor, while an additional two experienced some damage and one was broken irreparably. Future development could be focused on durability to long-term saltwater exposure, which also poses a problem for traditional probes. Other durable options for measuring ϵ are on the horizon as well, and should be considered as an alternative for some applications (Wang et al. 2022; Northcott et al. 2026).

A traditional shear probe takes approximately 5 hours to assemble, spread out over 3 days to account for curing time for the epoxy and silicone. The manufacturing process in this study takes significantly longer, around 7 hours. However, this process was designed for prototyping. In the future the electrodes could be printed directly on the PVDF rather than acetone etching with a stencil, and the time for assembly would be comparable to a traditional probe. A traditional probe costs approximately $200 USD to produce, which includes $150 to have the steel sting machined, $10 for the PZT sensor, and the rest for epoxy, silicone, and wires. The only cost difference in our design is the sensing element, which is approximately $4.50 for a PVDF probe.

In theory the PVDF design could be made more sensitive by adding additional layers. In practice there is no more room within the dimensions of the current probe for additional layers. Our prototypes are just below the limit of exceeding the silicone diameter at the narrow end of the probe. To add sensitivity for resolution of low turbulence environments or decrease diameter for resolution of high turbulence flow, we would recommend that future studies explore other piezo-polymers. A range of other piezo-polymers exist with higher piezoelectric constants that could be used to design more sensitive shear probes with different dimensions. Several studies have demonstrated composite materials that combine flexible piezo-polymers with more sensitive piezo-materials like PZT (McCall et al. 2014; Cui et al. 2019; Ganeshkumar et al. 2017; Babu and de With 2014). Piezo-composites have been shown to yield a higher voltage response without sacrificing material durability. Flexible piezo-materials are already in use in ocean technology including bio inspired lateral-line velocity sensing, wave energy harvesting, and hydrophones, (Shizhe and Yijin 2022; Jbaily and Yeung 2015; Viet et al. 2017; Bowen et al. 2004). We chose to use off the shelf sheets of PVDF for this study because it allowed us to fabricate shear probes without a fume hood, spin coater, and other facilities that are often available in materials science labs but rarely in oceanographic labs. Going forward, deeper collaborations between oceanography and materials science could yield greater advancements in sensor development.

Based on the results of our pressure cycling and durability testing, future work should be dedicated to characterizing the failure modes and reliability over long time scales of polymer shear probes. The design of shear probes has remained the same for over 50 years, and has been tested in a wide variety of ocean environments on many platforms (Lueck et al. 2002). There is room for improvement by leveraging piezo-polymer materials that have been around for a similar length of time. The piezo-electric properties of PVDF were discovered in 1969, one year before the invention of the shear probe (Mishra et al. 2019; Siddon 1971). The parallel development of these two technologies highlights the need for greater collaboration across engineering disciplines. We have shown that even with limited access to materials synthesis, prefabricated piezo-polymers offer the opportunity for more durable ocean turbulence sensing. Future development will increase access to turbulence observations for large scale programs like ARGO and GO-SHIP that rely on non-specialist deployment.

Acknowledgements

We would like to acknowledge the talented and kind team of engineers in the MOD Lab, without whom this work would have been impossible. The Sandbox Makerspace at Scripps Institution of Oceanography provided laser cutter access and a welcoming and helpful environment. We would specifically like to thank Helen Dufel for excellent boat piloting, Zachary Taebel for assistance in durability testing, and Isabella Franco and Sara Goheen for machine shop wisdom and patience.

Chapter 3, in part is currently being prepared for submission for publication of the material. Bellerjeau, Charlotte; Le Boyer, Arnaud; Alford, Matthew H.; Lastuka, Sean; McConnell Becca. "Polymer Shear Probes for Durable Ocean Turbulence Sensing". The dissertation author was the primary investigator and author of this material.

Chapter 4 : Basic or Applied: Complicity and Tuning the Proximity of Research to its Impacts

A Student's Introduction to a Shifting Boundary

I once heard a professor say that they, "Never assign students to projects behind the veil". I assume that the "veil" they were referring to was one of security clearance, but I think it's an apt metaphor for the military-university complex at large. As a PhD student in Applied Ocean Sciences I've been exposed to the shifting definitions of the words basic and applied in many different settings. My time at Scripps Institution of Oceanography (SIO) has been punctuated by moments of conflict and resistance. The University of California San Diego, of which SIO is a part, has a rich history of protests in which the concept of complicity took center stage (Lim 2025; UCSD Libraries, n.d.). These moments have inspired myself and many other students to reflect on our own roles in academic research. Some graduate students who, like myself, are funded on Department of Defense (DoD) projects believe that they are taking money away from the military to do their research, which otherwise could have been put to a more violent use. The intention of this work is to invite those who hold these views to reflect and join in conversation, not to pass judgement. I've often wondered what interest the Office of Naval Research (ONR) could possibly have in my research, but we can see in their mission statement that they don't fund anything that doesn't benefit their objectives (Office of Naval Research, n.d.). The relationship between the military and academia in the United States seemed to be obscured from my perspective as a student.

The Merriam Webster dictionary defines complicity as an “association or participation in or as if in a wrongful act” (Merriam-Webster 2026). Not only does one have to be a participant in an activity to be complicit in it, but that action has to be perceived as wrongful. The wrongfulness of the U.S. military’s actions is beyond the scope of this study. We will instead speak to the association or participation of science in furthering the military agenda. Science and technology studies (STS) scholars Gregory Hollin and Ros Williams warn that in some formats, “recognition of the inevitability of complicity leads to guilt and passivity rather than action” (Hollin and Williams 2021). Their study describes complicity as a complex entanglement, distinct from guilt in that it is not necessarily a reflection towards past actions, but an ongoing relationship that is enmeshed with responsibility. Conversations around complicity in academia often hinge upon the distinction between basic and applied research. Language and our self-definitions as scientists play an essential role in the fabric of the veil.

A growing number of scientists argue that critically evaluating the histories of their fields will lead to contemporary research that is less likely to further colonial and racist structures (Scarlett 2022; Prescod-Weinstein 2017; Nyblade and McDonald 2021). Tamara Pico and the other creators of GeoContext, a resource for teaching the colonial history of earth sciences, describe the importance of origin stories in the way students do or don’t see themselves in science (Pico 2023; Cartier 2021). Much of the historical and contemporary rhetoric around basic and applied research is founded in the myth of neutrality; that science is objective, unbiased, and apolitical (O'Brien 1993; van Eck, Messling, and Hayhoe 2024). In the tradition of feminist sciences, many researchers have forged an alternative path that honors their positionality within science (TallBear 2014; Liboiron 2021; Giordano 2025). In this work I examine how language can be used to obfuscate our positionality as scientists, how the stories we choose to tell about our fields can define the way students interact with them, and how rhetoric is used to construct a relationship between science and impact.

The Origins and Evolution of Basic/Applied Rhetoric

Basic/applied rhetoric can be traced back to the nineteenth century when the fields of physics and engineering were professionalizing amidst a flood of research funding associated with industrialization, (Lucier 2012). Physicists and engineers found mutual benefit in distinguishing their fields of expertise, while arguing for the usefulness of their work to common sources of funding. STS scholar Thomas Gieryn referred to the rhetorical tuning between research and its impacts as boundary-work. These boundaries served the purposes of securing funding, protection of intellectual authority, and preserving autonomy from political interference (Gieryn 1983).

From the mid 1800s through WWII basic science was more commonly referred to as pure, often carrying a moral authority over applied science in the minds of its promoters. One of the early advocates of this hierarchy was Henry Rowland, a late 1800s physicist who delivered a “Plea for Pure Science” to the American Association for the Advancement of Science. Rowland made the moral authority of pure scientists clear, writing “We are tired of seeing our professors degrading their chairs by the pursuit of applied science instead of pure science…” (Rowland 1883, 243). His address painted pure science as a hallmark of the dominance of U.S. and western European nations, and argued for more government funding within universities. While he asserted the important role of applied research in making technological advances that benefited society, he did so without ceding moral high ground on which he placed pure science.

The definitions of basic and applied often lean upon the argument that technology descends directly from basic research in physics and chemistry in a linear fashion, (Kline 1995). Rowland argued that, “To have the applications of a science, the science itself must exist.” (Rowland 1883, 242). Many historians of science and technology have argued that this linear model is reductive and doesn’t accurately capture the pathways of technological advance, pointing out that the linear model was crafted by the rhetorical work of scientists like Rowland rather than being an observable process (Gooday 2012; Kline 1995; Lucier 2012).

After World War II (WWII) the word pure shifted to basic, and basic/applied rhetoric was cemented into the structure of federal research funding. Near the end of WWII, President Roosevelt asked Vannevar Bush, the head of the Office of Scientific Research and Development, how best to continue the fruitful relationship between military and science communities into peace-time. His response was the essay *Science, the Endless Frontier* which laid out a vision of federal funding for research that precipitated the founding of the National Science Foundation (NSF) in 1951, (Bush 1945; National Science Foundation, n.d.). In 1946 the ONR was founded in another effort to solidify the relationship between the U.S. military and science (Office of Naval Research, n.d.).

The NSF and the DoD both follow similar definitions of basic and applied research, (Bickell et al. 2024):

> “Basic Research: Experimental or theoretical work undertaken primarily to acquire new knowledge of the underlying foundations of phenomena and observable facts, without any particular application or use in view.

> Applied Research: Original investigation undertaken to acquire new knowledge—directed primarily toward a specific, practical aim or objective."

The primary difference in the definitions is whether a specific objective for the new knowledge is held in mind by the researchers when they write their proposal.

Both organizations fund a combination of basic and applied research but only the DoD distinguishes between basic and applied in a structural way, referring to distinct pools of money. The DoD has nine funding categories for research, development, testing, and evaluation, the first three of which are: 6.1 (Basic Research), 6.2 (Applied Research), and 6.3 (Advanced Technology Development). Each of these categories is defined as being progressively closer to its specific end purpose, and their definitions lean heavily on the concept of a linear progression from basic research to applied research to technology (Sargent 2018).

This pervasive idea of a linear relationship between basic science and technological development was called into question by the DoD's own Project Hindsight, studying the role that basic research played in technology development between WWII and 1962 (Sherwin and Isenson 1967). The report concluded that the knowledge gained by basic research becomes most useful to technological development on timescales longer than the twenty year period they had studied. The authors of the Project Hindsight report noted that recruitment pathways were an indirect benefit of funding basic research that was more immediate than technological progress. As they put it, "Undirected research serves as a form of postdoctoral training; it provides initial jobs for new Ph.D.'s who are inclined toward basic research but who want a closer look at mission-oriented research before making a career commitment" (Sherwin and Isenson 1967, 156). The military recognizes that it can recruit from a wider pool of scientific expertise if it allows participation in relevant but unclassified research. From a more utilitarian angle, graduate students need to publish their research in order to get a degree so it is useful for some military funded work to fall into the unclassified and publishable category.

A 1982 National Academy of the Sciences (NAS) report from the Panel on Science Communication and National Security leans on the flexibility of definitions for basic and applied while arguing against increased secrecy measures in scientific research (Institute of Medicine, National Academy of Sciences, and National Academy of Engineering 1982). At that time the government was worried that scientists were sharing too much with the Soviet Union. Commenting on the NAS report, STS scholar Gieryn points out that, "The boundary-work here is subtle and complex: on one hand, the Panel asserts that university-based science yields "basic" rather than "applied" knowledge; on the other, they assert that university-based science is essential for technological progress." (Gieryn 1983, 791). The NAS panel, which is made up of scientists, describes university research as basic when distancing it from Soviet technological progress, but applied when drawing it closer to technological progress in the United States. This is one example of how basic/applied rhetoric served scientists in navigating the political pressure for secrecy.

Basic/applied rhetoric was co-designed to the mutual benefit of scientists and their patrons throughout the nineteenth and twentieth centuries. It allowed scientists to argue for the usefulness of their research while simultaneously distancing themselves from its impacts for recruitment and in the context of secrecy. Scientists and engineers originally crafted this language to argue for funding during a boom of industrialization while maintaining their intellectual authority and autonomy. In the wake of WWII federal funding agencies adopted the basic/applied framework and made it a structural feature of the research landscape. In the next section we will explore the ways oceanographers framed their work to navigate the shifting funding priorities of the twentieth century, setting the stage for an analysis of contemporary grant abstracts at the Scripps Institution of Oceanography (SIO).

Blurred Boundaries in Military Oceanography

My field of physical oceanography and my employer, SIO, have a relationship with DoD research that goes back to WWII. Oceanographers received funding in ocean state prediction used in Naval operations from submarine warfare to beach landings of ground forces. Naomi Oreskes' book *Science on a Mission* describes the conflict that this influx of military funding created within the field. Some oceanographers resisted the influence of the military on the direction of scientific research while others embraced the prospect of a steady funding source beyond the scale of any pre-war patron.

This tension between oceanographers who sought military patronage and those who craved autonomy for their research direction came to a head at the Woods Hole Oceanographic Institute (WHOI) in 1960 in what later became known as the Palace Revolt. Scientists at WHOI in the late 1950s were concerned that, "Dependence on Navy funding would inevitably shift the balance in oceanography away from basic and towards applied research" (Oreskes 2021, 111). A handful of WHOI scientists were very concerned about the autonomy of their research when the new director, Paul Fye, began to push for a closer relationship with the Navy and a more direct focus on its operational needs. Fye had a background in munitions development, and some saw him as closer to the military than to oceanography. The concerned WHOI scientists included prominent deep sea physicist Henry Stommel and influential atmospheric scientist Joanne Malkus, who wrote to members of the Board of Trustees asking for Fye's removal and made public statements of protest. In the end, both of these scientists ended up leaving WHOI because they were uncomfortable with the close relationship it was cultivating with the Navy.

At SIO, the resistance to military funding seemed to be primarily founded on the disproportionate support of physics and geology over biological sciences, as SIO was originally founded as a marine biological station in 1907. The Marine Physical Laboratory (MPL) was founded in 1946 as a post-WWII continuation of the University of California Division of War Research, inheriting much of its initial equipment and staff from the Navy Electronics Laboratory and receiving most of its funding from the Office of Naval Research. MPL is now the oldest research division within SIO and accounts for a large portion of contemporary physical oceanography research at SIO. In their 2003 article on the history of MPL, SIO scientists Fred Spiess and Bill Kuperman refer to the 1960s as the Golden Age of Growth for MPL, facilitated by their close relationship with the Navy (Spiess and Kuperman 2003). In its conclusion the article states that "MPL currently pursues basic observational ocean science by a combination of in situ measurements and remote sensing." Although these MPL leaders self-describe its research as basic, earlier in the article they describe the direct application of their research to specific Naval technologies including submarine sonar and tactical communication systems, and a hydrophone array that was installed on an "experimental U.S. submarine". The DoD definition of basic research states that it is "without any particular application or use in view" (Bickell et al. 2024). It appears that in practice this distinction was tunable.

Funding sources began to diversify throughout the 1970s and research topics spread out from the portfolio of the first two decades at MPL that was more directly relevant to military operations. In response to the apparent waning of military support for university based research the directors of four university housed applied laboratories, including MPL, co-authored the report *The Role of University Laboratories in Navy Research and Development* to argue for increased funding (Hampton et al. 1983). The report outlines the unique technical expertise that had been developed at each laboratory due to the funding prioritization of the DoD. It argues that "This unique position of the laboratories, with close ties to both the Navy and their parent institutions, allows them to serve as a valuable interface between Navy 6.1 (basic) and 6.2 (applied) Technology Base programs and the talent, resources, and technology available within their respective universities" (Hampton et al. 1983, 2). They additionally point out that "their positioning within universities allows for training students and professionals in Navy-related areas of ocean science, which provides a flow of experienced people into Technology Base programs", highlighting the value of academia for recruitment (Hampton et al. 1983, 2). The roles of both basic and applied research are emphasized within the same institutions, distinguishable only by their funding source from either the 6.1 or 6.2 pool. Rather than forming a boundary between groups of scientists or research topics, both types of research are performed by the same groups of people. The only distinction between basic and applied seems to be an intentionality at the moment of funding.

Abstract Analysis

Here we examine the usage of the words basic and applied within all of the successfully funded DoD and NSF grant abstracts from SIO with start dates in the time period of January 2015 through January 2025. Our analysis is done with a specific eye to the functional role of this language in the relationship between academia and the military. For this study I created a database of funded NSF and DoD grant abstracts by searching in the publicly available NSF active award database and Defense Technical Information Center for the years 2015 to 2025 (National Science Foundation, n.d., Defense Technical Information Center, n.d.). I was unable to search for SIO directly in the DoD database, only its parent organization the University of California San Diego. For the DoD database I additionally did an internet search of the name of every Principal Investigator (PI) I didn't know personally to identify SIO affiliations. The assembled list consists of 139 NSF grants and 288 DoD grants. For each entry I recorded the grant numbers, titles, start and end dates, PI names, and abstracts. I cross-referenced the PI's names with their SIO academic profiles and added the research units and the curricular groups with which they identify. Next, I read through all of the abstracts and pulled out any place names that were mentioned, adding an approximate latitude and longitude. Finally, I found every use of the words basic and applied and noted whether the word was being used to describe research. I noted whether the word was being used as juxtaposition, for example in the phrase "basic and applied research", and whether the word was immediately adjacent to a phrase like "Navy relevant" or "of Naval interest". The database consists of only publicly available information, and the specific compilation I used for my study will be made available for public use in an open-access repository.

Before looking into abstract language, we will take a broad view of the structure and distribution of NSF and DoD funding at SIO. The Office of Naval Research (ONR) accounts for an average of 28 percent of funding at SIO between the years 2015 and 2022, for which annual reports with funding information are publicly available (Scripps Institution of Oceanography 2023). During the same period the NSF accounted for 26 percent of SIO funding. MPL received 67 percent of ONR funding at SIO from 2015 to 2025, while it only received 9 percent of NSF funding. The distribution of funding across the eight SIO research divisions that received funding from either NSF or DoD from 2015 to 2025 is shown in Figure 1. The research divisions are: the Marine Physical Laboratory (MPL); Climate, Atmospheric

Science, and Physical Oceanography (CASPO); the Center for Marine Biotechnology and Biomedicine (CMB); the Institute of Geophysics and Planetary Physics (IGPP); the Integrated Oceanography Division (IOD); the SIO Department (SIO); Marine Biology (MB); and the Geophysical Research Division (GRD). Any PIs that don't fall under a research division are listed as 'undefined', which largely accounts for funding received for SIO research vessels. MPL received the majority of DoD funding, in a continuation of their historical relationship. The DoD's prioritization of oceanography, geophysics, and atmospheric science over biology can be seen in the distribution as well, confirming the fears of pre-WWII SIO biologists. NSF funding is much more evenly spread across disciplines.

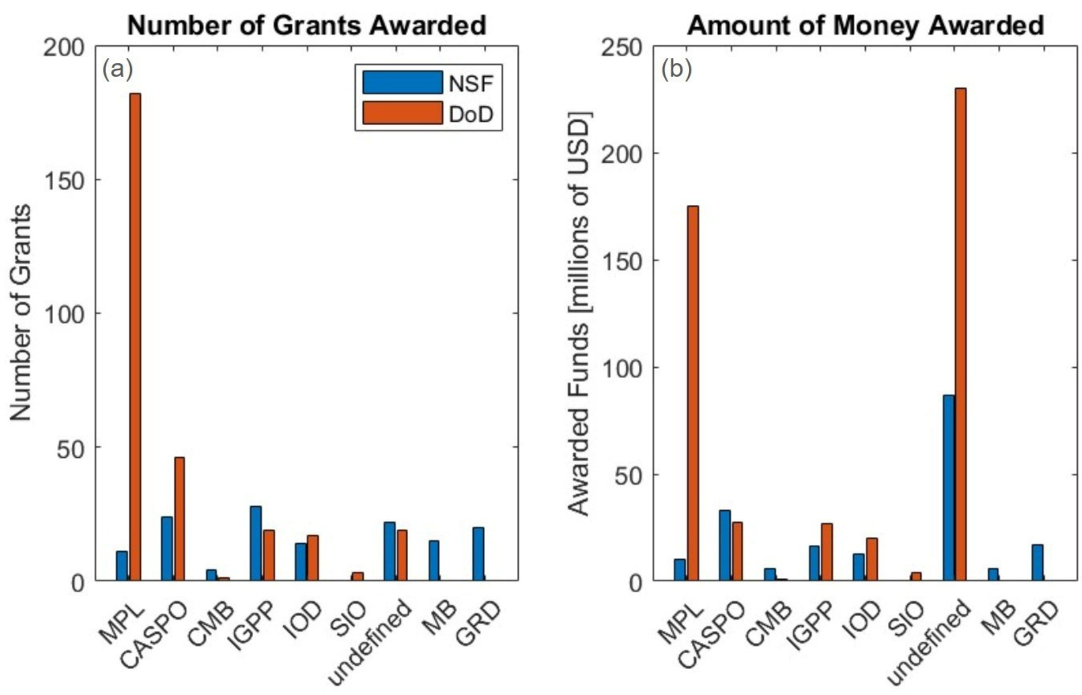

Figure 4.1: [a] Number of grants awarded across the eight of SIO's research divisions funded by NSF and/or DoD within the period 2015-2025 [b] Awarded funds by research division from 2015-2025.

Now that we've oriented ourselves within the landscape of NSF and DoD funding at SIO, we return to the language scientists use to describe their research in their abstracts. Out of 139 NSF abstracts three include the word basic, one of which is using it to describe research. Five NSF abstracts use the word applied, but none of them are using it to describe research. Within 288 DoD abstracts, 287 of which are funded by ONR, twenty five use the word basic with seventeen of those uses refer to research. Thirteen ONR abstracts use the word applied, six of which use it to describe research. The basic/applied framework is used more commonly within abstract language directed at the ONR, and is almost entirely absent from NSF abstracts. This makes sense given that the distinction between the two is built into the funding structure of the DoD and represents two distinct pools of money. The question is then, why does basic/applied rhetoric serve the ONR but not the NSF? Both organizations fund a combination of research they identify as basic or applied, but one of them made the distinction structural. What functional role is this distinction playing in the relationship between the military and academia? To answer these questions we will draw from specific examples of basic/applied rhetoric within the abstracts.

SIO abstracts directed at ONR were almost twice as likely to describe themselves as basic as they were applied, which may indicate that more of SIO's funding comes from the 6.1 pool. Out of the twenty five uses of the word basic, five additionally qualified their research as "Navy-relevant" or "of Naval interest". The end use isn't specific enough to identify their work as applied, but they do know enough about its potential usefulness to argue for Navy relevance. This is indicative of the grey areas in a rhetorical distinction that seems to be defined by intentionality. The intertwining of the words basic and applied extends to, in many cases, using them directly next to each other as a juxtaposed pair. Five of the twenty five abstracts that use the word basic fall into this category, using the phrase “basic and applied” to indicate that their research project will include elements of both types of research or that the results of their research has multiple end uses.

Two functional roles of the basic/applied framework were repeated throughout many of the ONR abstracts. The first was that many of the projects seem to serve dual data pathways. Some of the data goes towards a research question of the PI, and other data goes directly to Navy organizational units for operational purposes. Military organizations called out in the abstracts for collaboration or direct transmission of data include: the Naval Undersea Warfare Center, Naval Information Warfare Center, Naval Oceanographic Office, Naval Research Lab, National Geospatial Intelligence Agency, Defense Mapping Agency, Unmanned Undersea Vehicle Squadron, Commander Task Force 75 in Guam, Naval Special Warfare, US Indo-Pacific Command, Naval Mine and Anti-Submarine Command, and the Undersea Warfighting Development Center.

Several abstracts mention the strategic significance of the locations where data will be collected. Approximate locations of all of the place names mentioned in abstracts are plotted in Figure 2. Some of the points are plotted from descriptions as vague as “the North Atlantic” while others are more specific, such as “Dongsha Atoll in the South China Sea” or “the Vietnamese waters of the Gulf of Tonkin”. The clustering of DoD areas of study as compared to NSF is reflective of a mode of research funding called Department Research Initiatives (DRIs). In a call for abstracts for a DRI PIs will often be asked to propose a research project in a prescribed location. The result is an intensive focus on one area and subject matter by many PIs, resulting in a less even spatial distribution than NSF, and a focus on regions that the Navy has determined to be operationally significant.

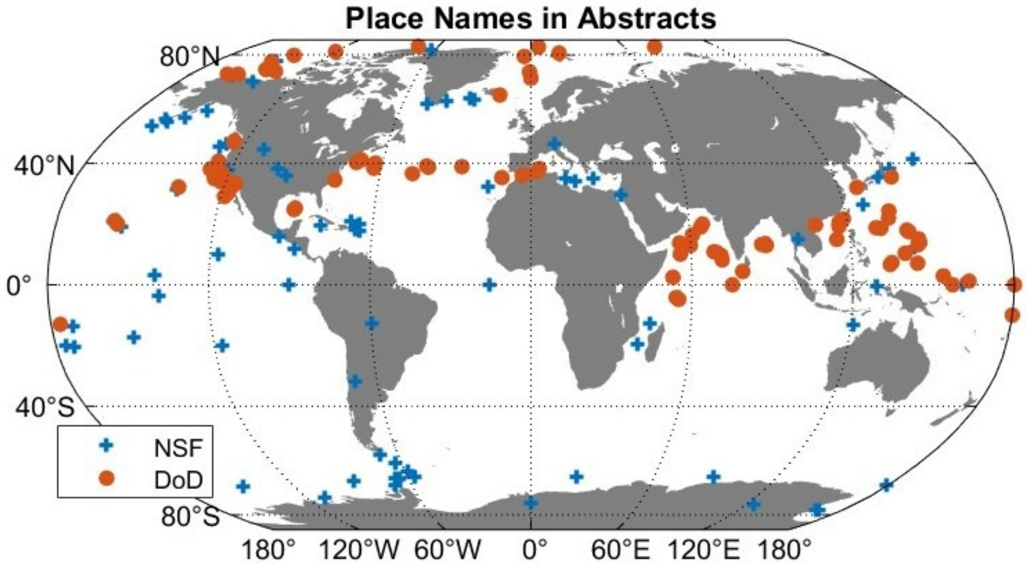

Figure 4.2: Approximate locations of the place names mentioned in abstracts from the NSF (blue plus signs) and DoD (red circles)

The distinction between data pathways in proposed projects is sometimes demarcated using the basic/applied framework, as in the example below with names redacted:

> "The basic science/signal processing research effort in this proposed program will be conducted mostly by two Scripps (SIO) graduate students, XXX and XXX, under the supervision of their co-advisors XXX, XXX, and XXX. Results will be published in peer-reviewed papers and the students' Ph.D. theses. Transition of fleet-relevant results will be coordinated via ONR Code 32 to the relevant U.S. Navy activities, including Undersea Warfighting Development Center (UWDC) in San Diego."

In this example basic research is designated as work to be conducted in a university setting by students while other results of the funded work will be communicated to military organizations. Other examples propose some elements of the project to be performed in collaboration with military organizations, such as one proposal that promises to, "coordinate our research efforts with the Defense Mapping Agency, the Naval Oceanographic Office and make these grids available to Navy labs, defense contractors and the general public."

The functional role of recruitment in the basic/applied framework is also apparent in the abstract quote above. The designation of some work as basic enables it to be conducted by students and published as a part of their thesis dissertations. Students need to publish their work to graduate, but it is also useful for recruitment purposes to have students begin to work on military research early in their careers, so the DoD benefits from funding some initiatives that are not as directly tied to military operations and require no classified data. This recruitment consideration was noted in Project Hindsight (Sherwin and Isenson 1967), the 1983 report by Applied Research Laboratories (Hampton et al. 1983), and the 2003 article on MPL history (Spiess and Kuperman 2003). Many abstracts in our collection mention that funds will be used to support student salaries. One goes so far as to say, "Postdocs and students supported under the proposed effort will become the backbone and workforce of future DoD research". Another abstract says, "Training the next generation of scientists and engineers through hands-on research experience using innovative curricula is critical to future Navy outcomes". Recruitment, education, or retention of students is mentioned in 44 out of 288 abstracts. One abstract identifies the specific interplay between recruitment and basic research, stressing its mutual benefit to both the Navy and the research community:

> "From a naval interest, this research ultimately enables a broad swath of naval interests associated with exploiting technical advantages as an offset strategy to counter adversary interests. As a research community, our enduring relationship with the Office of Naval Research furthers technical advantage by vertically integrating basic and applied research

that supports short- and long-term interests. A key element of the latter is education of the next generation workforce both as civilians and active duty."

The "vertical-integration of basic and applied research" paints a picture of the two working hand in hand. Seen as a whole, our abstract database indicates that basic and applied research are often conducted by the same people with the same ultimate end use in mind, but with different proximity to that use. The DoD identified on its own in Project Hindsight that funding basic research paid little dividends in warfighting capability on timescales shorter than many decades; yet they continue to fund it. The functional roles in the military-academy relationship of data acquisition and recruitment, demonstrated by the rhetoric scientists use to define and categorize themselves, offer some insight into the more immediate benefits that are offered to the military in exchange for their patronage.

The Basic/Applied Framework in Complicity

By examining the language that oceanographers use to describe their work when asking the Navy for funding, we've begun to clarify the obscured military-university relationship to reveal two short-term functional roles it serves. Data often follows dual pathways, one of which becomes part of students' research projects and is often referred to as basic, and another that is deemed operationally relevant and routed to one of many military organizations. We have seen that the basic/applied framework is not always used at SIO to differentiate distinct areas of research, but rather it allows the same projects to serve multiple purposes. While the NSF and the DoD both fund research that ranges in proximity to its end use, and fits the historical definitions of basic or applied, only one of these organizations chose to structurally compartmentalize its funding streams.

In addition to controlling the perceived relevance of research to its end use and end user, the basic/applied framework determines the proximity of students to the impacts of their work. This veil of obfuscation allows students such as myself to conduct research on a Navy project while wondering what interest the military could possibly have in the results. In an era where students are publicly challenging the ties between the military and the university, the rhetorical framework examined here allows many graduate students to hold the belief that their work is taking away from the military's objectives rather than promoting them. My hope is that this analysis will be useful not only to the feminist science and technology studies community, but also to future generations of students who have questions about where their funding is coming from and why.

Acknowledgements

I would like to thank Professor bt werner for their support in this chapter, for showing me that there are many ways to do science and exist within scientific institutions, and for creating spaces at SIO and UCSD for students to critically evaluate their fields and institutions.

Chapter 4, in part is currently being prepared for submission for publication of the material. Bellerjeau, Charlotte. "Basic or Applied: Complicity and Tuning the Proximity of Research to its Impacts". The dissertation author was the primary investigator and author of this material.

REFERENCES

Achatz, U., Alexander, M. J., Becker, E., Chun, H.-Y., Dörnbrack, A., Holt, L., Plougonven, R., Polichtchouk, I., Sato, K., Sheshadri, A., Stephan, C. C., Niekerk, A. van, & Wright, C. J. (2024). *Atmospheric Gravity Waves: Processes and Parameterization*. https://doi.org/10.1175/JAS-D-23-0210.1

Alberty, M. S., Billheimer, S., Hamann, M. M., Ou, C. Y., Tamsitt, V., Lucas, A. J., & Alford, M. H. (2017). A reflecting, steepening, and breaking internal tide in a submarine canyon. *Journal of Geophysical Research: Oceans*, *122*(8), 6872–6882. https://doi.org/10.1002/2016JC012583

Alford, M. H. (2010). Sustained, Full-Water-Column Observations of Internal Waves and Mixing near Mendocino Escarpment. *Journal of Physical Oceanography*, *40*(12), 2643–2660. https://doi.org/10.1175/2010JPO4502.1

Alford, M. H., & Gregg, M. C. (2001). Near-inertial mixing: Modulation of shear, strain and microstructure at low latitude. *Journal of Geophysical Research: Oceans*, *106*(C8), 16947–16968. https://doi.org/10.1029/2000JC000370

Alford, M. H., Le Boyer, A., Ren, A. S., Voet, G., Bellerjeau, C., Whalen, C. B., Hall, B., & Couto, N. (2025). Observations of Turbulence Generated by a Near-Inertial Wave Propagating Downward in an Anticyclonic Eddy. *Geophysical Research Letters*, *52*(6), e2024GL114070. https://doi.org/10.1029/2024GL114070

Alford, M. H., & MacCready, P. (2014). Flow and mixing in Juan de Fuca Canyon, Washington. *Geophysical Research Letters*, *41*(5), 1608–1615. https://doi.org/10.1002/2013GL058967

Alford, M. H., MacKinnon, J. A., Simmons, H. L., & Nash, J. D. (2016). Near-Inertial Internal Gravity Waves in the Ocean. *Annual Review of Marine Science*, *8*(Volume 8, 2016), 95–123. https://doi.org/10.1146/annurev-marine-010814-015746

Alford, M. H., Shcherbina, A. Y., & Gregg, M. C. (2013). *Observations of Near-Inertial Internal Gravity Waves Radiating from a Frontal Jet*. https://doi.org/10.1175/JPO-D-12-0146.1

Alford, M. H., Wynne-Cattanach, B., Boyer, A. L., Couto, N., Voet, G., Spingys, C. P., Castro, B. F., Forryan, A., Garabato, A. C. N., & Haren, H. van. (2024). *Buoyancy flux and mixing efficiency from direct, near-bottom turbulence measurements in a submarine canyon*. https://doi.org/10.1175/JPO-D-24-0005.1

Alford, M., & Pinkel, R. (2000). *Patterns of Turbulent and Double-Diffusive Phenomena: Observations from a Rapid-Profiling Microconductivity Probe*. https://journals.ametsoc.org/view/journals/phoc/30/5/1520-0485_2000_030_0833_potadd_2.0.co_2.xml

Aluie, H., Hecht, M., & Vallis, G. K. (2018). Mapping the Energy Cascade in the North Atlantic Ocean: The Coarse-Graining Approach. *Journal of Physical Oceanography*, *48*(2), 225–244. https://doi.org/10.1175/JPO-D-17-0100.1

Anderson, J. (2011). *Fundamentals of Aerodynamics* (5th ed.). McGraw-Hill.
Andres, M., Donohue, K. A., & Toole, J. M. (2020). The Gulf Stream's path and time-averaged velocity structure and transport at 68.5°W and 70.3°W. *Deep Sea Research Part I: Oceanographic Research Papers*, *156*, 103179. https://doi.org/10.1016/j.dsr.2019.103179

Andrews, D. G., & McIntyre, M. E. (1976). *Planetary Waves in Horizontal and Vertical Shear: The Generalized Eliassen-Palm Relation and the Mean Zonal Acceleration*. https://journals.ametsoc.org/view/journals/atsc/33/11/1520-0469_1976_033_2031_pwihav_2_0_co_2.xml

Babu, I., & de With, G. (2014). Highly flexible piezoelectric 0–3 PZT–PDMS composites with high filler content. *Composites Science and Technology*, *91*, 91–97. https://doi.org/10.1016/j.compscitech.2013.11.027

Barkan, R., Srinivasan, K., Yang, L., McWilliams, J. C., Gula, J., & Vic, C. (2021a). Oceanic Mesoscale Eddy Depletion Catalyzed by Internal Waves. *Geophysical Research Letters*, *48*(18), e2021GL094376. https://doi.org/10.1029/2021GL094376

Barkan, R., Srinivasan, K., Yang, L., McWilliams, J. C., Gula, J., & Vic, C. (2021b). Oceanic Mesoscale Eddy Depletion Catalyzed by Internal Waves. *Geophysical Research Letters*, *48*(18), e2021GL094376. https://doi.org/10.1029/2021GL094376

Barkan, R., Winters, K. B., & McWilliams, J. C. (2017). *Stimulated Imbalance and the Enhancement of Eddy Kinetic Energy Dissipation by Internal Waves*. https://doi.org/10.1175/JPO-D-16-0117.1
Bell, T. H. (1975). Lee waves in stratified flows with simple harmonic time dependence. *Journal of Fluid Mechanics*, *67*(4), 705–722. https://doi.org/10.1017/S0022112075000560

Bickell, E. G., Blevins, E. G., DeSantis, M. K., Gallo, M. E., Harris, L., Humphreys, B. E., & Jones, A. C. (n.d.). *Federal Research and Development (R&D) Funding: FY2025*. Library of Congress. Retrieved April 5, 2026, from https://www.congress.gov/crs-product/R48307

Bowen, C. R., Perry, A., Lewis, A. C. F., & Kara, H. (2004). Processing and properties of porous piezoelectric materials with high hydrostatic figures of merit. *Journal of the European Ceramic Society, 8th International Conference on Ceramic Processing*, *24*(2), 541–545. https://doi.org/10.1016/S0955-2219(03)00194-8

Bühler, O. (2014). *Waves and Mean Flows* (2nd ed.). Cambridge University Press. https://doi.org/10.1017/CBO9781107478701

Bühler, O., & McIntyre, M. E. (1999). *On Shear-Generated Gravity Waves that Reach the Mesosphere. Part II: Wave Propagation*.

https://journals.ametsoc.org/view/journals/atsc/56/21/1520-0469_1999_056_3764_osggwt_2.0.co_2.xml

Bush, V. (1945). *Science: The Endless Frontier*. https://nsf-gov-resources.nsf.gov/2023-04/EndlessFrontier75th_w.pdf

Cartier, K. M. S. (2021, March 9). *Teaching Geoscience History in Context*. Eos. http://eos.org/articles/teaching-geoscience-history-in-context

Conn, S., & Callies, J. (2026). *Global Near-Inertial Wave Spectra Shaped by Mesoscale Eddies*. https://doi.org/10.1175/JPO-D-25-0163.1

Cui, H., Hensleigh, R., Yao, D., Maurya, D., Kumar, P., Kang, M. G., Priya, S., & Zheng, X. (Rayne). (2019). Three-dimensional printing of piezoelectric materials with designed anisotropy and directional response. *Nature Materials*, *18*(3), 234–241. https://doi.org/10.1038/s41563-018-0268-1

de Lavergne, C., Madec, G., Capet, X., Maze, G., & Roquet, F. (2016). Getting to the bottom of the ocean. *Nature Geoscience*, *9*(12), 857–858. https://doi.org/10.1038/ngeo2850

de Marez, C., Lahaye, N. J., & Gula, J. (2020). Interaction of the Gulf Stream with small scale topography: A focus on lee waves. *Scientific Reports*, *10*(1), 2332. https://doi.org/10.1038/s41598-020-59297-5

Defense Technical Information Center. (n.d.). *DTIC Award Database* [Dataset]. Retrieved May 2, 2026, from https://dtic.dimensions.ai/discover/grant?or_facet_research_org=grid.266100.3

Dematteis, G., Le Boyer, A., Pollmann, F., Polzin, K. L., Alford, M. H., Whalen, C. B., & Lvov, Y. V. (2024). Interacting internal waves explain global patterns of interior ocean mixing. *Nature Communications*, *15*(1), 7468. https://doi.org/10.1038/s41467-024-51503-6

Doherty, K. W., Frye, D. E., Liberatore, S. P., & Toole, J. M. (1999). A Moored Profiling Instrument*. *Journal of Atmospheric and Oceanic Technology*, *16*(11), 1816–1829. https://doi.org/10.1175/1520-0426(1999)016%253C1816:AMPI%253E2.0.CO;2

Duda, T. F., & Cox, C. S. (1987). Vorticity measurement in a region of coastal ocean eddies by observation of near-inertial oscillations. *Geophysical Research Letters*, *14*(8), 793–796. https://doi.org/10.1029/GL014i008p00793

Eden, C., Pollmann, F., & Olbers, D. (2019). Numerical Evaluation of Energy Transfers in Internal Gravity Wave Spectra of the Ocean. *Journal of Physical Oceanography*, *49*(3), 737–749. https://doi.org/10.1175/JPO-D-18-0075.1

Egbert, G. D., & Erofeeva, S. Y. (2002). *Efficient Inverse Modeling of Barotropic Ocean Tides*. https://journals.ametsoc.org/view/journals/atot/19/2/1520-0426_2002_019_0183_eimobo_2_0_co_2.xml

Eliassen, A., & Palm, E. (1961). *On the Transfer of Energy in Stationary Mountain Waves*. I kommisjon hos Aschehoug.

Eriksen, C. C. (1982). Observations of internal wave reflection off sloping bottoms. *Journal of Geophysical Research: Oceans*, *87*(C1), 525–538. https://doi.org/10.1029/JC087iC01p00525

Essink, S., Kunze, E., Lien, R.-C., Inoue, R., & Ito, S. (2022). *Near-Inertial Wave Interactions and Turbulence Production in a Kuroshio Anticyclonic Eddy*. https://doi.org/10.1175/JPO-D-21-0278.1

Ferrari, R., Mashayek, A., McDougall, T. J., Nikurashin, M., & Campin, J.-M. (2016). Turning Ocean Mixing Upside Down. *Journal of Physical Oceanography*, *46*(7), 2239–2261. https://doi.org/10.1175/JPO-D-15-0244.1

Ferrari, R., & Wunsch, C. (2009). Ocean Circulation Kinetic Energy: Reservoirs, Sources, and Sinks. *Annual Review of Fluid Mechanics*, *41*(Volume 41, 2009), 253–282. https://doi.org/10.1146/annurev.fluid.40.111406.102139

Ganeshkumar, R., Cheah, C. W., Xu, R., Kim, S.-G., & Zhao, R. (2017). A high output voltage flexible piezoelectric nanogenerator using porous lead-free KNbO3 nanofibers. *Applied Physics Letters*, *111*(1), 013905. https://doi.org/10.1063/1.4992786

Garrett, C. (2001). *What is the "Near-Inertial" Band and Why Is It Different from the Rest of the Internal Wave Spectrum?* https://journals.ametsoc.org/view/journals/phoc/31/4/1520-0485_2001_031_0962_witnib_2.0.co_2.xml

Garrett, C., & Munk, W. (1972). Space-Time scales of internal waves. *Geophysical Fluid Dynamics*, *3*(3), 225–264. https://doi.org/10.1080/03091927208236082

Gieryn, T. F. (1983). Boundary-Work and the Demarcation of Science from Non-Science: Strains and Interests in Professional Ideologies of Scientists. *American Sociological Review*, *48*(6), 781–795. https://doi.org/10.2307/2095325

Giordano, S. (2025). *Labs of Our Own: FeministTinkerings with Science*. Rutgers University Press.

Gonella, J. (1972). A rotary-component method for analysing meteorological and oceanographic vector time series. *Deep Sea Research and Oceanographic Abstracts*, *19*(12), 833–846. https://doi.org/10.1016/0011-7471(72)90002-2

Gooday, G. (2012). "Vague and Artificial": The Historically Elusive Distinction between Pure and Applied Science. *Isis*, *103*(3), 546–554. https://doi.org/10.1086/667978

Greatbatch, R. J., Zhai, X., Kohlmann, J.-D., & Czeschel, L. (2010). Ocean eddy momentum fluxes at the latitudes of the Gulf Stream and the Kuroshio extensions as revealed by satellite data. *Ocean Dynamics*, *60*(3), 617–628. https://doi.org/10.1007/s10236-010-0282-6

Gregg, M. C. (1989). Scaling turbulent dissipation in the thermocline. *Journal of Geophysical Research: Oceans*, *94*(C7), 9686–9698. https://doi.org/10.1029/JC094iC07p09686

Gregg, M. C. (1999). *Uncertainties and Limitations in Measuring ε and χT*. https://journals.ametsoc.org/view/journals/atot/16/11/1520-0426_1999_016_1483_ualima_2_0_co_2.xml

Gregg, M. C., Sanford, T. B., & Winkel, D. P. (2003). Reduced mixing from the breaking of internal waves in equatorial waters. *Nature*, *422*(6931), 513–515. https://doi.org/10.1038/nature01507

Gula, J., Molemaker, M. J., & McWilliams, J. C. (2015). *Gulf Stream Dynamics along the Southeastern U.S. Seaboard*. https://doi.org/10.1175/JPO-D-14-0154.1

Hampton, L., Hettche, L. R., Murphy, S., & Watson, K. (1983). *The Role of University Laboratories in Navy Research and Development*. APL, ARL, ARL-PSU, MPL.

Henyey, F. S., Wright, J., & Flatté, S. M. (1986). Energy and action flow through the internal wave field: An eikonal approach. *Journal of Geophysical Research: Oceans*, *91*(C7), 8487–8495. https://doi.org/10.1029/JC091iC07p08487

Hersbach, H., Bell, B., Berrisford, P., Hirahara, S., Horányi, A., Muñoz-Sabater, J., Nicolas, J., Peubey, C., Radu, R., Schepers, D., Simmons, A., Soci, C., Abdalla, S., Abellan, X., Balsamo, G., Bechtold, P., Biavati, G., Bidlot, J., Bonavita, M., … Thépaut, J.-N. (2020). The ERA5 global reanalysis. *Quarterly Journal of the Royal Meteorological Society*, *146*(730), 1999–2049. https://doi.org/10.1002/qj.3803

Hickey, B. M. (1995). *Coastal Submarine Canyons*.

Hollin, G., & Williams, R. (2022). Complicity: Methodologies of power, politics and the ethics of knowledge production. *Sociology of Health & Illness*, *44*(S1), 1–21. https://doi.org/10.1111/1467-9566.13575

Ijichi, T., & Hibiya, T. (2015). Frequency-Based Correction of Finescale Parameterization of Turbulent Dissipation in the Deep Ocean. *Journal of Atmospheric and Oceanic Technology*, *32*(8), 1526–1535. https://doi.org/10.1175/JTECH-D-15-0031.1

Institute of Medicine, National Academy of Sciences, & National Academy of Engineers. (1982). *Scientific Communication and National Security*. The National Academy Press. https://doi.org/10.17226/253

Jbaily, A., & Yeung, R. W. (2015). Piezoelectric devices for ocean energy: A brief survey. *Journal of Ocean Engineering and Marine Energy*, *1*(1), 101–118. https://doi.org/10.1007/s40722-014-0008-9

Kim, Y., Eckermann, S. D., & Chun, H. (2003). An overview of the past, present and future of gravity-wave drag parametrization for numerical climate and weather prediction models. *Atmosphere-Ocean*, *41*(1), 65–98. https://doi.org/10.3137/ao.410105

Kline, R. (1995). Construing "Technology" as "Applied Science": Public Rhetoric of Scientists and Engineers in the United States, 1880-1945. *Isis*, *86*(2), 194–221.

Klymak, J. M., Pinkel, R., & Rainville, L. (2008). Direct Breaking of the Internal Tide near Topography: Kaena Ridge, Hawaii. *Journal of Physical Oceanography*, *38*(2), 380–399. https://doi.org/10.1175/2007JPO3728.1

Kumar, P., & Foufoula-Georgiou, E. (1997). Wavelet analysis for geophysical applications. *Reviews of Geophysics*, *35*(4), 385–412. https://doi.org/10.1029/97RG00427

Kundu, P. K., & Cohen, I. M. (2010). *Fluid Mechanics*. Academic Press.
Kunze, E. (1985). *Near-Inertial Wave Propagation In Geostrophic Shear*. https://journals.ametsoc.org/view/journals/phoc/15/5/1520-0485_1985_015_0544_niwpig_2_0_co_2.xml

Kunze, E., MacKay, C., McPhee-Shaw, E. E., Morrice, K., Girton, J. B., & Terker, S. R. (2012). *Turbulent Mixing and Exchange with Interior Waters on Sloping Boundaries*. https://doi.org/10.1175/JPO-D-11-075.1

Kunze, E., Rosenfeld, L. K., Carter, G. S., & Gregg, M. C. (2002). Internal Waves in Monterey Submarine Canyon. *Journal of Physical Oceanography*, *32*(6), 1890–1913. https://doi.org/10.1175/1520-0485(2002)032%253C1890:IWIMSC%253E2.0.CO;2

Kunze, E., Schmitt, R. W., & Toole, J. M. (1995). *The Energy Balance in a Warm-Core Ring's Near-Inertial Critical Layer*. https://journals.ametsoc.org/view/journals/phoc/25/5/1520-0485_1995_025_0942_tebiaw_2_0_co_2.xml

Le Boyer, A., & Alford, M. H. (2021). Variability and Sources of the Internal Wave Continuum Examined from Global Moored Velocity Records. *Journal of Physical Oceanography*, *51*(9), 2807–2823. https://doi.org/10.1175/JPO-D-20-0155.1

Le Boyer, A., Alford, M. H., Couto, N., Goldin, M., Lastuka, S., Goheen, S., Nguyen, S., Lucas, A. J., & Hennon, T. D. (2021a). Modular, Flexible, Low-Cost Microstructure Measurements: The Epsilometer. *Journal of Atmospheric and Oceanic Technology*, *38*(3), 657–668. https://doi.org/10.1175/JTECH-D-20-0116.1

Le Boyer, A., Alford, M. H., Couto, N., Goldin, M., Lastuka, S., Goheen, S., Nguyen, S., Lucas, A. J., & Hennon, T. D. (2021b). *Modular, Flexible, Low-Cost Microstructure Measurements: The Epsilometer*. https://doi.org/10.1175/JTECH-D-20-0116.1

Le Boyer, A., Couto, N., Alford, M. H., Drake, H. F., Bluteau, C. E., Hughes, K. G., Naveira Garabato, A. C., Moulin, A. J., Peacock, T., Fine, E. C., Mashayek, A., Cimoli, L., Meredith, M. P., Melet, A., Fer, I., Dengler, M., & Stevens, C. L. (2023). Turbulent diapycnal fluxes as a pilot Essential Ocean Variable. *Frontiers in Marine Science*, *10*. https://doi.org/10.3389/fmars.2023.1241023

Leaman, K. D., & Sanford, T. B. (1975). Vertical energy propagation of inertial waves: A vector spectral analysis of velocity profiles. *Journal of Geophysical Research (1896-1977)*, *80*(15), 1975–1978. https://doi.org/10.1029/JC080i015p01975

Lee, C. M., & Eriksen, C. C. (1997). Near-inertial internal wave interactions with mesoscale fronts: Observations and models. *Journal of Geophysical Research: Oceans*, *102*(C2), 3237–3253. https://doi.org/10.1029/96JC03209

Lee, T., & Cornillon, P. (1996). *Propagation and Growth of Gulf Stream Meanders between 75° and 45°W*. https://journals.ametsoc.org/view/journals/phoc/26/2/1520-0485_1996_026_0225_pagogs_2_0_co_2.xml

Liboiron, M. (2021). *Pollution Is Colonialism*. Duke University Press. https://doi.org/10.2307/j.ctv1jhvnk1

Lighthill, S. M. J. (1978). *Waves in Fluids*. Cambridge University Press.
Lim, J. (2025, October 13). *Uncensored: Student-led tour traces UVSD's hidden histories of student activism*. https://ucsdguardian.org/2025/10/13/uncensored-student-led-tour-traces-ucsds-hidden-histories-of-student-activism/

Lindzen, R. S. (1973). Wave-mean flow interactions in the upper atmosphere. *Boundary-Layer Meteorology*, *4*(1), 327–343. https://doi.org/10.1007/BF02265242

Lucier, P. (2012). The Origins of Pure and Applied Science in Gilded Age America. *Isis*, *103*(3), 527–536. https://doi.org/10.1086/667976

Lueck, R. G., Wolk, F., & Yamazaki, H. (2002). Oceanic Velocity Microstructure Measurements in the 20th Century. *Journal of Oceanography*, *58*(1), 153–174. https://doi.org/10.1023/A:1015837020019

Lumpkin, R., & Speer, K. (2007). *Global Ocean Meridional Overturning*. https://doi.org/10.1175/JPO3130.1

Lvov, Y. V., Polzin, K. L., & Tabak, E. G. (2004). Energy Spectra of the Ocean's Internal Wave Field: Theory and Observations. *Physical Review Letters*, *92*(12), 128501. https://doi.org/10.1103/PhysRevLett.92.128501

MacKinnon, J. A., & Winters, K. B. (2005). Subtropical catastrophe: Significant loss of low-mode tidal energy at 28.9°. *Geophysical Research Letters*, *32*(15). https://doi.org/10.1029/2005GL023376

MacKinnon, J. A., Zhao, Z., Whalen, C. B., Waterhouse, A. F., Trossman, D. S., Sun, O. M., Laurent, L. C. S., Simmons, H. L., Polzin, K., Pinkel, R., Pickering, A., Norton, N. J., Nash, J. D., Musgrave, R., Merchant, L. M., Melet, A. V., Mater, B., Legg, S., Large, W. G., … Alford, M. H. (2017). *Climate Process Team on Internal Wave–Driven Ocean Mixing*. https://doi.org/10.1175/BAMS-D-16-0030.1

McCall, W. R., Kim, K., Heath, C., La Pierre, G., & Sirbuly, D. J. (2014). Piezoelectric Nanoparticle–Polymer Composite Foams. *ACS Applied Materials & Interfaces*, *6*(22), 19504–19509. https://doi.org/10.1021/am506415y

McFarlane, N. A. (1987). *The Effect of Orographically Excited Gravity Wave Drag on the General Circulation of the Lower Stratosphere and Troposphere*. https://journals.ametsoc.org/view/journals/atsc/44/14/1520-0469_1987_044_1775_teooeg_2_0_co_2.xml

Mcintyre, M. E. (1981). On the 'wave momentum' myth. *Journal of Fluid Mechanics*, *106*, 331–347. https://doi.org/10.1017/S0022112081001626

MeasurementSpecialtiesInc. (1999, April 2). *Piezo Film Sensors Technical Manual*. https://www.sparkfun.com/datasheets/Sensors/Flex/MSI-techman.pdf

Melet, A. V. (2022). The role of ocean mixing in the climate system. In *Ocean Mixing* (pp. 5–34). Elsevier. https://doi.org/10.1016/B978-0-12-821512-8.00009-8

Miles, J. W., & Howard, L. N. (1964). Note on a heterogeneous shear flow. *Journal of Fluid Mechanics*, *20*(2), 331–336. https://doi.org/10.1017/S0022112064001252

Mishra, S., Unnikrishnan, L., Nayak, S. K., & Mohanty, S. (2019). Advances in Piezoelectric Polymer Composites for Energy Harvesting Applications: A Systematic Review. *Macromolecular Materials and Engineering*, *304*(1), 1800463. https://doi.org/10.1002/mame.201800463

Moum, J. N., Farmer, D. M., Smyth, W. D., Armi, L., & Vagle, S. (2003). *Structure and Generation of Turbulence at Interfaces Strained by Internal Solitary Waves Propagating Shoreward over the Continental Shelf*. https://journals.ametsoc.org/view/journals/phoc/33/10/1520-0485_2003_033_2093_sagota_2.0.co_2.xml

Moum, J. N., & Nash, J. D. (2009a). *Mixing Measurements on an Equatorial Ocean Mooring*. https://doi.org/10.1175/2008JTECHO617.1

Moum, J. N., & Nash, J. D. (2009b). *Mixing Measurements on an Equatorial Ocean Mooring*. https://doi.org/10.1175/2008JTECHO617.1

Muench, J. E., & Kunze, E. (1999). *Internal Wave Interactions with Equatorial Deep Jets. Part I: Momentum-Flux Divergences*. https://journals.ametsoc.org/view/journals/phoc/29/7/1520-0485_1999_029_1453_iwiwed_2.0.co_2.xml

Muench, J. E., & Kunze, E. (2000). *Internal Wave Interactions with Equatorial Deep Jets. Part II: Acceleration of the Jets*. https://journals.ametsoc.org/view/journals/phoc/30/8/1520-0485_2000_030_2099_iwiwed_2.0.co_2.xml

Müller, P., Holloway, G., Henyey, F., & Pomphrey, N. (1986). Nonlinear interactions among internal gravity waves. *Reviews of Geophysics*, *24*(3), 493–536. https://doi.org/10.1029/RG024i003p00493

Munk, W. H. (1966). Abyssal recipes. *Deep Sea Research and Oceanographic Abstracts*, *13*(4), 707–730. https://doi.org/10.1016/0011-7471(66)90602-4

Munk, W., & Wunsch, C. (1998). Abyssal recipes II: Energetics of tidal and wind mixing. *Deep Sea Research Part I: Oceanographic Research Papers*, *45*(12), 1977–2010. https://doi.org/10.1016/S0967-0637(98)00070-3

Nagai, T., Tandon, A., Kunze, E., & Mahadevan, A. (2015). *Spontaneous Generation of Near-Inertial Waves by the Kuroshio Front*. https://doi.org/10.1175/JPO-D-14-0086.1

NASA/JPL. (2019). *GHRSST level 4 MUR 0.25deg global foundation sea surface temperature analysis (v4.2)*. NASA Physical Oceanography Distributed Active Archive Center. https://doi.org/10.5067/GHM25-4FJ42

Nash, J. D., Alford, M. H., Kunze, E., Martini, K., & Kelly, S. (2007). Hotspots of deep ocean mixing on the Oregon continental slope. *Geophysical Research Letters*, *34*(1). https://doi.org/10.1029/2006GL028170

National Science Foundation. (n.d.-a). *History—About NSF*. Retrieved April 26, 2026, from https://www.nsf.gov/about/history

National Science Foundation. (n.d.-b). *NSF Award Database* [Dataset]. Retrieved May 2, 2026, from https://www.nsf.gov/awardsearch/search-results/?PIId=&PIFirstName=&PILastName=&PIOrganization=University+of+California+San+Diego&PIState=CA&PIZip=&PICountry=&ProgOrganization=&ProgEleCode=&BooleanElement=All&ProgRefCode=&BooleanRef=All&Program=&ProgOfficer

Naveira Garabato, A. C., Frajka-Williams, E. E., Spingys, C. P., Legg, S., Polzin, K. L., Forryan, A., Abrahamsen, E. P., Buckingham, C. E., Griffies, S. M., McPhail, S. D., Nicholls, K. W., Thomas, L. N., & Meredith, M. P. (2019). Rapid mixing and exchange of deep-ocean waters in an abyssal boundary current. *Proceedings of the National Academy of Sciences of the United States of America*, *116*(27), 13233–13238. https://doi.org/10.1073/pnas.1904087116

Naveira Garabato, A. C., Yu, X., Callies, J., Barkan, R., Polzin, K. L., Frajka-Williams, E. E., Buckingham, C. E., & Griffies, S. M. (2022). Kinetic Energy Transfers between Mesoscale and Submesoscale Motions in the Open Ocean's Upper Layers. *Journal of Physical Oceanography*, *52*(1), 75–97. https://doi.org/10.1175/JPO-D-21-0099.1

Northcott, D., Boyer, A. L., MacKinnon, J., Alford, M. H., & Lucas, A. J. (2026). *Observations of the Internal Wave to Turbulence Cascade*. https://doi.org/10.1175/JPO-D-25-0114.1

Nyblade, M., & McDonald, J. (2021, September 7). *Recognizing Geology's Colonial History for Better Policy Today*. Eos. http://eos.org/science-updates/recognizing-geologys-colonial-history-for-better-policy-today

Oakey, N. S. (1977). *An Instrument to Measure Oceanic Turbulence and Microstructure* (BI-R-77-3). Bedford Institute of Oceanography. https://waves-vagues.dfo-mpo.gc.ca/Library/53399.pdf

O'Brien, M. H. (1993). Being a scientist means taking sides. *BioScience*, *43*(10), 706–708. https://doi.org/10.2307/1312342

Office of Naval Research. (n.d.). *ONR History*. Retrieved March 1, 2026, from https://www.onr.navy.mil/about-onr/history

Olbers, D. J. (1976). Nonlinear energy transfer and the energy balance of the internal wave field in the deep ocean. *Journal of Fluid Mechanics*, *74*(2), 375–399. https://doi.org/10.1017/S0022112076001857

Olbers, D. J. (1981). *The Propagation of Internal Waves in a Geostrophic Current*. https://journals.ametsoc.org/view/journals/phoc/11/9/1520-0485_1981_011_1224_tpoiwi_2_0_co_2.xml

Oreskes, N. (2021). *Science on a Mission: How Military Funding Shaped What We DO and Don't Know about the Ocean*. University of Chicago Press.

Osborn, T. R. (1974). Vertical Profiling of Velocity Microstructure. *Journal of Physical Oceanography*, *4*(1), 109–115. https://doi.org/10.1175/1520-0485(1974)004%253C0109:VPOVM%253E2.0.CO;2

Osborn, T. R. (1980). *Estimates of the Local Rate of Vertical Diffusion from Dissipation Measurements*. https://journals.ametsoc.org/view/journals/phoc/10/1/1520-0485_1980_010_0083_eotlro_2_0_co_2.xml

Osborn, T. R., & Cox, C. S. (1972). Oceanic fine structure. *Geophysical Fluid Dynamics*, *3*, 321–345. https://doi.org/10.1080/03091927208236085

Patibandla, R., Buckingham, C. E., & Tandon, A. (2025). Near-inertial wave propagation in a curved front. *Journal of Fluid Mechanics*, *1015*, R1. https://doi.org/10.1017/jfm.2025.10358

Pico, T. (2023). Performing Geology: Risk and Conquest in the Origin Stories of a Field Science. *Catalyst: Feminism, Theory, Technoscience*, *9*(2), Article 2. https://doi.org/10.28968/cftt.v9i2.38296

Pinkel, R., Rainville, L., & Klymak, J. (2012). *Semidiurnal Baroclinic Wave Momentum Fluxes at Kaena Ridge, Hawaii*. https://doi.org/10.1175/JPO-D-11-0124.1

Pollard, R. T., & Millard, R. C. (1970). Comparison between observed and simulated wind-generated inertial oscillations. *Deep Sea Research and Oceanographic Abstracts*, *17*(4), 813–821. https://doi.org/10.1016/0011-7471(70)90043-4

Pollmann, F. (2020). Global Characterization of the Ocean's Internal Wave Spectrum. *Journal of Physical Oceanography*, *50*(7), 1871–1891. https://doi.org/10.1175/JPO-D-19-0185.1

Polzin, K. L. (2008). *Mesoscale Eddy–Internal Wave Coupling. Part I: Symmetry, Wave Capture, and Results from the Mid-Ocean Dynamics Experiment*. https://doi.org/10.1175/2008JPO3666.1

Polzin, K. L. (2010). *Mesoscale Eddy–Internal Wave Coupling. Part II: Energetics and Results from PolyMode*. https://doi.org/10.1175/2009JPO4039.1

Polzin, K., & Lvov, Y. V. (2011). Toward Regional Characterizations of the Oceanic Internal Wavefield. *Reviews of Geophysics*, *49*(4). https://doi.org/10.1029/2010RG000329

Polzin, K., Naveira Garabato, A. C., Huussen, T. N., Sloyan, B. M., & Waterman, S. (2014). Finescale parameterizations of turbulent dissipation. *Journal of Geophysical Research: Oceans*, *119*(2), 1383–1419. https://doi.org/10.1002/2013JC008979

Polzin, K., Toole, J. M., Ledwell, J. R., & Schmitt, R. W. (1997). Spatial Variability of Turbulent Mixing in the Abyssal Ocean. *Science*, *276*(5309), 93–96. https://doi.org/10.1126/science.276.5309.93

Polzin, K., Toole, J. M., & Schmitt, R. W. (1995). Finescale Parameterizations of Turbulent Dissipation. *Journal of Physical Oceanography*, *25*(3), 306–328. https://doi.org/10.1175/1520-0485(1995)025%253C0306:FPOTD%253E2.0.CO;2

Prescod-Weinstein, C. (2017, November 22). Black Women Physicists In the Wake. *Medium*. https://medium.com/@chanda/black-women-physicists-in-the-wake-ebf2cdeadb1a

Qu, L., Thomas, L. N., & Hetland, R. D. (2021). *Near-Inertial-Wave Critical Layers over Sloping Bathymetry*. https://doi.org/10.1175/JPO-D-20-0221.1

Rainville, L., & Pinkel, R. (2004). Observations of Energetic High-Wavenumber Internal Waves in the Kuroshio. *Journal of Physical Oceanography*, *34*(7), 1495–1505. https://doi.org/10.1175/1520-0485(2004)034%253C1495:OOEHIW%253E2.0.CO;2

Renault, L., Marchesiello, P., & Contreras, M. (2023). Coaction of Top and Bottom Drags in Gulf Stream Dynamics. *Journal of Geophysical Research: Oceans*, *128*(3), e2022JC018939. https://doi.org/10.1029/2022JC018939

Rio, M.-H., Mulet, S., & Picot, N. (2014). Beyond GOCE for the ocean circulation estimate: Synergetic use of altimetry, gravimetry, and in situ data provides new insight into geostrophic and Ekman currents. *Geophysical Research Letters*, *41*(24), 8918–8925. https://doi.org/10.1002/2014GL061773

Roemmich, D., Alford, M. H., Claustre, H., Johnson, K., King, B., Moum, J., Oke, P., Owens, W. B., Pouliquen, S., Purkey, S., Scanderbeg, M., Suga, T., Wijffels, S., Zilberman, N., Bakker, D., Baringer, M., Belbeoch, M., Bittig, H. C., Boss, E., … Yasuda, I. (2019). On the Future of Argo: A Global, Full-Depth, Multi-Disciplinary Array. *Frontiers in Marine Science*, *6*. https://doi.org/10.3389/fmars.2019.00439

Rowland, H. A. (1883). A Plea for Pure Science. *Science*, *2*(29), 242–250.
Sargent, J. F. (2018, February 21). *Defense Science and Technology Funding*. Library of Congress. https://www.congress.gov/crs-product/R45110

Savage, A. C., Waterhouse, A. F., MacKinnon, J. A., Yu, X., Garabato, A. C. N., Evans, D. G., Frajka-Williams, E., & Thomas, L. N. (2025). *Observations of Upper-Ocean Kinetic Energy Transfers between Near-Inertial Internal Waves and Low-Frequency Dynamics*. https://doi.org/10.1175/JPO-D-23-0230.1

Sawyer, J. S. (1956). The Vertical Circulation at Meteorological Fronts and Its Relation to Frontogenesis. *Proceedings of the Royal Society of London. Series A, Mathematical and Physical Sciences*, *234*(1198), 346–362.

Scarlett, J. P. (2022). The harmful legacy of colonialism in natural hazard risk. *Nature Communications*, *13*(1), 6945. https://doi.org/10.1038/s41467-022-34792-7

Scripps Institution Of Oceanography. (2023). *Progress Reports on Scripps Institution of Oceanography* [Dataset]. https://sio.photoshelter.com/galleries/C0000GBgxyOyNshI/G0000BWCZxCiqcZE/2000

Shakespeare, C. J., & Hogg, A. M. (2019). *On the Momentum Flux of Internal Tides*. https://doi.org/10.1175/JPO-D-18-0165.1

Sherwin, C. W., & Isenson, R. S. (1967). Project Hindsight. *Science*, *156*(3782), 1571–1577.
Shizhe, T., & Yijin, W. (2022). An Artificial Lateral Line Sensor Using Polyvinylidene Fluoride (PVDF) Membrane for Oscillatory Flow Sensing. *IEEE Access*, *10*, 15771–15785. https://doi.org/10.1109/ACCESS.2022.3148165

Siddon, T. E. (1971). A Miniature Turbulence Gauge Utilizing Aerodynamic Lift. *Review of Scientific Instruments*, *42*(5), 653–656. https://doi.org/10.1063/1.1685193

Spiess, F., & Kuperman, W. (2003). The Marine Physical Laboratory at Scripps. *Oceanography*, *16*(3), 45–54.

TallBear, K. (2014). Standing With and Speaking as Faith: A Feminist-Indigenous Approach to Inquiry. *Journal of Research Practice*, *10*(2), Article 2.

Tedesco, P. F., Baker, L. E., Garabato, A. C. N., Mazloff, M. R., Gille, S. T., Caulfield, C. P., & Mashayek, A. (2023). Spatiotemporal Characteristics of the Near-Surface Turbulent Cascade at the Submesoscale in the Drake Passage. *Journal of Physical Oceanography*, *54*(1), 187–215. https://doi.org/10.1175/JPO-D-23-0108.1

Thomas, L. N., Kelly, S. M., Klenz, T., Young, W. R., & Rainville, L. (2024). *Why Near-Inertial Waves Are Less Affected by Vorticity in the Northeast Pacific Than in the North Atlantic | Oceanography*. https://tos.org/oceanography/article/why-near-inertial-waves-are-less-affected-by-vorticity-in-the-northeast-pacific-than-in-the-north-atlantic

Thomas, L. N., Moum, J. N., Qu, L., Hilditch, J. P., & Kunze, E. (2024). Blocked Drainpipes and Smoking Chimneys: Discovery of New Near-Inertial Wave Phenomena in Anticyclones | Oceanography. *Oceanography*, *37*(4), 22–33. https://doi.org/10.5670/oceanog.2024.304

Torrence, C., & Compo, G. P. (1998). *A Practical Guide to Wavelet Analysis*. https://journals.ametsoc.org/view/journals/bams/79/1/1520-0477_1998_079_0061_apgtwa_2_0_co_2.xml

Uchida, T., Jamet, Q., Dewar, W. K., Le Sommer, J., Penduff, T., & Balwada, D. (2022). Diagnosing the Thickness-Weighted Averaged Eddy-Mean Flow Interaction From an Eddying North Atlantic Ensemble: The Eliassen-Palm Flux. *Journal of Advances in Modeling Earth Systems*, *14*(5), e2021MS002866. https://doi.org/10.1029/2021MS002866

UCSD Libraries. (n.d.). *Tell Us How UC It: History of Student Activism Timeline* [Dataset]. Retrieved April 28, 2026, from https://library.ucsd.edu/dc/collection/bb72746900

van Eck, C. W., Messling, L., & Hayhoe, K. (2024). Challenging the neutrality myth in climate science and activism. *Npj Climate Action*, *3*(1), 1–3. https://doi.org/10.1038/s44168-024-00171-9

Viet, N. V., Wu, N., & Wang, Q. (2017). A review on energy harvesting from ocean waves by piezoelectric technology. *Journal of Modeling in Mechanics and Materials*, *1*(2). https://doi.org/10.1515/jmmm-2016-0161

Voet, G., Alford, M. H., Cusack, J. M., Pratt, L. J., Girton, J. B., Carter, G. S., Klymak, J. M., Tan, S., & Thurnherr, A. M. (2023). *Energy and Momentum of a Density-Driven Overflow in the Samoan Passage*. https://doi.org/10.1175/JPO-D-22-0220.1

Voet, G., Alford, M., Polzin, K., Naveira Garabato, A., Kawamato, S., Dufel, H., Hogue, B., Wynne-Cattanach, B., Couto, N., Le Boyer, A., Spyngis, C., Messias, M.-J., & Mercier, H. (2024). *Boundary layer turbulence and abyssal recipes (BLT): Moored observations* (Version 3, p. 32871436467 bytes) [Dataset]. Dryad. https://doi.org/10.5061/DRYAD.V15DV424F

Voet, G., Alford, M., Polzin, K., Naveira Garabato, A., Wynne-Cattanach, B., Couto, N., Le Boyer, A., Spyngis, C., Messiar, M.-J., & Mercier, H. (2024). *Boundary Layer Turbulence and Abyssal Recipes (BLT): Multibeam Bathymetry Dataset* [Dataset]. SEANOE. https://doi.org/10.17882/99872

Wang, R., Qiao, Q., Yang, S., Kong, X., Liu, G., Chen, X., Yang, H., Song, D., Jia, L., Cui, J., He, C., Yang, Y., Zhang, G., Xue, C., & Zhang, W. (2022). High-Sensitivity MEMS Shear Probe for Autonomous Profiling Observation of Marine Turbulence. *Remote Sensing*, *14*(19), Article 19. https://doi.org/10.3390/rs14195004

Waterhouse, A. (2017). Internal Tide Convergence and Mixing in a Submarine Canyon in: Journal of Physical Oceanography Volume 47 Issue 2 (2017). *Journal of Physical Oceanography*, *47*(2), 303–322. https://doi.org/10.1175/JPO-D-16-0073.1

Waterhouse, A. F., MacKinnon, J. A., Nash, J. D., Alford, M. H., Kunze, E., Simmons, H. L., Polzin, K. L., Laurent, L. C. S., Sun, O. M., Pinkel, R., Talley, L. D., Whalen, C. B., Huussen, T. N., Carter, G. S., Fer, I., Waterman, S., Garabato, A. C. N., Sanford, T. B., & Lee, C. M. (2014). *Global Patterns of Diapycnal Mixing from Measurements of the Turbulent Dissipation Rate*. https://doi.org/10.1175/JPO-D-13-0104.1

Waterman, S., Polzin, K. L., Garabato, A. C. N., Sheen, K. L., & Forryan, A. (2014). Suppression of Internal Wave Breaking in the Antarctic Circumpolar Current near Topography. *Journal of Physical Oceanography*, *44*(5), 1466–1492. https://doi.org/10.1175/JPO-D-12-0154.1

Whalen, C. B., Talley, L. D., & MacKinnon, J. A. (2012). Spatial and temporal variability of global ocean mixing inferred from Argo profiles. *Geophysical Research Letters*, *39*(18). https://doi.org/10.1029/2012GL053196

Whitt, D. B., & Thomas, L. N. (2013). *Near-Inertial Waves in Strongly Baroclinic Currents*. https://doi.org/10.1175/JPO-D-12-0132.1

Whitt, D. B., Thomas, L. N., Klymak, J. M., Lee, C. M., & D'Asaro, E. A. (2018). *Interaction of Superinertial Waves with Submesoscale Cyclonic Filaments in the North Wall of the Gulf Stream*. https://doi.org/10.1175/JPO-D-17-0079.1

Winkel, D. P. (1998). *Influences of mean shear in Florida current on turbulent production by internal waves*. http://hdl.handle.net/1773/11024

Wunsch, C. (1969). Progressive internal waves on slopes. *Journal of Fluid Mechanics*, *35*(1), 131–144. https://doi.org/10.1017/S0022112069001005

Wunsch, C., & Ferrari, R. (2004). Vertical Mixing, Energy, and the General Circulation of the Oceans. *Annual Review of Fluid Mechanics*, *36*(Volume 36, 2004), 281–314. https://doi.org/10.1146/annurev.fluid.36.050802.122121

Wynne-Cattanach, B. L., Couto, N., Drake, H. F., Ferrari, R., Le Boyer, A., Mercier, H., Messias, M.-J., Ruan, X., Spingys, C. P., van Haren, H., Voet, G., Polzin, K., Naveira Garabato, A. C., & Alford, M. H. (2024). Observations of diapycnal upwelling within a sloping submarine canyon. *Nature*, *630*(8018), 884–890. https://doi.org/10.1038/s41586-024-07411-2

Wynne-Cattanach, B. L., Couto, N., Drake, H., Ferrari, R., Le Boyer, A., Mercier, H., Messias, M.-J., Ruan, X., Spingys, C., Van Haren, H., Voet, G., Polzin, K., Naveira Garabato, A., & Alford, M. (2024). *boundary layer turbulence and abyssal recipes: Moorings, microstructure and dye survey datasets* [Dataset]. [object Object]. https://doi.org/10.17882/98178

Young, W., & Jelloul, M. (1997). Propagation of near-inertial oscillations through a geostrophic flow. *Journal of Marine Research*, *55*(4). https://elischolar.library.yale.edu/journal_of_marine_research/2242